NSEL Report Series
Report No. NSEL-052
October 2021

Full-scale Laboratory Testing of Embedded Miter Gate Anchorages to Inform Fatigue Life Estimates

Brian A. Eick
Nathaniel M. Levine
Matthew D. Smith
and
Billie F. Spencer, Jr.

Department of Civil and Environmental Engineering
University of Illinois at Urbana-Champaign

UILU-ENG-2021-2103

ISSN: 1940-9826

The Newmark Structural Engineering Laboratory (NSEL) of the Department of Civil and Environmental Engineering at the University of Illinois at Urbana-Champaign has a long history of excellence in research and education that has contributed greatly to the state-of-the-art in civil engineering. Completed in 1967 and extended in 1971, the structural testing area of the laboratory has a versatile strong floor/wall and a three-story clear height that can be used to carry out a wide range of tests of building materials, models, and structural systems. The laboratory is named for Dr. Nathan M. Newmark, an internationally known educator and engineer, who was the Head of the Department of Civil Engineering at the University of Illinois [1956-73] and the Chair of the Digital Computing Laboratory [1947-57]. He developed simple, yet powerful and widely used, methods for analyzing complex structures and assemblages subjected to a variety of static, dynamic, blast, and earthquake loadings. Dr. Newmark received numerous honors and awards for his achievements, including the prestigious National Medal of Science awarded in 1968 by President Lyndon B. Johnson. He was also one of the founding members of the National Academy of Engineering.

Contact:
Prof. B.F. Spencer, Jr.
Nathan M. and Anne M. Newmark Endowed Chair in Civil Engineering
2213 NCEL, MC-250
205 North Mathews Ave.
Urbana, IL 61801
Telephone (217) 333-8630
E-mail: bfs@illinois.edu

This technical report is based on joint work performed in the Newmark Structural Engineering Laboratory by students and faculty in the Department of Civil and Environmental Engineering at the University of Illinois and researchers at the US Army Corps of Engineers Engineer Research and Development Center.

Financial support for this research was provided in part by the US Army Corps of Engineers through a subaward from the University of California, San Diego.

The cover photographs are used with permission. The Trans-Alaska Pipeline photograph was provided by Terra Galleria Photography (http://www.terragalleria.com/).

ABSTRACT

On the inland navigation system, miter gates are common structures that are supported by steel frames known as anchorages embedded in the concrete lock chamber wall. These anchorages primarily resist the overturning moment caused by the self-weight of the gate as it swings open and closed. Typically, miter gates will swing open and closed many times per day such that the loading experienced by the miter gate anchorages is cyclic in nature, and so, fatigue life of anchorages must be considered. A significant concern regarding miter gate anchorages is that many of the anchorages have been in service since the construction of the lock, oftentimes more than eighty years ago. The typical analysis approach to miter gate anchorages is to ignore the embedding concrete and treat the anchorage as a freestanding truss. This approach to analysis leads to unreasonably high estimation of stresses in the anchorage components, further exacerbating fatigue concerns. To aid in understanding the stress distribution of embedded anchorage components, the researchers of this study perform a full-scale test of a miter gate anchorage. The test is performed in three phases. In phase one, the anchorage is supported in a manner to represent the assumptions of the traditional analysis of anchorages, where the embedding concrete is ignored. In phase two and three, the anchorage is embedded in concrete. In phase two, the extent of the embedding concrete is intended to represent the configuration typical to so-called miter or primary anchorages. In phase three, a portion of the embedding block is cut away to simulate the reduced concrete coverage typical of the so-called recess or secondary anchorages. In all phases, the anchorage is pulled to simulate the reaction of the hanging miter gate that the in-service anchorage would support and the strain response throughout the anchorage is recorded with strain gages. In this initial study, the results are used to inform the code-based fatigue analysis typically performed by design engineers. A metric is defined, termed the strain-modulus, that is used to estimate the magnitude of axial stress in anchorage components given an applied load. It is seen that in all but one case, the strain modulus decreases in the anchorage when embedded in concrete in phase 2 and 3 as opposed to the unembedded anchorage in phase 1. The strain modulus is then leveraged to update the code-based fatigue analysis and it is shown that, for most of the unembedded portions of the anchorage, the stress in well below the endurance limit of steel such that fatigue limit states likely need not be considered. As such, design engineers may wish to reevaluate plans to excavate and replace these anchorages in kind. Ultimately, this testing is intended to develop a representative dataset that can be used to quantify the interaction between steel and concrete in miter gate anchorages. The dataset will be used to calibrate modeling procedures, inform future design, as well as adjust existing lifecycle estimates.

CONTENTS

INTRODUCTION

1.1 Background

Miter gates are common structures used at the 193 lock sites owned and operated by the US Army Corps of Engineers (USACE) along the inland waterways that comprise the Inland Navigation System [1] [2]. Miter gates act as the damming surface of the lock chamber allowing water level inside the chamber to differ from the water level outside the chamber. This report focuses on a critical component of miter gates known as the embedded anchorage which acts as the primary supporting member securing the miter gate to the lock chamber wall. The embedded anchorages are typically steel components that are mostly embedded in the concrete lock chamber wall and connected to the upper hinge (or, gudgeon) portion of the miter gate by steel bars. A typical schematic of a miter gate and embedded anchorage is shown in the elevation view in Figure 1-1. Each leaf (or, door) of a miter gate is generally supported by two anchorages: one in line with the gate when it is fully closed (often referred to as the miter or primary anchorage), and one in line with the gate when it is fully opened (often referred to as the recess or secondary anchorage). The different orientations of the two anchorages are highlighted in the plan view shown in Figure 1-2. Note the proximity of the secondary anchorage to the edge of the concrete wall, which will come into consideration during this study.

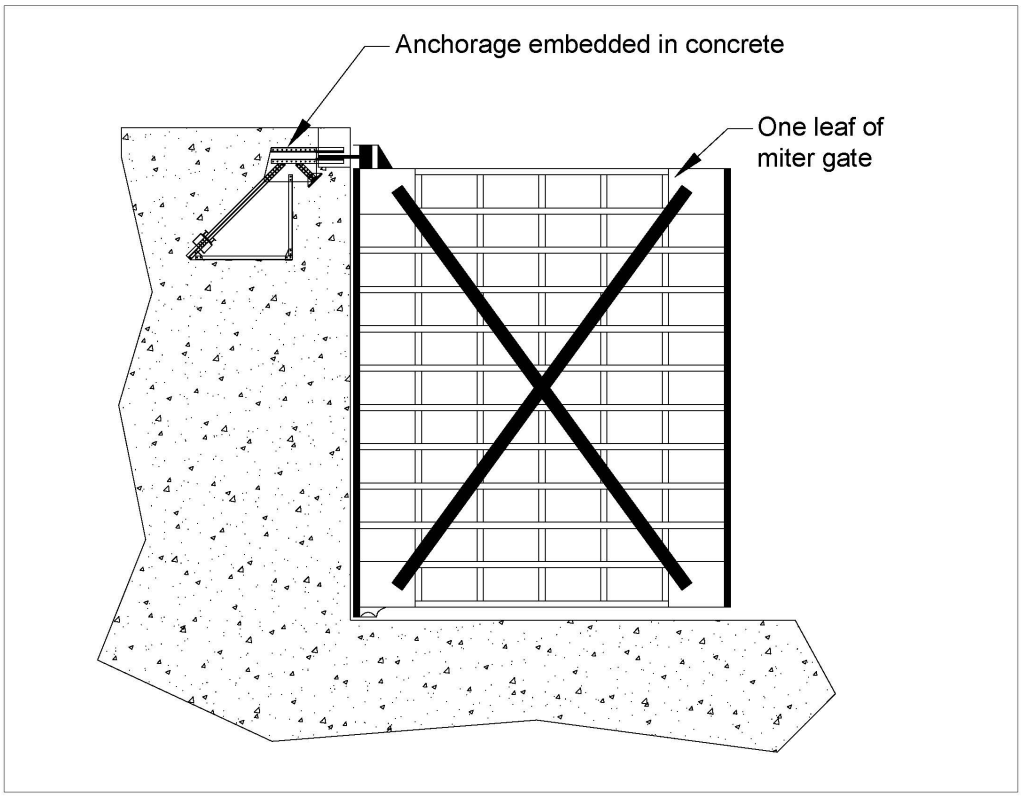

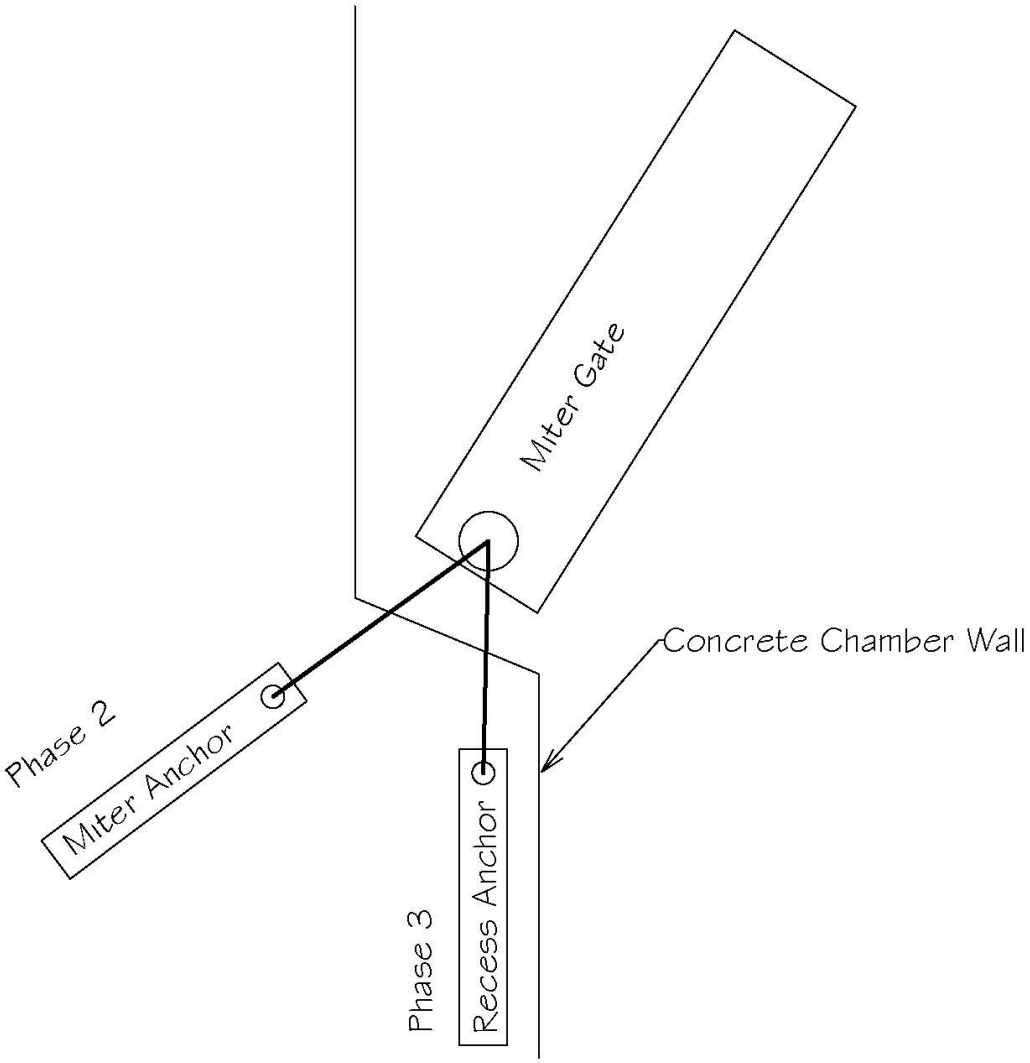

The primary loading scenario on miter gate anchorages is from the overturning moment of a hanging miter gate. An elevation view of an anchorage is shown in Figure 1-3, with arrows showing the assumed distribution of forces caused by the overturning moment of the hanging gate. Referring to Figure 1-2, as the gate swings open or closed, the reaction of the overturning moment is shared between the primary and secondary anchorages, with the percentage of the reaction on each anchorage dependent on the position of the gate. That is, when the gate is fully open, the secondary anchorage is intended to resist 100% of the overturning moment. Similarly, when the gate is fully closed, the primary anchorage is intended to resist 100% of the overturning moment. In intermediate positions, the anchorages share the load proportionally based on the angle of the gate. Thus, every time the gate opens and closes, the anchorages experience a load cycle. Gate swings may occur dozens of time per day, and so anchorages may experience thousands of load cycles per year, and so material fatigue is a primary concern in anchorage analysis and design.

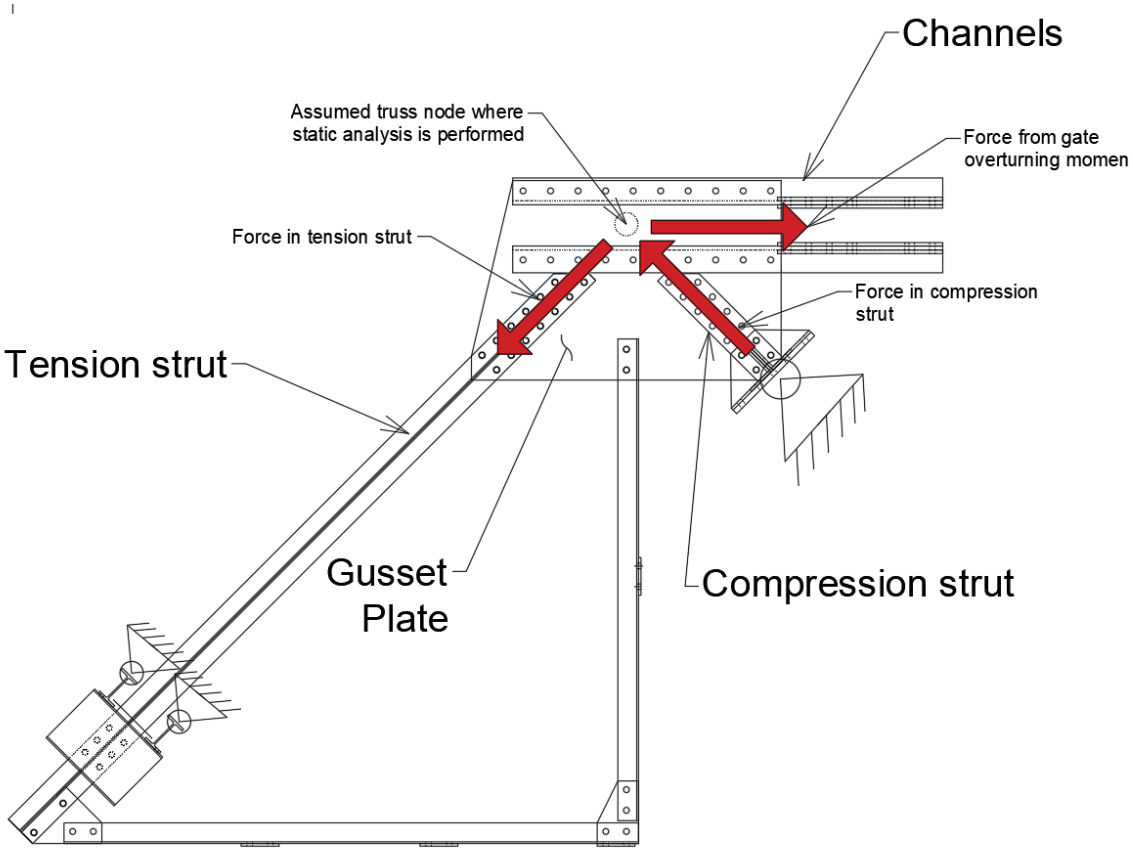

1.1.1 Fatigue analysis of miter gate anchorages

The cyclic nature of loading on miter gate anchorages is such that fatigue is a primary concern. Compounding fatigue concerns is the fact that most of the miter gates are intended to be supported by existing embedded anchorage systems that are "original", meaning they can be as much as 80 years old. Traditionally, analysis of the anchorage is performed by ignoring any contributions to structural performance that the embedding concrete might have due to bonding and/or bearing between the steel and concrete. This conservative analysis approach suggests unreasonably high stresses in the steel components of the anchorage, effectively leading to the assumption that the load cycles experienced by the anchorage have unreasonably high stress amplitudes. The age of the anchorages, along with the conservative analysis approach, has led to concern that fatigue failure of many of these anchorages is imminent. Failure of an anchorage will ultimately lead to loss of a miter gate, and the potential for significant economic impact through closure of the lock chamber and delays on the inland navigation system [3] [4] [5].

For miter gate anchorages, fatigue analysis is frequently performed according to the AASHTO Manual for Bridge Evaluation [6]. Equation 7.2.5.1-1 is the AASHTO manual is used to find an estimate of fatigue life for miter gate components. The AASHTO approach is based on traditional power law approaches developed in part by the work of Wohler [7] and Basquin [8], and the linear accumulated damage law developed by Miner [9]. The AASHTO equation is adjusted here in eq. (1-1) to provide an expression for remaining life as follows:

$$Y_{remaining} = \frac{R_R A}{N_{mean}\left[(\Delta f)_{eff}\right]^3} - Y_{service} \quad (1\text{-}1)$$

where $Y_{remaining}$ is the finite fatigue life of the detail in years, $Y_{service}$ is the years in which the anchorage has been in service, R_R and A are AASHTO specific constants, N_{mean} is the average number of cycles experienced by the anchorage based on lock records, and $(\Delta f)_{eff}$ is the effective stress range per cycle. For riveted connections typical of historical miter gate anchorages, the most appropriate detail for fatigue analysis is 2.3 from table 6.6.1.2.3-1 in the AASHTO (2017). This detail leads to a fatigue category "D" with R_R and A equal to 1.6 and 2.2 x 10^9 ksi^3, respectively. For the fatigue analysis of miter gate anchorages, $(\Delta f)_{eff}$ is found by assuming that the miter gate anchorage typically cycles between no stress and the stress caused by resisting the full overturning moment caused by the quasi-static opening and closing of the gate. The magnitude of the full stress is found by simple static truss analysis highlighted in Figure 1-3. The truss analysis shows that the tension strut is the critical member as it has the highest tensile stress under the typical load. The AASHTO-based fatigue analysis is performed for a selection of miter gate anchorages along the Upper Mississippi river for which gate weight, dimensions, and annual cycle data were available with results in Table 1-1. Note, the anchorages along the upper Mississippi River are all of a similar construction, and the representative tension strut cross-section is taken as 6.86 in^2.

Table 1-1 Remaining life of anchorages along the Upper Mississippi River, based on AASHTO equation 7.2.5.1-1

Lock designation	$Y_{service}$ (as of 2021)	Max Force in tension strut (kips)	$(\Delta f)_{eff}$ (ksi)	N_{mean}	$Y_{remaining}$ (years)
11	84	122	17.8	6646	10.1
12	82	122	17.8	6195	19.0
13	82	122	17.8	5882	24.4
14	82	125	18.2	8381	-12.6
15	87	117	17.1	8397	-2.5
16	82	125	18.2	8244	-11.4
17	82	122	17.8	7170	5.3
18	82	125	18.2	8004	-9.3
20	85	125	18.2	6325	6.9
21	83	120	17.5	6527	17.8
22	83	120	17.5	6275	21.8

The data shown in Table 1-1 shows results for remaining life of the anchorages if the originally designed miter gates were to remain on the anchorage. In the coming years, USACE district engineers within the USACE Mississippi Valley Division (MVD) will be tasked to hang new miter gates at their lock and dam sites. These new miter gates are significantly heavier than the old gates, which will increase $(\Delta f)_{eff}$ and exacerbate fatigue concerns. Moreover, the embedding concrete of these anchorages precludes inspection of the vast majority of the system, and so, the current condition of the embedded portion of these anchorages is completely unknown. Accordingly, there is reluctance throughout MVD to hang the heavier new gates on these anchorage systems of unknown quality. However, it is suspected that the embedding concrete contributes significantly to the structural behavior of the system. However, without definitive evidence supporting this

notion, there is reluctance to accept this notion given the economic and life-safety implications of a failed miter gate anchorage.

1.1.2 Previous work performed

Through conversations with miter gate design engineers and operations personnel, it is known that when embedded anchorage systems have been excavated, it is typical to see bonding between the steel and concrete. Moreover, even in the absence of bonding, it is deemed very likely that the steel of the anchorage will bear against the concrete in such a manner as to alleviate a great deal of stress throughout the anchorage. Thus, characterizing and quantifying the interaction of steel and concrete in miter gate anchorages is of primary importance in order to get a more accurate representation of the stress amplitudes the anchorages experience under a load cycle. There is a dearth of work in the literature regarding the material interaction between steel and concrete of structural components of a size similar to miter gate anchorages. There has been significant investigation on the material interaction of steel rebar [10] [11] [12] [13] [14], as well as concrete-filled steel tubes [15] [16] [17], but none of these component are directly analogous to the truss-like behavior of miter gate anchorage. Several studies have leveraged finite element analysis (FEA) to describe complicated steel/concrete interaction [18] [19] [20]. Similarly, many studies have leveraged FEA to aid in the analysis of complicated miter gate behavior [21] [22] [23]. Levine, et al. [24], coupled the two approaches in the analysis of miter gate anchorages. They simulated the interaction between steel and concrete as springs acting normal to each surface to the embedded portions of the anchorage. Spring stiffness was selected based on foundation modulus found in the literature [25]. They show that the inclusion of concrete/steel interaction in a numerical model of an embedded anchorage significantly reduces the stress throughout the anchorage. The reduction in stress occurs even with the conservative assumption is made to only consider bearing interaction and ignore bonding between the steel and concrete by having springs only in the direction normal to the surface. Changes in stress were particularly stark in the tension strut of the anchorage. Here, stress went from being the highest in the structure to being effectively negligible. Figure 1-4 shows the change in stress in the numerical model of the embedded anchorage when bearing between steel and concrete is simulated via springs. In almost all locations of the model, the stress decreases.

While the numerical models provide analytical evidence of the lack of stress in the embedded portions of the anchorage, there is a strong desire from stakeholders to perform physical testing of full-scale anchorages to verify the modeling results. In 2018, two new anchorages were instrumented at Lock and Dam 20 on the Mississippi river to determine the change in strain response in the embedded portion by comparing strain gage data before and after the embedding concrete was poured [26]. An image of the instrumented anchorage at Lock and Dam 20 is shown in Figure 1-5. Some thirty strain gages were installed on the anchorage, and a novel loading method was developed to place the anchorage under tension using a Nord-lock supernut and a threaded rod. Due to concerns of strength of the anchor rods prior to pouring of concrete, the project engineers allowed a maximum tensile load of 20 kips to be placed on the specimen. Even with a larger allowable load, on-site constraints would've made it difficult to apply a force larger than 20 kips. The results indeed appear to corroborate those obtained via the numerical model. However, there was a persistent issue with noise in the recorded data and the applied load was of such a small magnitude that it was unclear if the strain gages were responding at all to the load. Moreover, the anchorage at Lock and Dam 20 is not representative of the typical anchorages seen along the Upper

Mississippi River. Thus, the uncertainty in the collected data, and the uniqueness of the new anchorage at Lock and Dam 20 led to a desire for additional physical testing.

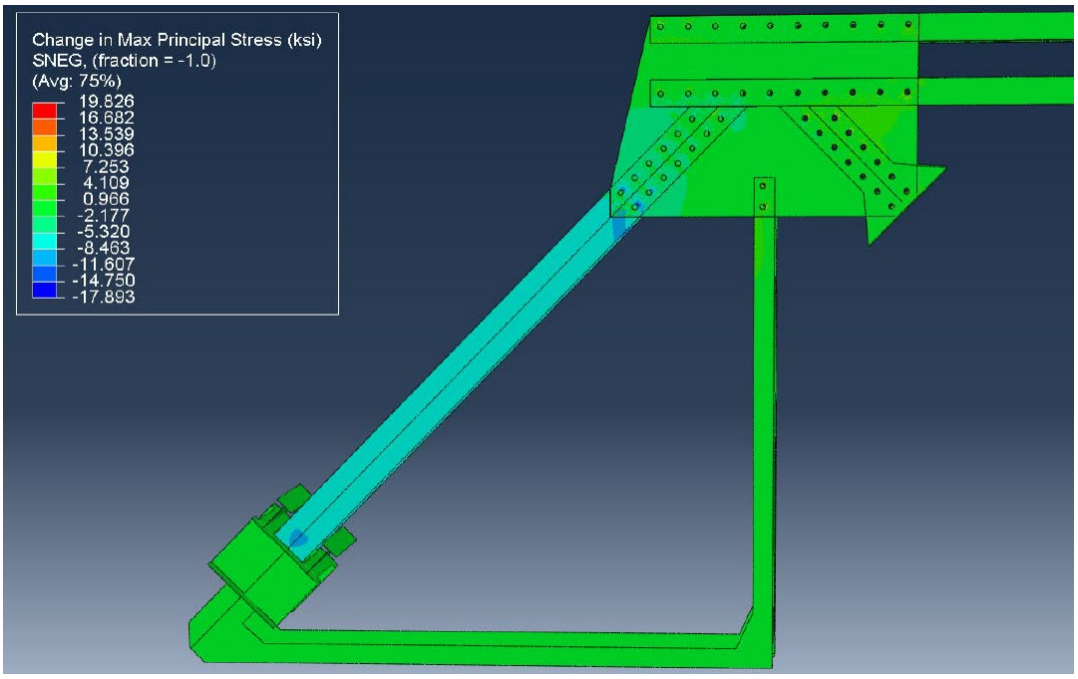

Figure 1-4 Change in stress in the numerical model of an embedded anchorage when bearing interaction between steel and concrete is simulated. Negative values indicate that stress decreases when concrete is simulated.

Figure 1-5 Instrumented anchorage at Lock 20, prior to installation

1.2 Objective

The goal of the test is to definitively show whether or not the embedded portions of the anchorage experience significant load under representative loading conditions. By performing this test in a laboratory environment, loads of significant magnitude can be applied and issues with noise in the data can be more easily addressed. To inform historical fatigue analysis, a direct comparison will be made to the magnitude of stress when the concrete is ignored and the magnitude of stress when the concrete is considered. This study aims to provide definitive evidence that neglecting the interaction between steel and concrete is excessively conservative. In doing so, a representative data set will be generated to validate and calibrate models to more accurately quantify the stress distribution of the embedded portion of the anchorages when under load. Ultimately, this testing will lead to more accurate fatigue life predictions for the embedded anchorages of miter gates.

The approach is to load a full-scale miter gate embedded anchorage to obtain representative strain data for the structure when concrete is and is not present. The testing will take place in 3 phases. In phase 1, the anchorage is supported in a manner to mimic the traditional analysis method of ignoring the structural contribution of embedding concrete. In phase 2, the test specimen is embedded in concrete to simulate the actual environment of a typical primary/miter anchorage with an effectively infinite domain of embedding concrete. In phase 3, a significant portion of the embedding concrete is removed in order to simulate a secondary/recess anchorage. Recall the difference between the miter and recess anchorages, as highlighted in Figure 1-2. In all phases, the anchorage specimen in instrumented with an array of strain gages that are used to characterize the stress distribution throughout the specimen.

With the results from the testing, a metric is found (herein termed the “strain modulus”) that allows for the estimation of strain, and thus stress, distribution of the components of similarly constructed anchorages. This metric is used in conjunction with the typically used AASHTO fatigue analysis to provide an updated estimate of the remaining fatigue life of the anchorages already analyzed in Table 1-1. Results of the test largely support the findings of the previous numerical studies that stress in the embedded portions of the anchorage quickly dissipates into the embedding concrete. In the tension strut of the anchorage, the stress of the test specimen is effectively negligible, and stress amplitudes would be below commonly accepted values of the endurance limit of steel such that fatigue analysis could likely be ignored. It should be noted that it is infeasible to accurately simulate concrete degradation similar to what may be seen on lock and dam sites in service for eighty or more years. Therefore, engineers and asset managers interested in the results of this study should carefully consider on-site conditions prior to directly applying the results of this study to decisions regarding anchorage repair or replacement.

This report is an extension of the publication by Eick, et al, [27], where the size limitations of the journal article format prevented sharing of all but the most informative data. Here, data and the associated metrics are presented for all sensors used in the study for the benefit of interested stakeholders and to aid in future work to leverage the obtained results for future analysis and design.

METHODOLOGY

This test of the anchorage is to be performed in three phases. Phase 1 of the test mimics the assumed conditions of the traditional analysis method, whereby the anchorage is a free-standing truss supported only at the foot of the compression and tension struts. Phase 2 of the test will see the test specimen embedded in concrete to mimic primary anchorage typical of the upper Mississippi River locks and dams. For phase 3, a large portion of the embedding concrete is removed such that the embedding condition simulates those for a secondary anchorage. In this section, the design of the anchorage and concrete are discussed, as are specifics of the testing method and protocols. Instrumentation and data acquisition parameters are also discussed, and the metrics used for analysis are described in detail.

2.1 Anchorage and Concrete design

The anchorage fabricated for the test was designed to be as close as possible to an exact replica of the original anchorages installed at Lock 16 on the Upper Mississippi River. The original drawings for the anchorage at Lock 16 are shown in Figure 2-1. Unavailable historical steel shapes were replaced with similar modern shapes. This was primarily an issue for the tension and compression struts, listed on the original drawings as 12" I @ 28#. These were replaced with the similar S12X30.8. Additionally, rivets were replaced with bolts. To simulate the bearing surface present in the rivets of the original anchorage, tension-control bolts were utilized. The grade of steel used in the original construction is unknown. For the test specimen, all steel is ASTM A36. The yield strength of this grade of steel is expected to be similar to the steel in the original construction; however, the testing performed will load the structure in the linear range, and so yield strength should have minimal effect on results. The fabricated test specimen standing in the lab prior to placement of the supports is shown in Figure 2-2.

For the portion of the test where the specimen will be embedded, the concrete mix was designed per recommendations of USACE MVR engineers. A 3000 psi design strength mix was selected to achieve a strength of 4500-5000 psi at testing. The block in which the test specimen is embedded strikes a balance of being large enough to simulate the effectively infinitely large concrete domain of the in-situ lock chamber wall, while still being feasibly constructed and supported in the laboratory. Ultimately, the embedding concrete block has dimensions of 10'W X 14' L X 12' H. Concrete reinforcement is intended to represent the reinforcing cage typically used in the field and consists of No. 6 bars surrounding the specimen, spaced at 12 inches. No. 4 bars are used in the horizontal direction to tie the No. 6 bars together. An elevation view showing the rebar layout for the concrete block is given in Figure 2-3 while a plan view is provided in Figure 2-4. Note, at the time of the concrete pour, cylinders were taken to determine a concrete strength curve via ASTM C39 [28] Results for concrete strength are presented in the following chapter.

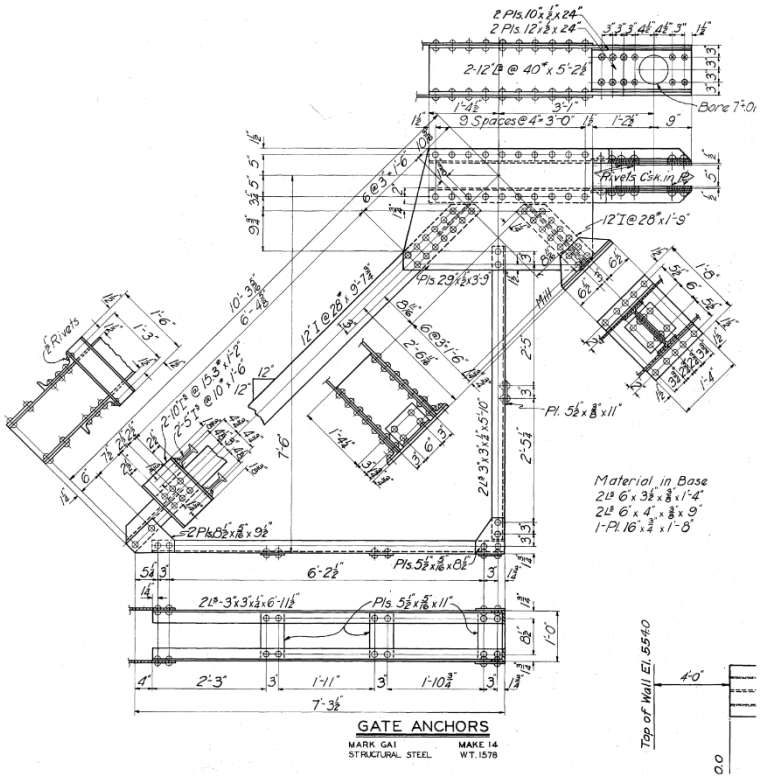

Figure 2-1 Original Lock 16 anchorage drawings

Figure 2-2 Fabricated test specimen standing in the lab.

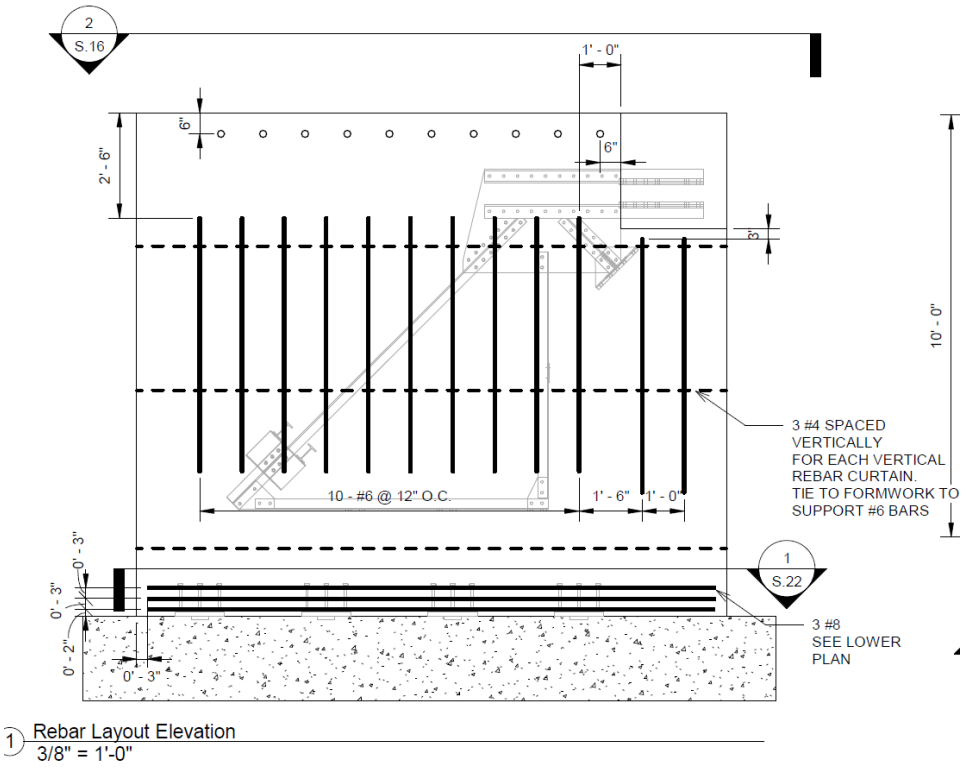

Figure 2-3. Elevation view showing rebar layout

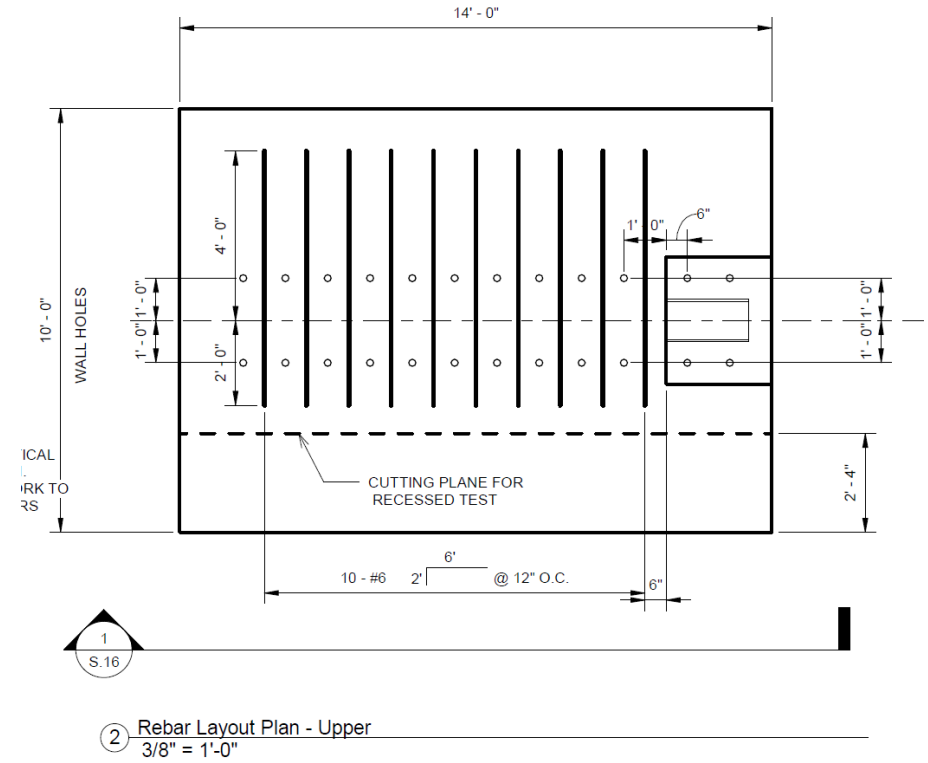

Figure 2-4 Plan view of rebar layout

2.2 Test setup and procedure

2.2.1 Phase 1

For phase 1, the anchorage is setup to resemble to traditional method of analysis whereby the embedding concrete is ignored. To accomplish this, steel fixtures were fabricated to provide the supports necessary. For the compression strut, rolled steel members were welded together to provide a bearing surface against which the compression strut can push. For the tension strut, steel rectangular tubes were welded around the tension strut like a yoke, which was then bolted to a welded steel assembly that was ultimately bolted to the floor. These supports are shown in a schematic in Figure 2-5, with a close up of the tension yoke shown in Figure 2-6.

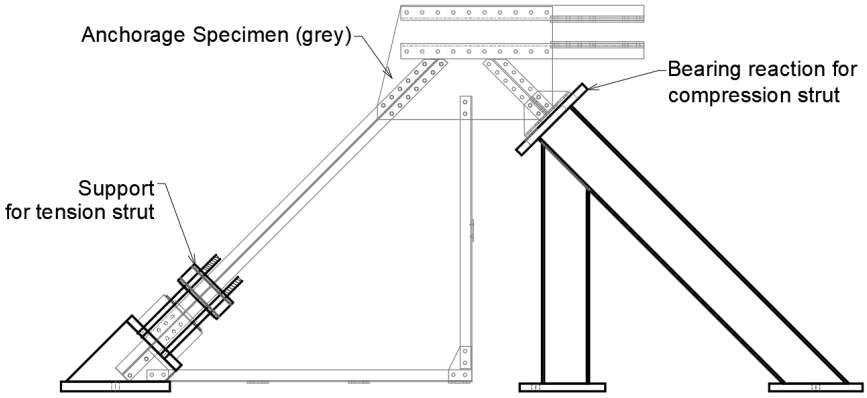

Figure 2-5 Schematic showing anchorage supports for phase 1 to mimic traditional analysis assumptions

Figure 2-6 Close up of tension reaction yoke

To apply sufficient load to the anchorage, two actuators with 220 kip capacity were attached to a spreader beam and programed to pull on the anchorage in a synchronized manner. A 3D schematic of the entire phase 1 test setup is shown in Figure 2-7, while an overhead view of the test setup in the lab is shown in Figure 2-8. Concerns about strength and stability of the test specimen in phase 1 led to a need to apply a relatively limited load of 140 kips. This load was applied several times and readings were taken from the instrumentation to characterize the strain response of the specimen.

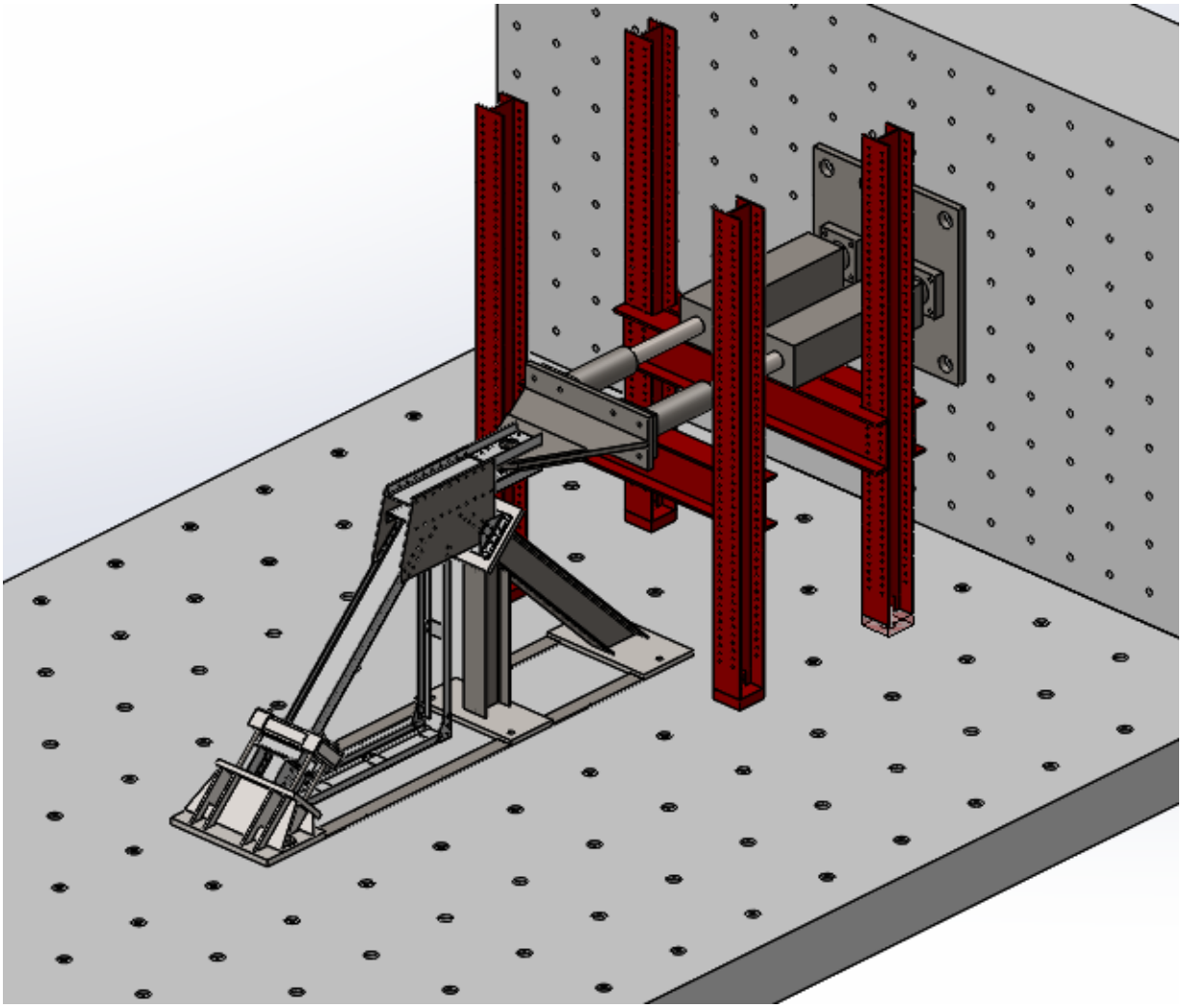

Figure 2-7 3D schematic of phase 1 bare-steel test

Figure 2-8. Overhead view of phase 1 setup in the lab

2.2.2 Phase 2

In phase 2, the anchorage is fully embedded in concrete to simulate the actual in-situ conditions of a miter gate embedded anchorages. In this phase, the supports fabricated for phase 1 are removed and the anchorage was lifted several feet off the ground prior to pouring of concrete to minimize any boundary effects at the bottom of the anchorage, as seen in Figure 2-9. To prevent sliding or overturning of the concrete block when placed under load, 8 Dywidag-type threaded rods were passed through the block, post-tensioned, and anchored to the laboratory reaction floor. Additional shear keys were added at floor connections to resist sliding of the block. The supports for the block are shown in Figure 2-10. For this phase of testing, the anchorage is supported exclusively by the embedding concrete, as in the field. Loading of the anchorage is exactly the same as in phase 1. For phase 2, there is less concern of strength and stability, and so the full force of the actuators can be applied. For this interim report, the following chapter only discusses results for the phase 1 test and the phase 2 test up to 140 kips, as a one-to-one comparison is easily made. For the phase 2 test, data was also obtained for loading up to 390 kips (targeting 400 kips, but limited by hydraulic pump pressure capacity and small misalignments in the actuator). This data has not been processed in detail, and so is not discussed in detail in the following chapter. However, the data is presented in the Appendix to further inform the behavior of the embedded anchorages when subjected to loads more representative of a miter gate. The follow up full report of the testing will discuss results from the full 400 kip load placed on the anchorage. For phase 2, a 3D schematic of the test setup is shown in Figure 2-11, while a picture of the setup in the lab is shown in Figure 2-12.

Figure 2-9. Test specimen raised off floor prior to pouring of concrete

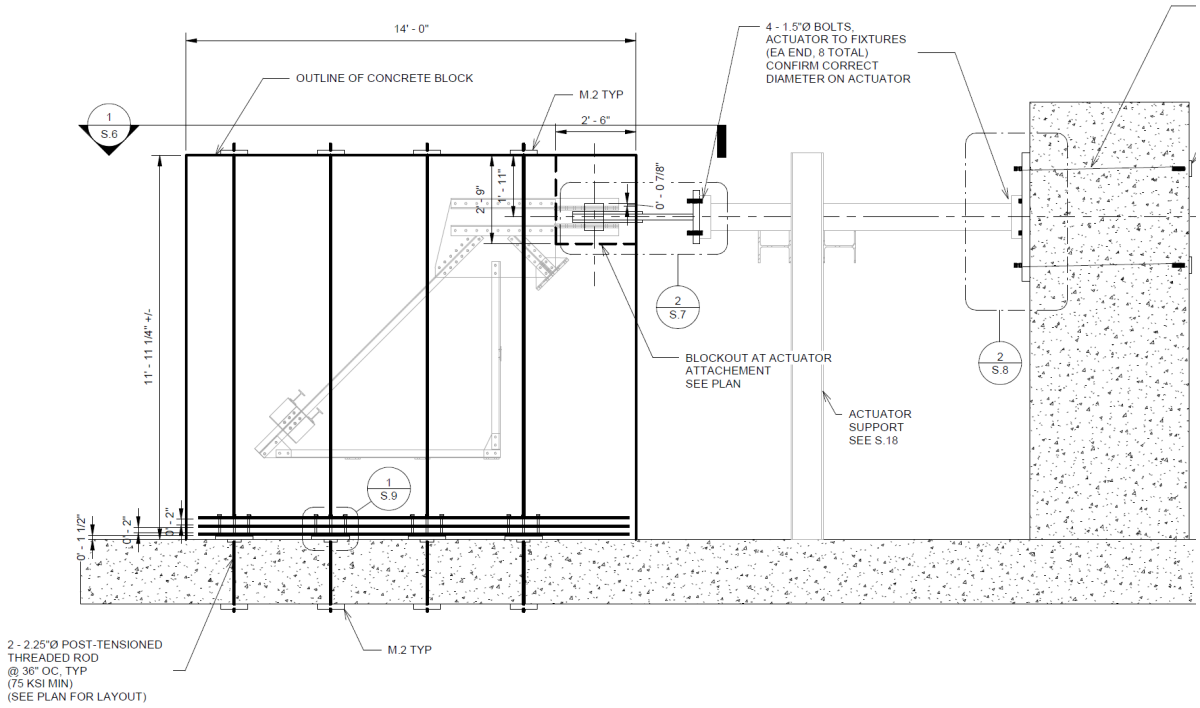

Figure 2-10. Schematic of installed concrete block.

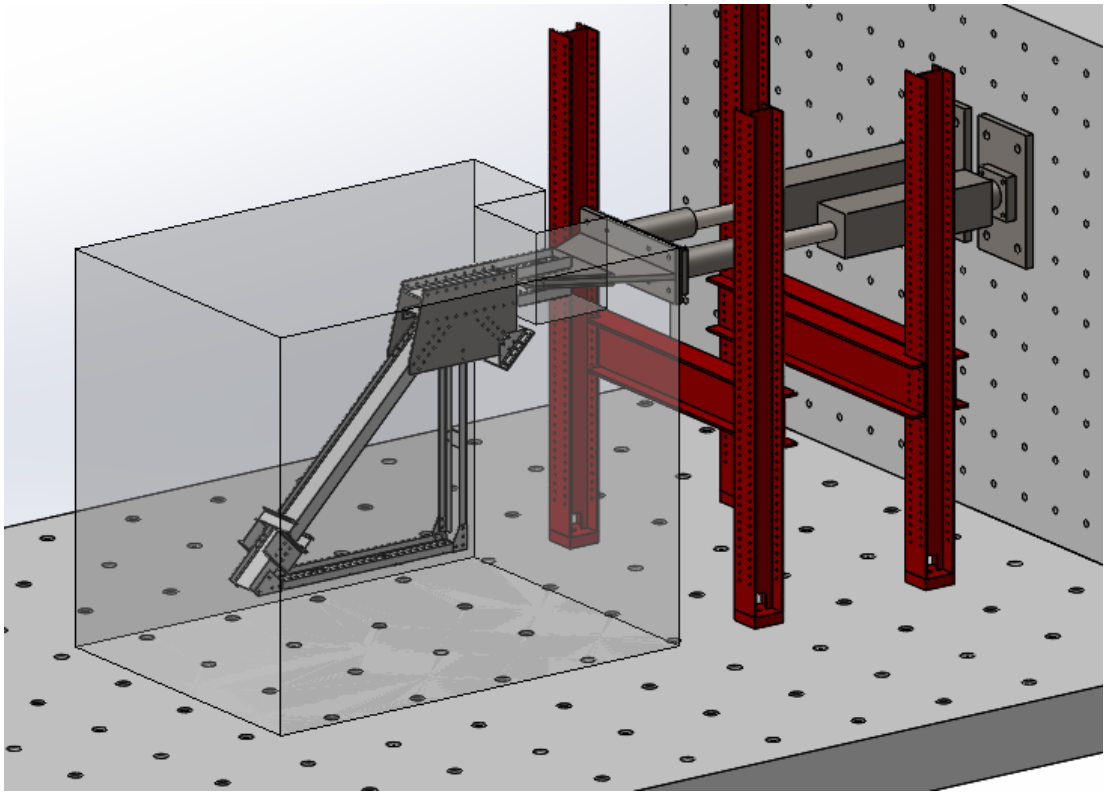

Figure 2-11 3D schematic of phase 2: embedded test

Figure 2-12 Setup of phase 2 test in the lab

2.2.3 Phase 3

The testing procedure for phase 3 is identical to phase 2, with the exception that a portion of the concrete block is cut to simulate the minimal concrete cover on one face of a secondary anchorage. For the phase 3 test, the south-side of the concrete block was cut away such that the south-facing surfaces of the anchorage specimen has a depth of concrete cover identical to the recess anchor at Lock and Dam 16 on the Mississippi River (and typical of most recess anchorages along the Upper Mississippi River). The cutting procedure was performed with a wire saw and a 28” deep section of the block was cut off, as shown by the cutting-line in Figure 2-4. The wire saw in place and cutting the block is shown in Figure 2-13. The final cut portion of the block is shown in Figure 2-14.

Figure 2-13. Wire saw cutting the block of concrete in preparation for Phase 3

Figure 2-14 Finished cut of the concrete block

2.3 Instrumentation data acquisition and data processing procedures

The instrumentation installed on the anchorage is Micro-measurements 350 Ohm, quarter-bridge strain gages [29]. These were installed following manufacturer recommended procedures with the Micro-measurements M-Bond 200 adhesive [30]. Locations of strain gages are provided in the results section and are thus not provided here for brevity. Gage locations were selected to aid in quantifying the distance over which significant stress remains in the embedded steel (in other words, how "quickly" the embedding concrete dissipates the stress). Thus, strain gages were spaced along steel members with relatively high concentration of gages near the edge of the embedding concrete. To protect the strain gages during the concrete pouring procedure, the strain gages were covered in an epoxy and then further coated in a water proofing material. Strain gages were wired in the three-wire configuration. For data acquisition, a National Instruments (NI) SCXI-1001 chassis [31] is used with the SCXI-1520 [32] module combined with the SCXI-1314 universal strain terminal block accessory [33]. Force and displacement signals were recorded from the actuators using the SCXI-1102 module.

Data acquisition was performed using the NI SignalExpress software [34]. For the phase I/ bare steel test, data was sampled at 10 Hz, which proved to be sufficient. For the phase 2/concrete test, electrical noise was a persistent issue. To prevent aliasing of the noise a combination of an analogue anti-aliasing filter and higher sample rate of 40 Hz was used. The anti-aliasing filter was a low-pass filter provided in the SCXI-1520 module and was setup with a cutoff frequency of 10Hz. Note, the low-pass filter was utilized in the phase I test, but the cutoff frequency was left at the default value of 10 kHz with no perceived need to adjust it.

At the start of testing, the strain gages were zeroed so that the measurements would be indicative of the change in strain due to the applied loads to the anchorage, while eliminating any residual strain due to self-weight, ambient thermal effects, or strain caused by gage installation. Nevertheless, during testing, data acquisition equipment tends to heat up due to flowing electrical current, and so some small drift in gage readings due to heating is typical. To address this issue the first reading of each strain gage when no load is applied during a test is taken as the zero reading of that gage for that particular test. That zero reading is then subtracted from all other readings of the gage. This ensures that the strain readings all start near zero strain for a particular test.

After collection of the data, an additional digital low-pass filter is used to further reduce the noise content of the signal. The filter utilized in a 10-pole butterworth filter with a cutoff frequency of $1/100^{th}$ of the Nyquist frequency. This filter is implemented in the Scipy package of the Python computing language [35]. For additional information regarding Nyquist frequencies, filtering, and signal processing, the reader is directed to an appropriate textbook, such as that by de Silva [36].

2.4 Metrics for investigation

Plots comparing all results from the tests with and without concrete are provided in the appendix. In this section, a simple metric is presented, herein referred to as the 'strain modulus', for easy comparison of the strain response at gage locations on the anchorage between the two sets of tests. The strain modulus is taken as the slope of the ordinary least squares (OLS) linear regression fit of the data. For the data herein, the slope of the OLS fit provides an indication of the average increase in micro-strain given a unit increase in applied force to the anchorage (in kips). The slope of the OLS fit of the data is found as:

$$\hat{\beta} = \frac{\sum(x_i - \bar{x})(y_i - \bar{y})}{\sum(x_i - \bar{x})^2} = \frac{cov(x,y)}{var(x)} \tag{2-1}$$

Where the 'bar' indicates the mean of the variable, 'cov' indicates the covariance, and 'var' indicates the variance. Details on calculating the sample variance and covariance from a set of data can be found in introductory statistics books, such as that by Hogg, McKean, and Craig [37]. Additional details for the OLS approach to linear regression can be found in the text by Sheather [38], for example. In the case of the tests performed herein, the values of interest are the strain response due to the applied load, and so y is the measured strain and x is the applied load. Thus, for the tests herein, the slope of the OLS fit is defined as

$$\hat{\beta} = \frac{cov(\mu\epsilon, P)}{var(P)} \tag{2-2}$$

Where $\mu\epsilon$ is the measured strain and P is the corresponding applied load. For the data herein, this metric has units of micro-strain per kip-applied force. The strain modulus thus provides an indication of the average increase in strain at a strain gage due to a unit increase in applied force to the anchorage. The higher the number, the more stress and strain is experienced in the local region of the anchorage under a given load (where the local region is the region immediately surrounding the strain gage).

The overwhelming majority of strain gages in this test responded in a nearly perfect linear fashion, making a linear regression fit appropriate. One such typical linear gage response is shown in Figure 2-15, which shows the response of strain gage S-10 for all the bare-steel tests (in black) with the average OLS fit superimposed in pink. Several gages show a response that is something other than perfectly linear such as that seen Figure 2-16 for gage S-02. These gages are typically near a support or point of load application where complicated contact phenomenon occur. For most of these gages, an OLS fit is still sufficient to characterize the average response, such as the OLS fit shown in pink superimposed on the data in Figure 2-16. For two gages, S-01 and N-19, the response is particularly poorly described by an OLS fit, as seen in Figure 2-17 (data in black, OLS fit in pink).

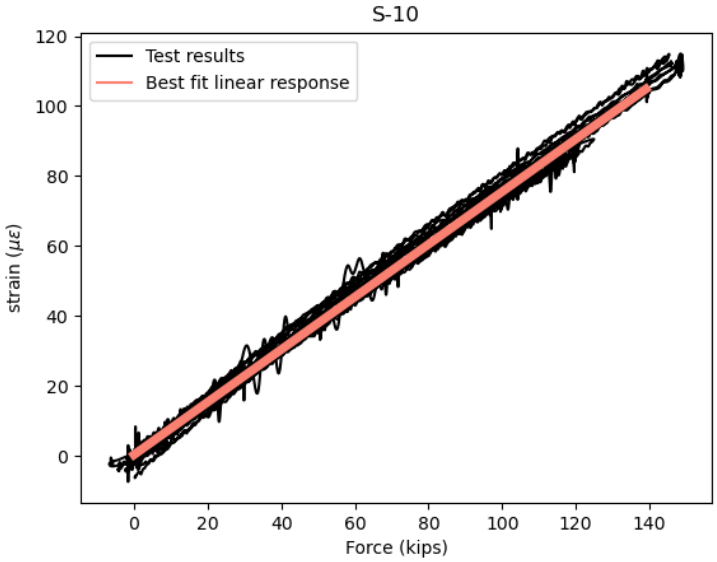

Figure 2-15 Strain response for gage-S-10 for all tests without concrete (black) with the OLS fit (pink) superimposed.

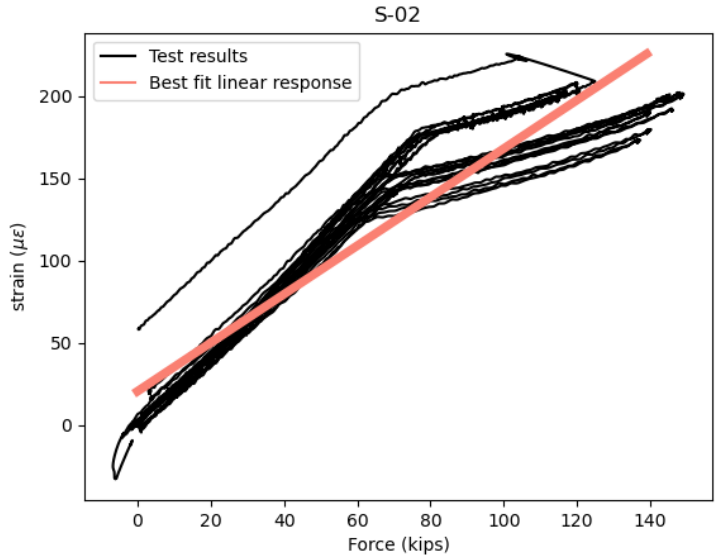

Figure 2-16 Not perfectly linear response of gage S-02 for all tests without concrete (black) , still well represented by OLS fit (pink)

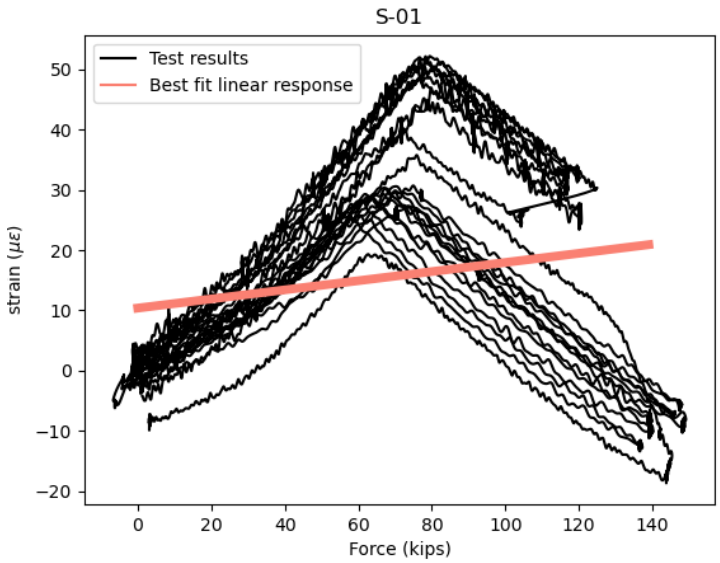

Figure 2-17 Response of strain gage S-01 for all tests without concrete (black), poorly represented by OLS fit

A metric to gage the quality of the OLS fit is the R-squared value. For a univariate regression, the R-squared value is equal to the square of the correlation coefficient between the dependent and independent variables (strain and force, respectively, in this case). It takes values between 0 and 1. The closer the R-squared value is to 1, the stronger the linear relationship between the variables (and the better the OLS fit). The R-squared value is defined as

$$R^2 = \left(\frac{cov(x,y)}{\sqrt{var(x)}\sqrt{var(y)}} \right)^2 \tag{2-3}$$

Where, all variables are as described above. As an example, the average R-squared for the data shown for gage S-10 in figure Figure 2-15 is 0.99 suggesting a nearly perfect linear relationship. For the data shown in Figure 2-16 for gage S-02, the R-squared is 0.94, suggesting that a linear relationship is still appropriate. For the data shown in Figure 2-17 for gage S-01, the average R-squared is 0.35, suggesting a linear relationship is not appropriate.

An additional metric that is of interest is the percentage change in strain modulus between the test performed with concrete and the test performed without concrete. It is of particular interest to gage the percentage change due to the addition of the embedding concrete, and so the change is measured against the results from the test without concrete. Formally, the percentage change is calculated as:

$$\Delta\%_{strainModulus} = 100 \times \frac{\hat{\beta}_{concrete} - \hat{\beta}_{no\ concrete}}{\hat{\beta}_{no\ concrete}} \tag{2-4}$$

RESULTS

In this section, the relevant results are shown. First, the strength results for the concrete cylinders are shown, and then metrics used for investigation of the strain data are shown. For each gage, a comparison bar plot is given showing the average strain modulus from the different phases of the test as calculated using eq. (2-2). The change in modulus is also shown in an additional bar plot, as calculated using eq. (2-4). Results are further tabulated along with the R-squared value (as calculated using eq. (2-3)) for each OLS fit to inform the goodness-of-fit. For an easy one-to-one comparison, the results between the different phases up to 140 kips are initially shown. Then the results between phase 2 and 3 up to the maximum load of the actuators are shown. The results are presented per region of the anchorage, defined as the channels, the north gusset, the south gusset, the tension strut, and the compression strut. For each region, an image is provided to highlight the location of each gage. Note, in all cases, the gages are oriented to measure strain along the long dimension of the shown rectangle. Values listed as "N/A" are for sensors damaged during the pouring of concrete for phase 2 and 3.

3.1 Concrete strength

Concrete cylinders were pulled from the concrete pour and tested to determine a strength development curve. The results from the various cylinder tests are presented in Table 3-1 and the strength development curve is shown in Figure 3-1. Testing for phase 2 reported herein was performed at concrete age of 69 days. Phase 3 testing was performed several weeks thereafter.

Table 3-1 Concrete cylinder strength

		Cylinder				
Age (days)	Quantity	1	2	3	4	Average
3	Load (lbs)	28410	27860	27860	33330	
	f'c (psi)	2261	2217	2217	2652	**2337**
7	Load (lbs)	51100	40480	43380	N/A	
	f'c (psi)	4066	3221	3452	N/A	**3580**
14	Load (lbs)	55840	52350	57870	58030	
	f'c (psi)	4444	4166	4605	4618	**4458**
28	Load (lbs)	72170	62670	73490	75160	
	f'c (psi)	5743	4987	5848	5981	**5640**
45	Load (lbs)	73150	74670	70860	70440	
	f'c (psi)	5821	5942	5639	5605	**5752**
69	Load (lbs)	79700	75010	N/A	N/A	
	f'c (psi)	6342	5969	N/A	N/A	**6156**

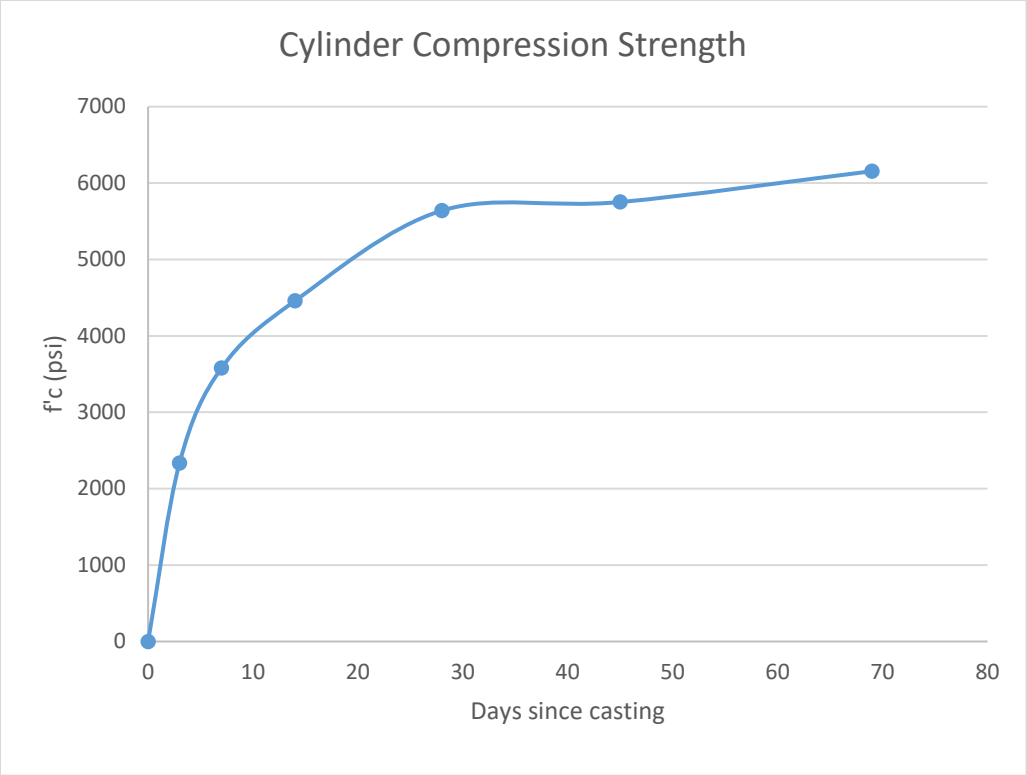

Figure 3-1 Concrete cylinder strength development curve

3.2 Channel sections

The approximate location of strain gages on the exposed portions of the channels are shown in red in the plan view of Figure 3-2 and elevation view of Figure 3-3. Gage N-22, N-23, S-22, and S-23 are attached to the flanges of the channels; T-11 is placed on the top doubler plate of the top channel and B-11 is placed on the bottom doubler plate of the bottom channel. Strain modulus results are shown in the bar plot in Figure 3-4, and the percentage change in strain moduli are shown in Figure 3-5. All results are tabulated in Table 3-2. Note, for the channels, plotted results are not shown for N-22 as this gage was damaged during the concrete pouring procedure.

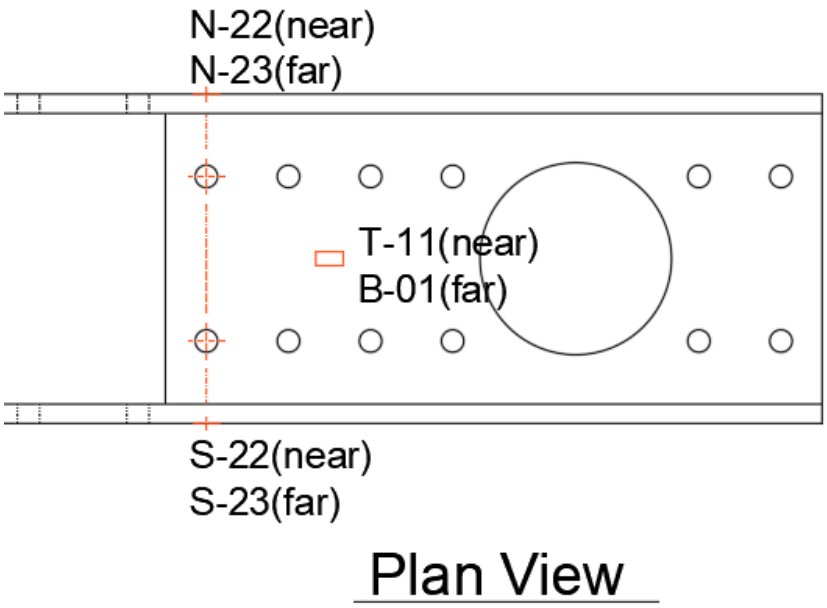

Figure 3-2 Plan view of exposed portion of channels showing installed strain gage labels

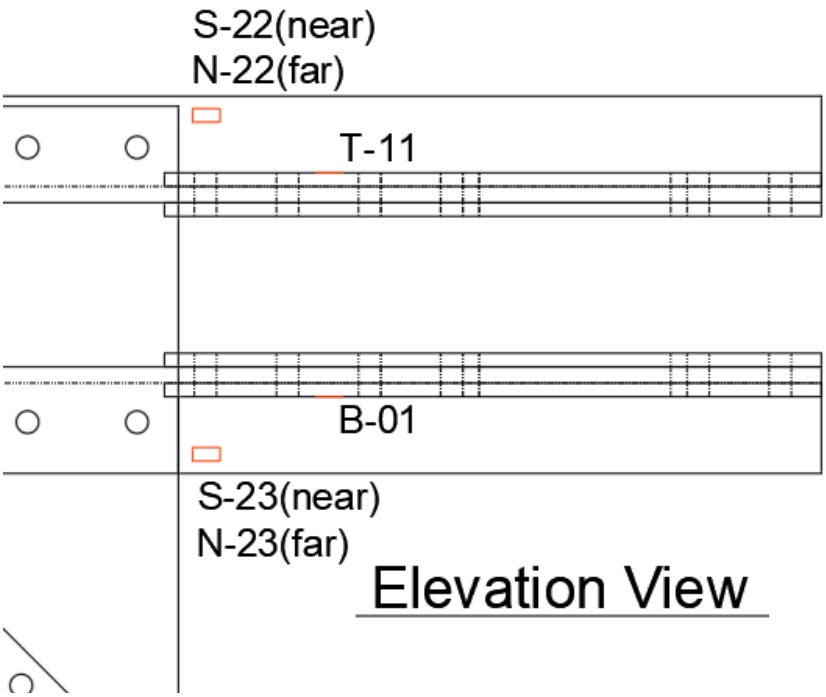

Figure 3-3 Elevation view of exposed portion of channels showing strain gage labels

3.2.1 Results for 140 kip test

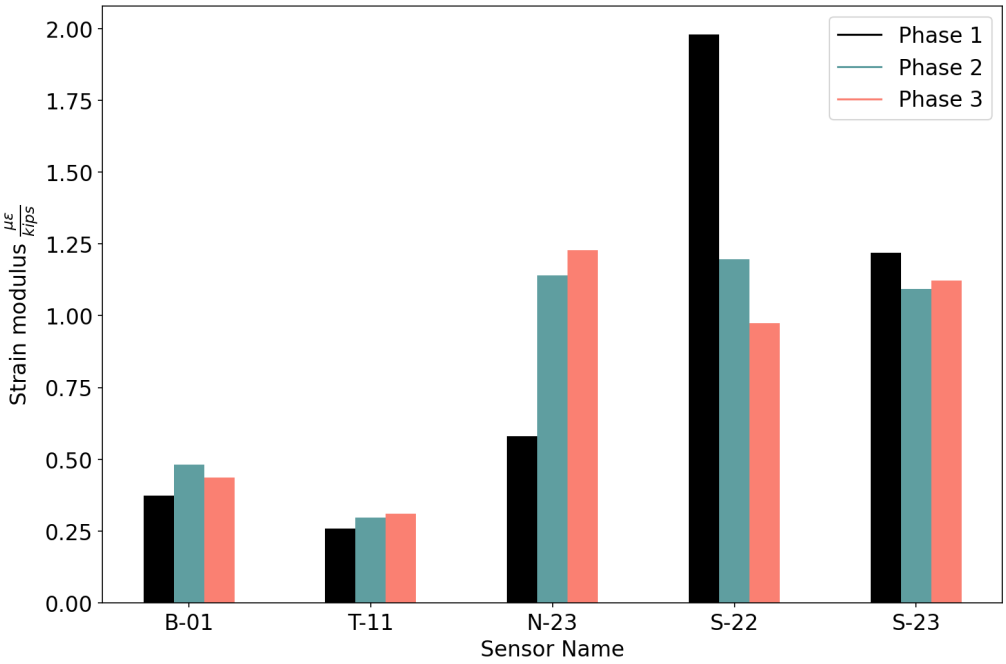

Figure 3-4. Average strain-modulus for tests with and without concrete for channel strain gages

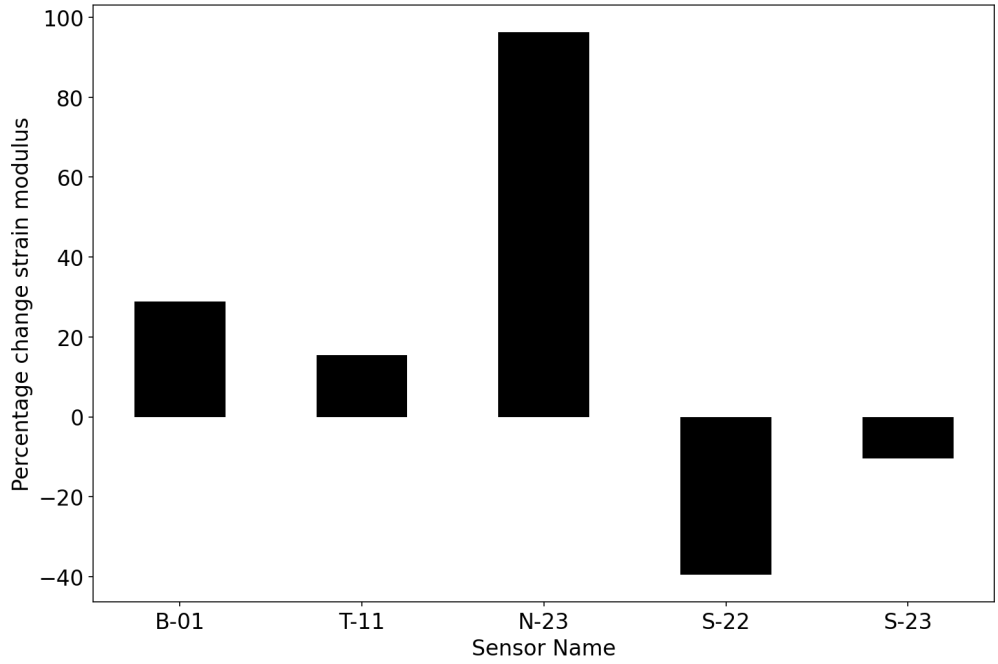

Figure 3-5 Percentage change in strain modulus for channel strain gages for phase 2

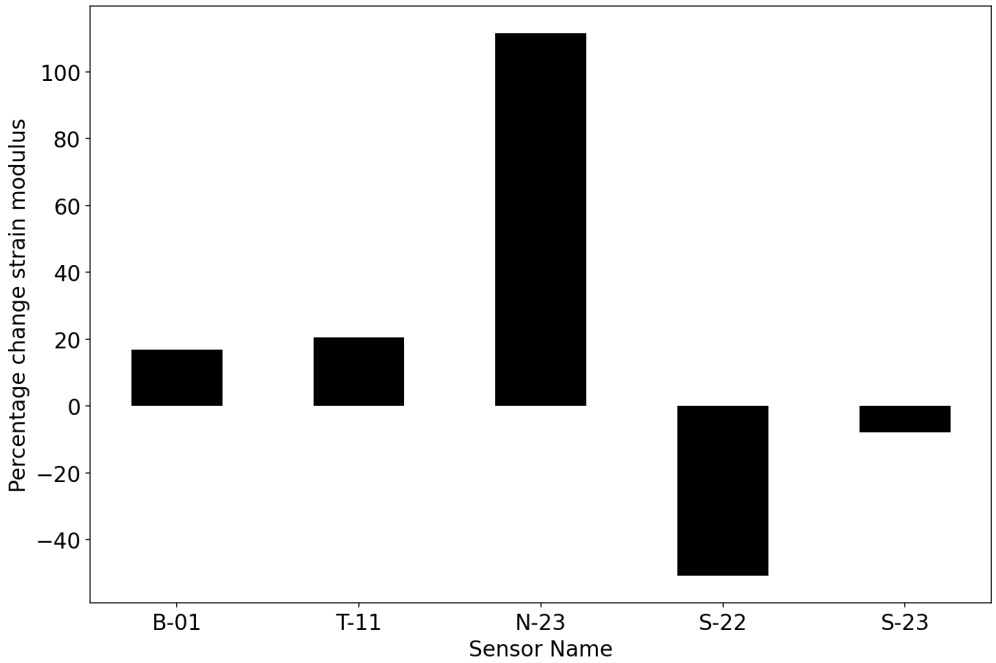

Figure 3-6 Percentage change in strain modulus for channel gages for phase 3

Table 3-2 Strain moduli and R-squared values for gages on the channels

Sensor	Phase 1		Phase 2		Phase 3	
	$(\frac{\mu\epsilon}{kip})$	R^2	$(\frac{\mu\epsilon}{kip})$	R^2	$(\frac{\mu\epsilon}{kip})$	R^2
B-01	0.3738	0.98	0.4817	0.92	0.437	0.92
T-11	0.2581	0.99	0.2979	0.98	0.3112	0.99
N-22	2.2746	1	N/A	N/A	N/A	N/A
N-23	0.581	0.93	1.1402	0.97	1.2291	0.99
S-22	1.9789	0.99	1.1969	0.92	0.9731	0.94
S-23	1.2197	1	1.0932	0.99	1.1232	1

3.2.2 Results for max load tests.

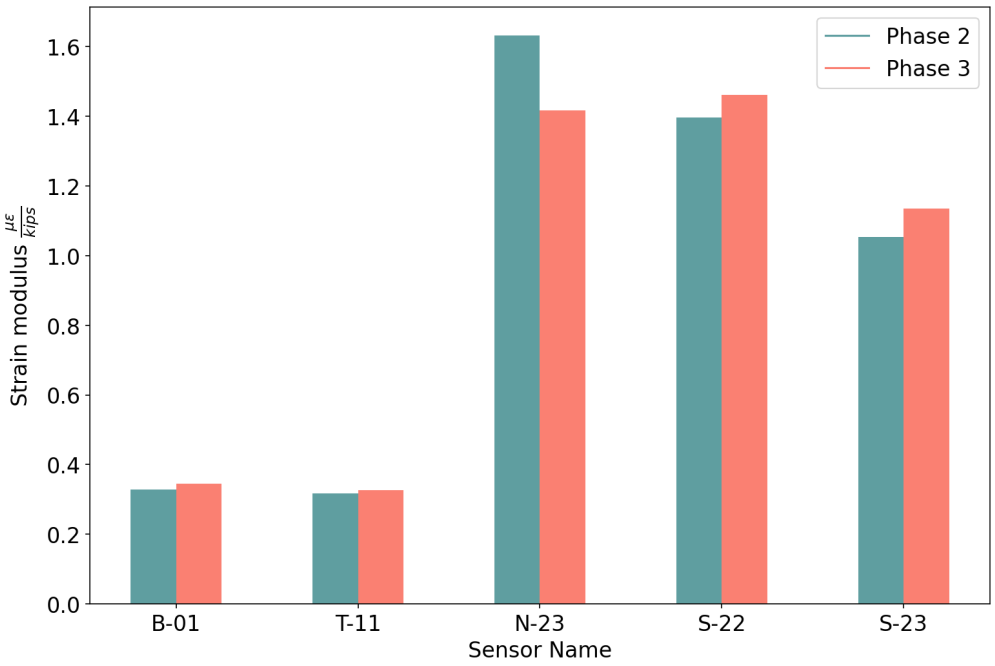

Figure 3-7 Strain modulus for channel gages, max load test

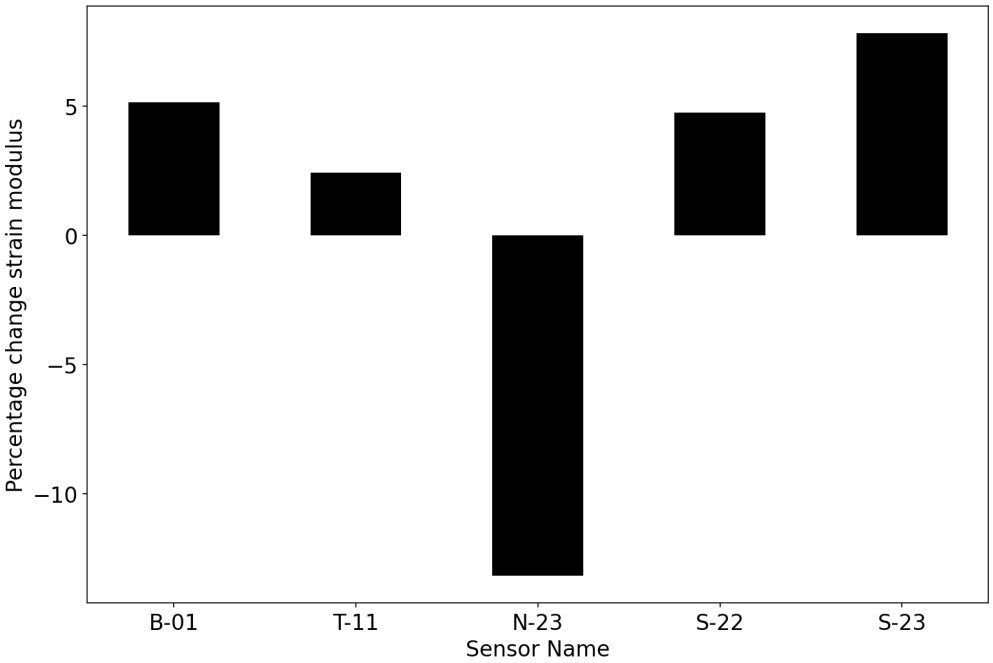

Figure 3-8 Percentage change between phase 3 and phase 2 of max load test

Table 3-3. Strain modulus and r-squared values for channel gages, max load

Sensor	Phase 2		Phase 3	
	$(\frac{\mu\epsilon}{kip})$	R^2	$(\frac{\mu\epsilon}{kip})$	R^2
B-01	0.3284	0.98	0.3263	0.98
T-11	0.318	0.98	0.3375	0.99
N-23	1.6318	0.99	1.5028	1
S-22	1.3956	1	1.378	0.99
S-23	1.053	1	1.183	1

3.3 North Gusset

Approximate gage locations on the north gusset plate are shown in Figure 3-9. All gages on the north gusset plate are attached on the outside face of the plate. The average strain moduli are shown in the bar plot in Figure 3-10. The percentage change in strain moduli are shown in Figure 3-11. All results are tabulated in Table 3-4Note, for the north gusset, plotted results are not shown for N-08, N-15 and N-16. These gages were damaged during the concrete pouring procedure.

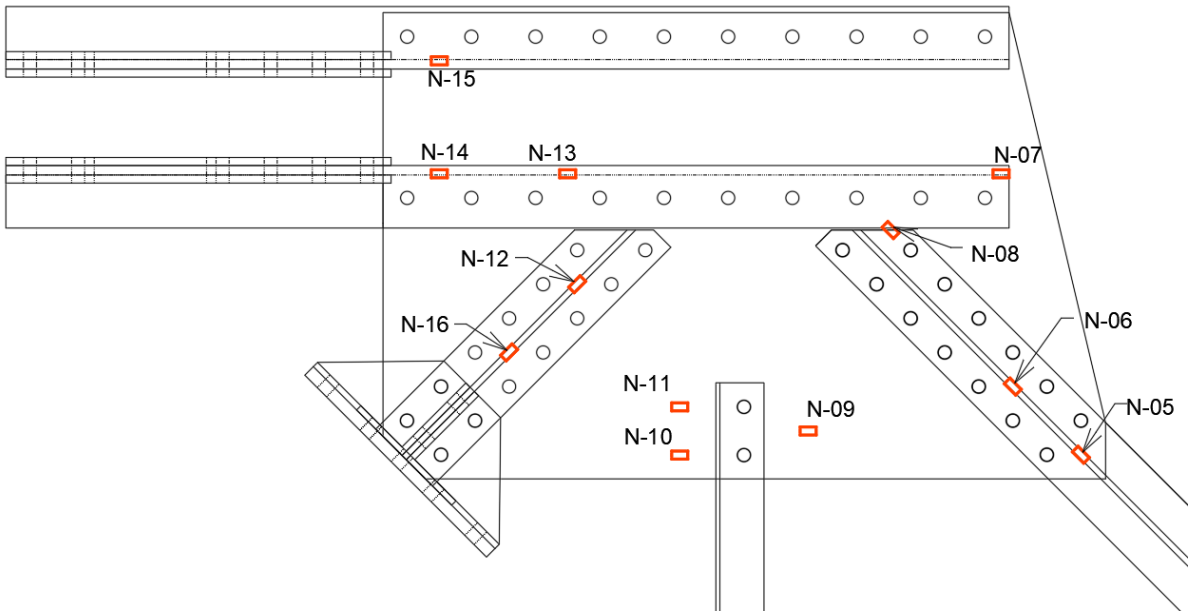

Figure 3-9 Strain gage labels for the north gusset

3.3.1 140 Kips test

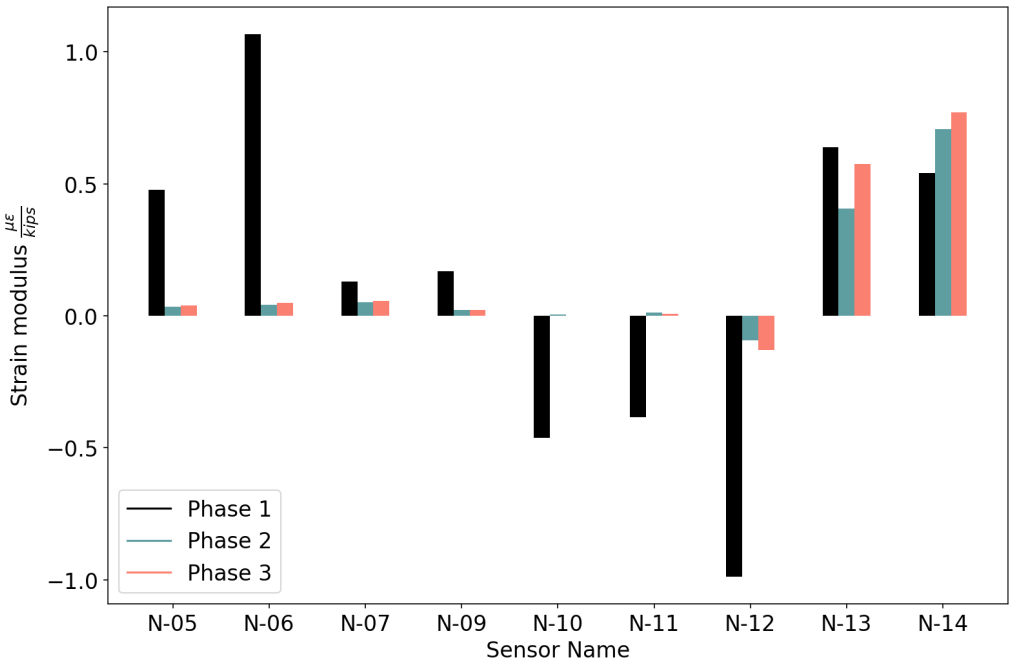

Figure 3-10 Strain modulus for tests with and without concrete for north gusset strain gages

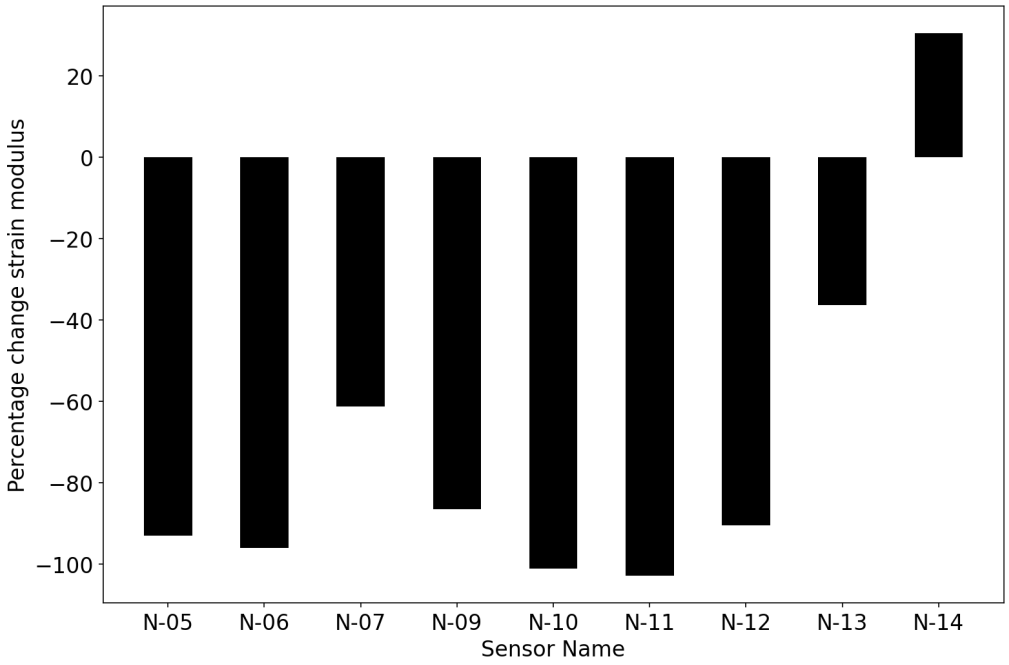

Figure 3-11 Percent change in strain modulus for strain gages on the north gusset for phase 2

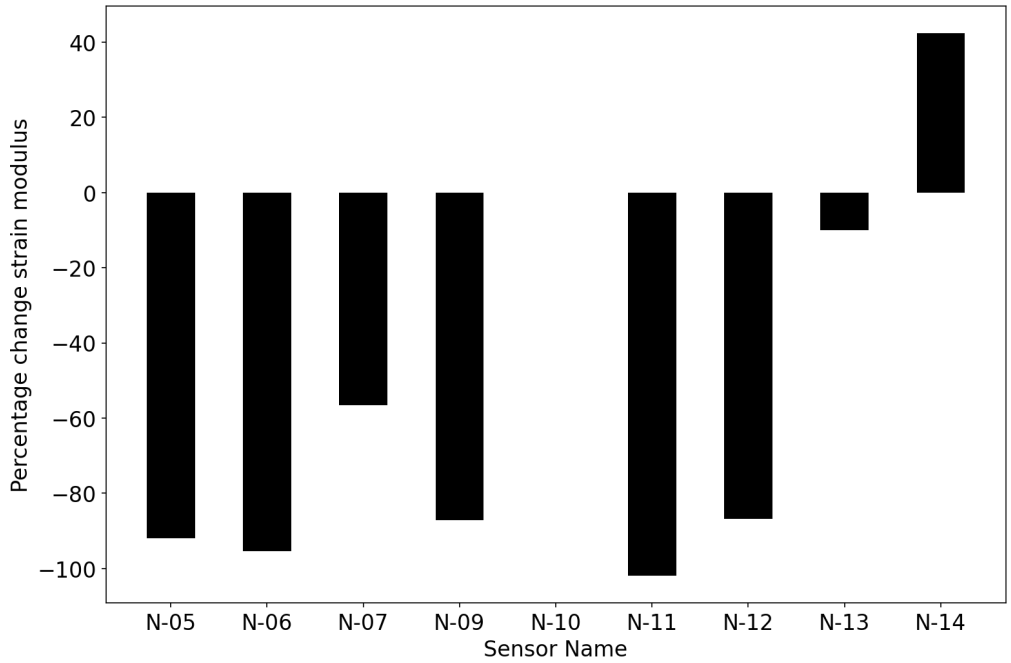

Figure 3-12. Percentage change in strain modulus for gages on north gusset plate for phase 3

Table 3-4 Strain moduli and R-squared values for gages on the north gusset

Sensor	Phase 1		Phase 2		Phase 3	
	$(\frac{\mu\epsilon}{kip})$	R^2	$(\frac{\mu\epsilon}{kip})$	R^2	$(\frac{\mu\epsilon}{kip})$	R^2
N-05	0.4777	0.98	0.0333	1	0.0385	1
N-06	1.0669	1	0.0415	1	0.0492	1
N-07	0.1305	0.98	0.0505	1	0.0566	0.99
N-08	1.0224	1	N/A	N/A	N/A	N/A
N-09	0.1688	0.97	0.0229	1	0.0218	0.98
N-10	-0.4624	0.98	0.0054	0.95	N/A	N/A
N-11	-0.3837	0.98	0.0111	0.98	0.0075	0.93
N-12	-0.9888	1	-0.0937	1	-0.1297	0.99
N-13	0.6394	0.99	0.4067	0.99	0.5756	0.99
N-14	0.5411	0.98	0.7063	0.99	0.7704	1
N-15	0.5855	0.99	N/A	N/A	N/A	N/A
N-16	-1.1274	1	N/A	N/A	N/A	N/A

3.3.2 Max load test

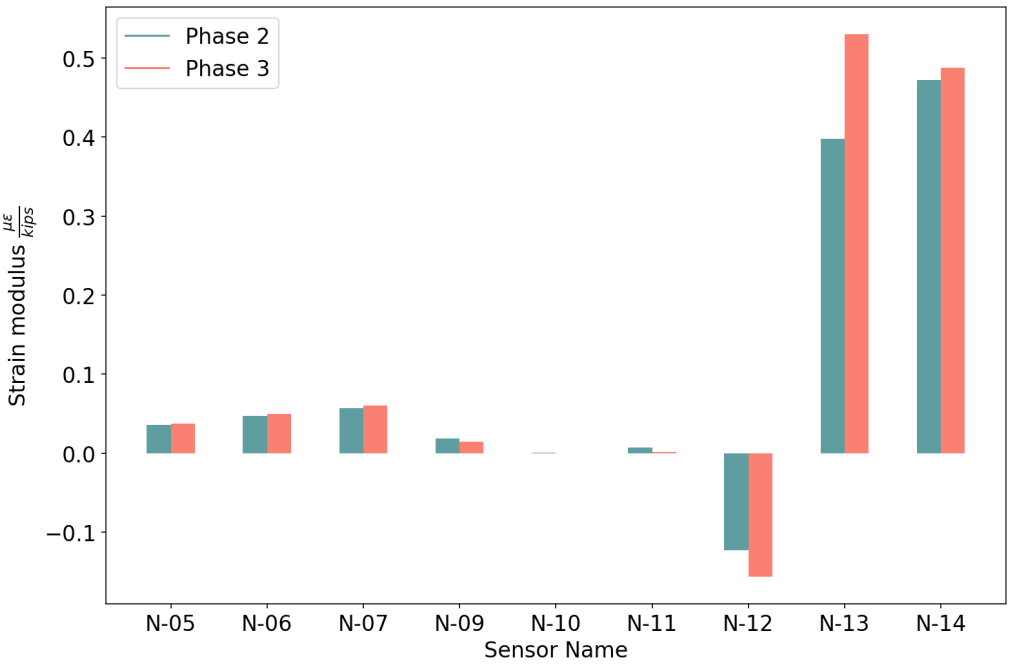

Figure 3-13Strain modulus for north gusset gages, max load tests

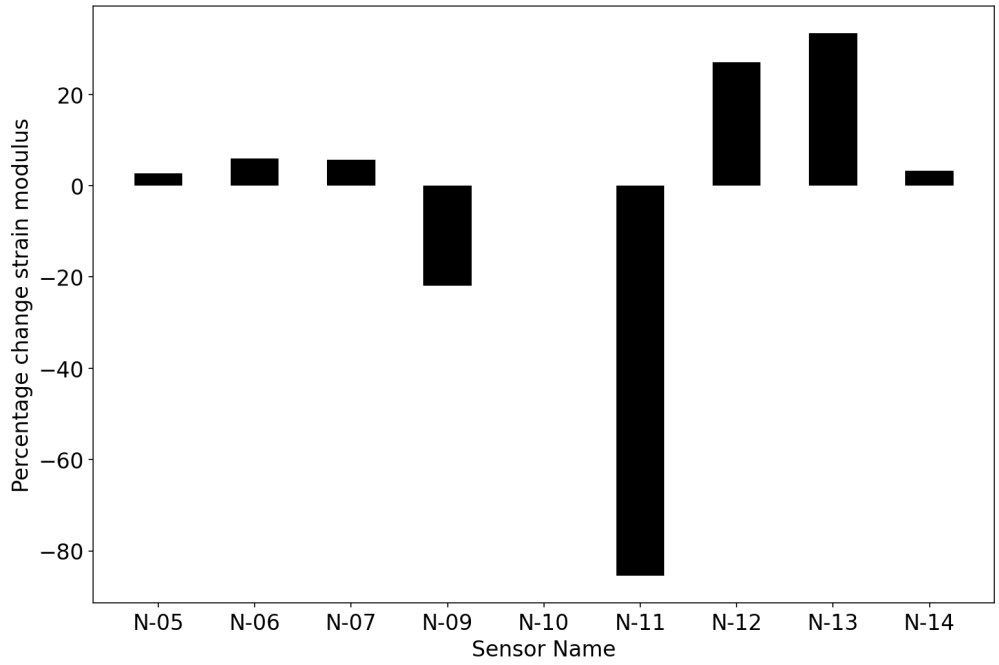

Figure 3-14 Percent change in strain modulus between phase 3 and phase 2, max load tests

Table 3-5 Strain modulus and r-squared values for north gusset gages, max load

Sensor	Phase 2		Phase 3	
	$(\frac{\mu\epsilon}{kip})$	R^2	$(\frac{\mu\epsilon}{kip})$	R^2
N-05	0.036	1	0.0401	1
N-06	0.0467	1	0.0517	1
N-07	0.0568	1	0.0613	0.99
N-09	0.0188	0.99	0.018	0.97
N-10	0.0007	0.18	N/A	N/A
N-11	0.0068	0.96	0.004	0.72
N-12	-0.1232	0.99	-0.1506	0.98
N-13	0.3974	1	0.5056	0.99
N-14	0.4723	0.95	0.4881	0.85

3.4 South Gusset

Approximate locations for the strain gages on the south gusset plate are shown in Figure 3-15. All gages on the south gusset plate are attached to the outside face of the plate. For clarity in the plots, results for the south gusset are divided into two arbitrary sets. The average strain moduli are shown in the bar plots of Figure 3-16 and Figure 3-17. The percentage change in strain moduli are shown in Figure 3-18 and Figure 3-19. All results are tabulated in Table 3-6. Note, plotted results are not shown for S-25 as this gage was damaged during the concrete pouring procedure.

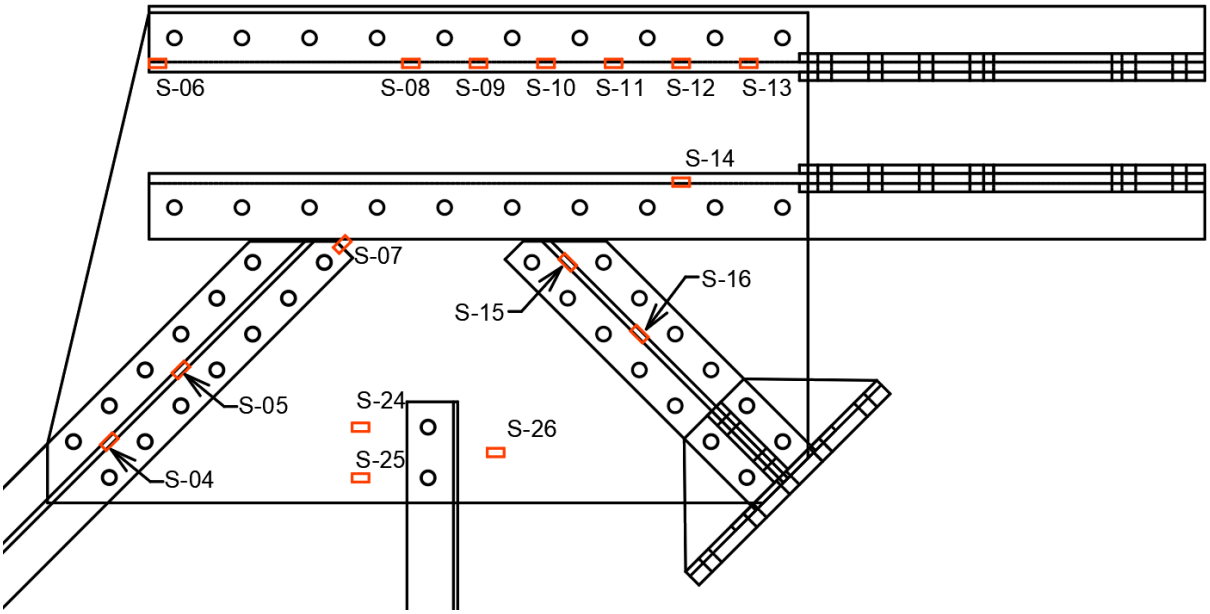

Figure 3-15 Labels for strain gages on the south gusset

3.4.1 140 kip tests

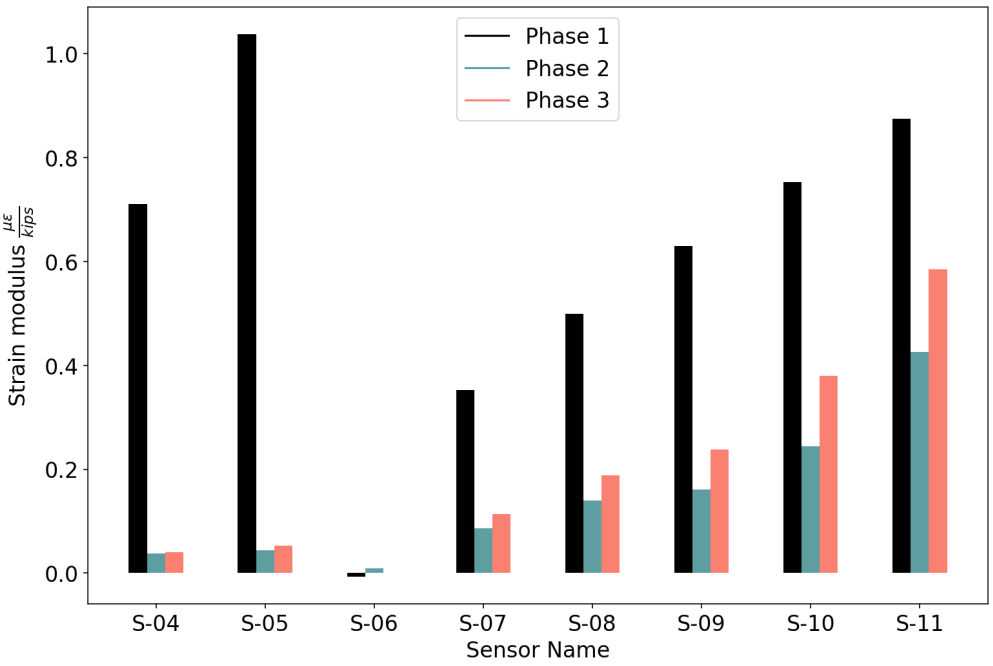

Figure 3-16 Strain modulus for tests with and without concrete for gages on the south gusset (first)

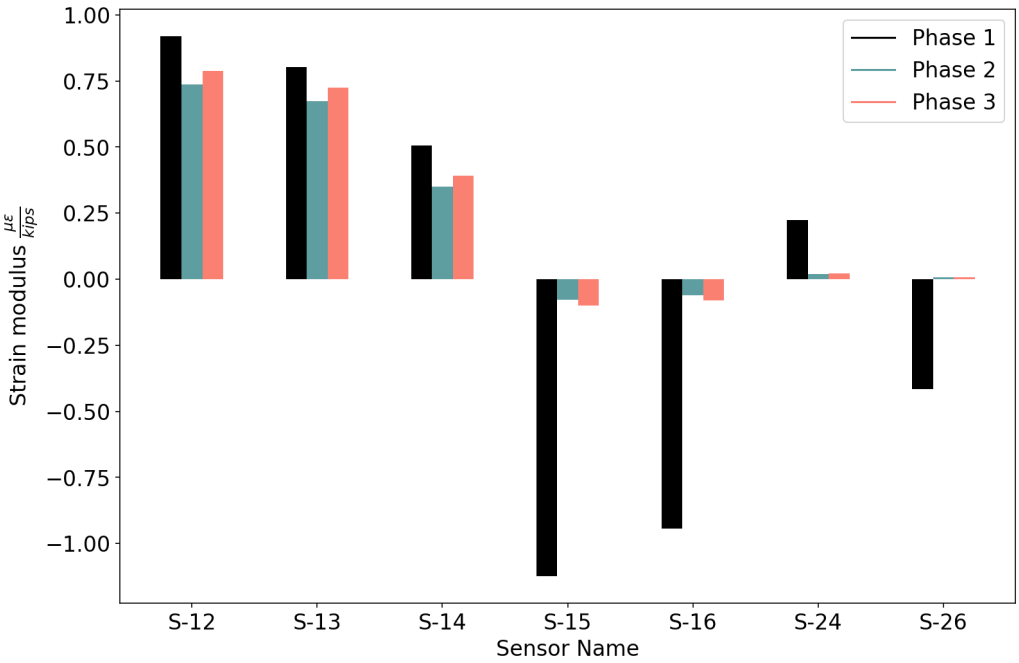

Figure 3-17 Strain modulus for tests with and without concrete for the remainder of gages on the south gusset

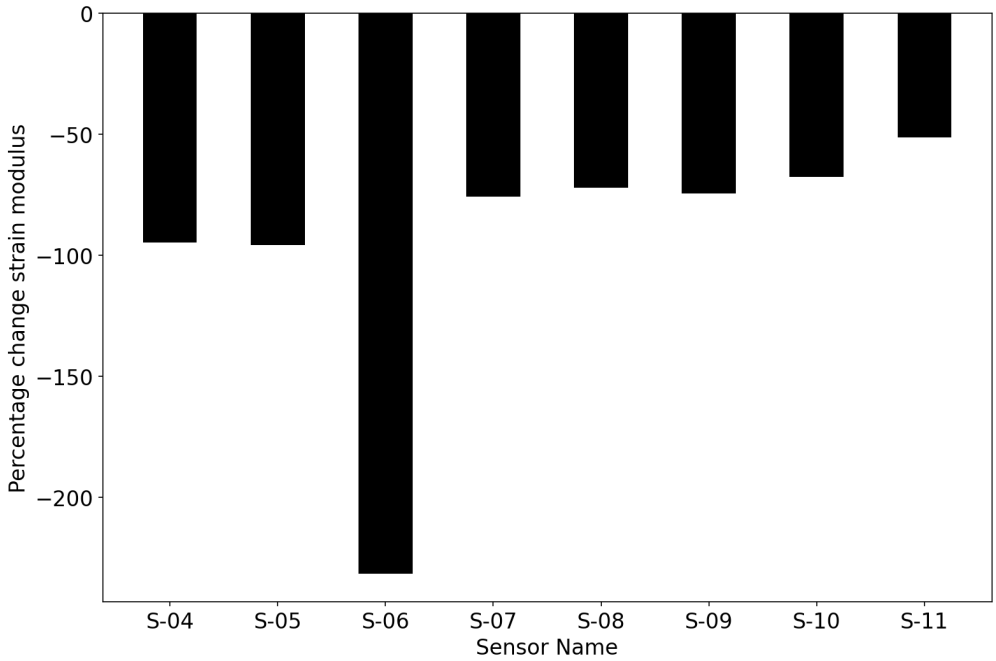

Figure 3-18 Percent change in strain modulus for south gusset gages, phase 2

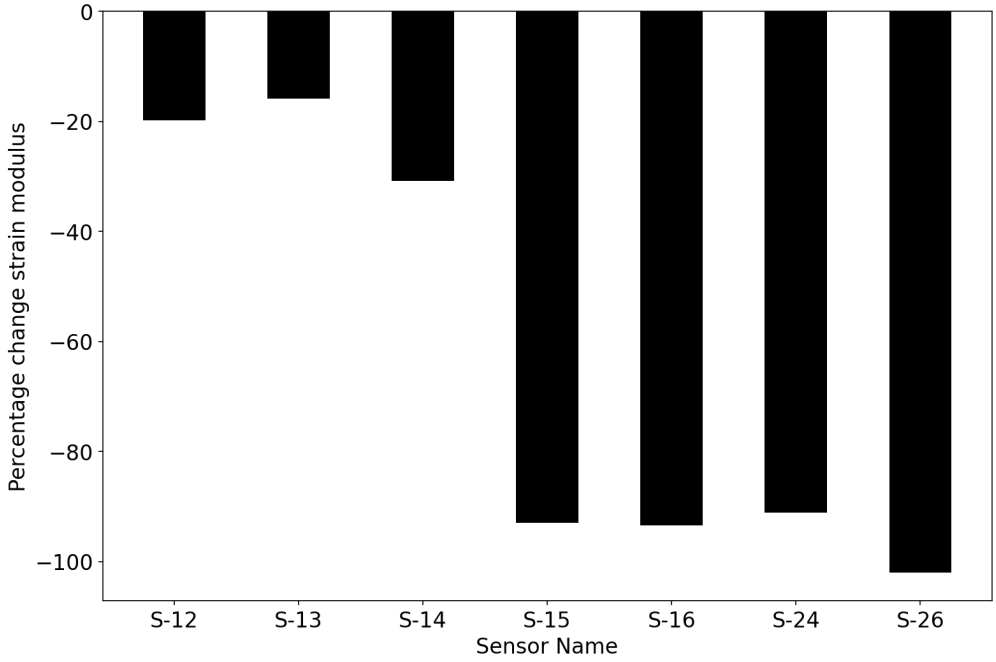

Figure 3-19. Percent change in strain modulus for the remainder of south gusset gages phase 2

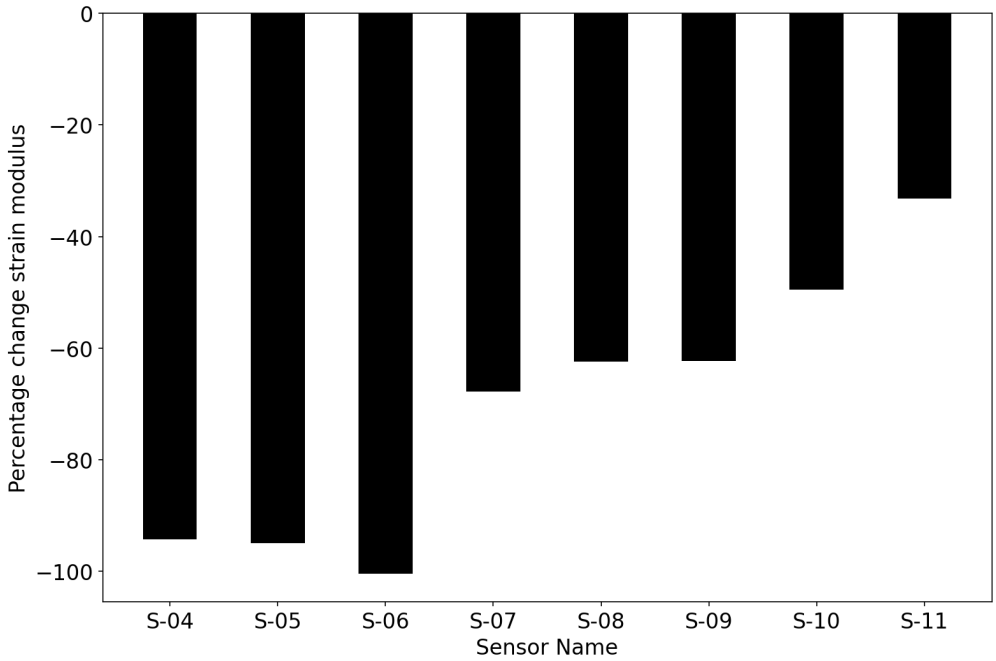

Figure 3-20 Percentage change in strain modulus for south gusset gages, phase 3

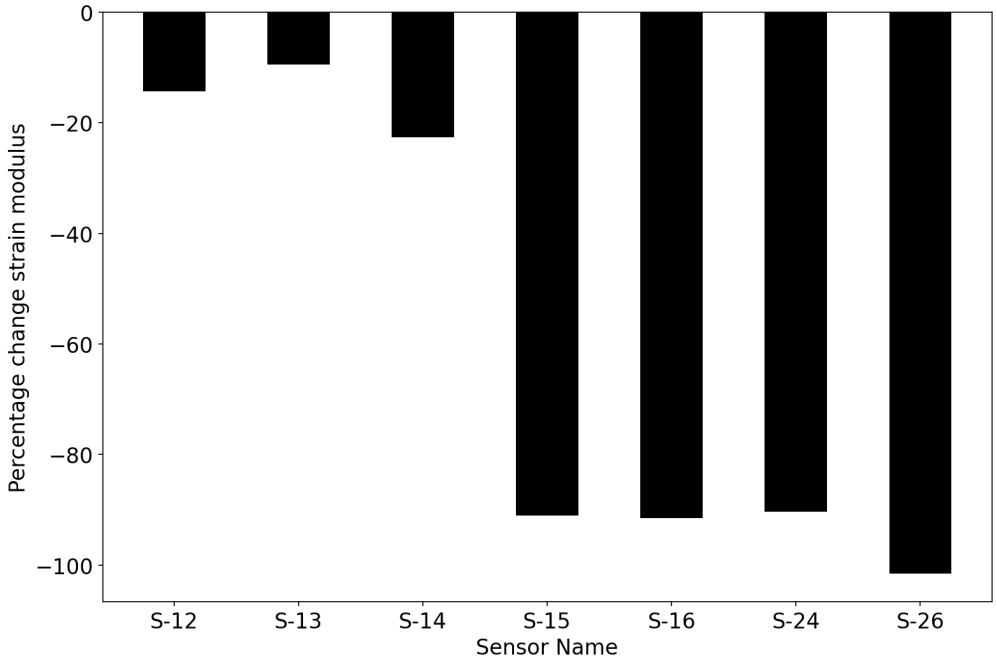

Figure 3-21 Percentage change in strain modulus for remainder of south gusset gages for phase 3

Table 3-6 strain moduli and R-squared values for gages on the south gusset

Sensor	Phase 1		Phase 2		Phase 3	
	$(\frac{\mu\epsilon}{kip})$	R^2	$(\frac{\mu\epsilon}{kip})$	R^2	$(\frac{\mu\epsilon}{kip})$	R^2
S-04	0.71	0.99	0.0373	1	0.0407	0.85
S-05	1.0375	1	0.044	1	0.0527	0.91
S-06	-0.0072	0.31	0.0094	0.93	N/A	N/A
S-07	0.3521	0.99	0.0857	1	0.1136	0.99
S-08	0.4986	0.99	0.1394	1	0.1876	0.99
S-09	0.6295	1	0.1611	1	0.2374	0.97
S-10	0.7523	1	0.2436	0.98	0.3797	0.98
S-11	0.8745	1	0.4262	0.98	0.5846	0.99
S-12	0.919	1	0.7366	0.99	0.7875	1
S-13	0.8016	0.97	0.6742	0.99	0.7254	1
S-14	0.5053	0.99	0.3494	0.98	0.3913	0.99
S-15	-1.1237	1	-0.0789	1	-0.1007	0.99
S-16	-0.9424	1	-0.0615	0.99	-0.0807	0.99
S-24	0.2239	0.96	0.0198	1	0.0215	0.99
S-25	0.1517	0.91	0.0466	0.26	-0.2423	0.06
S-26	-0.4162	0.99	0.0085	0.98	0.0064	0.94

3.4.2 Max Load tests

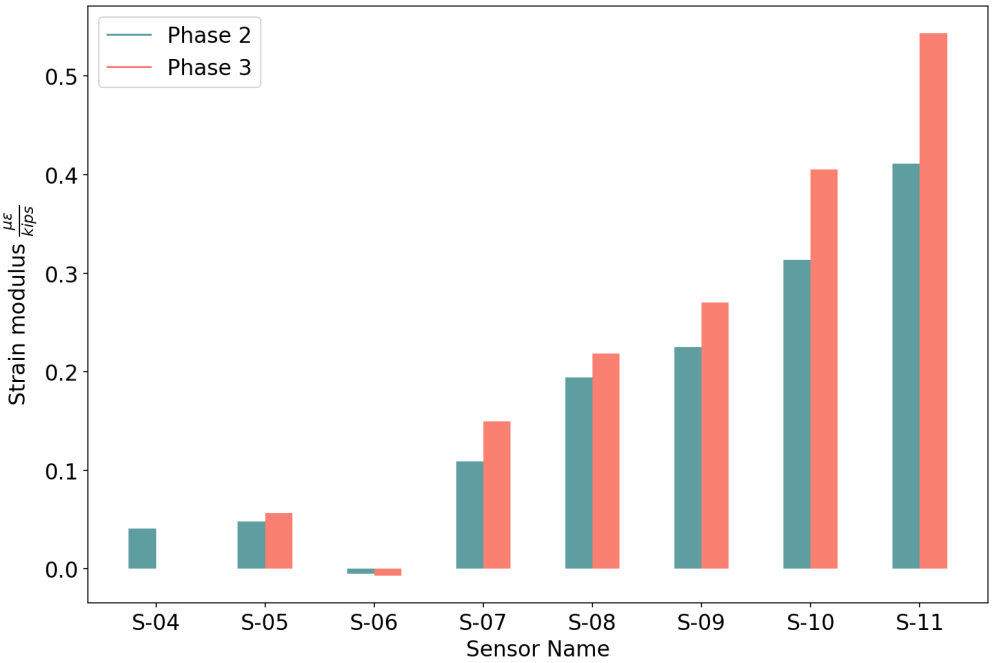

Figure 3-22 Strain Modulus for south gusset gages, max load

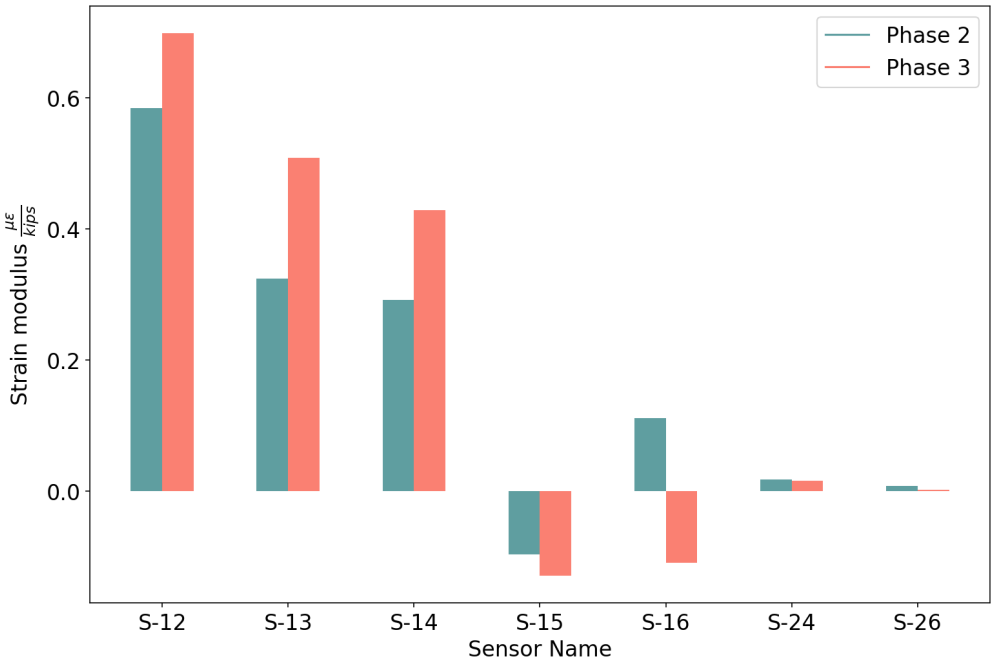

Figure 3-23 Strain modulus for remainder of south gusset gages, max load

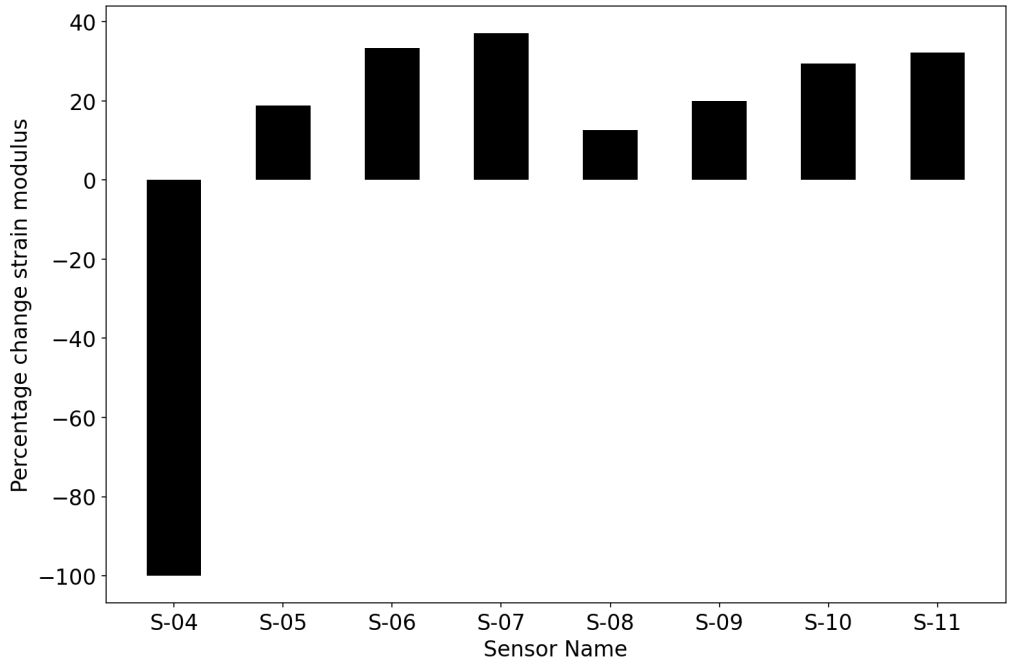

Figure 3-24 Percentage change between phase 3 and phase 2 for south gusset gages, max load

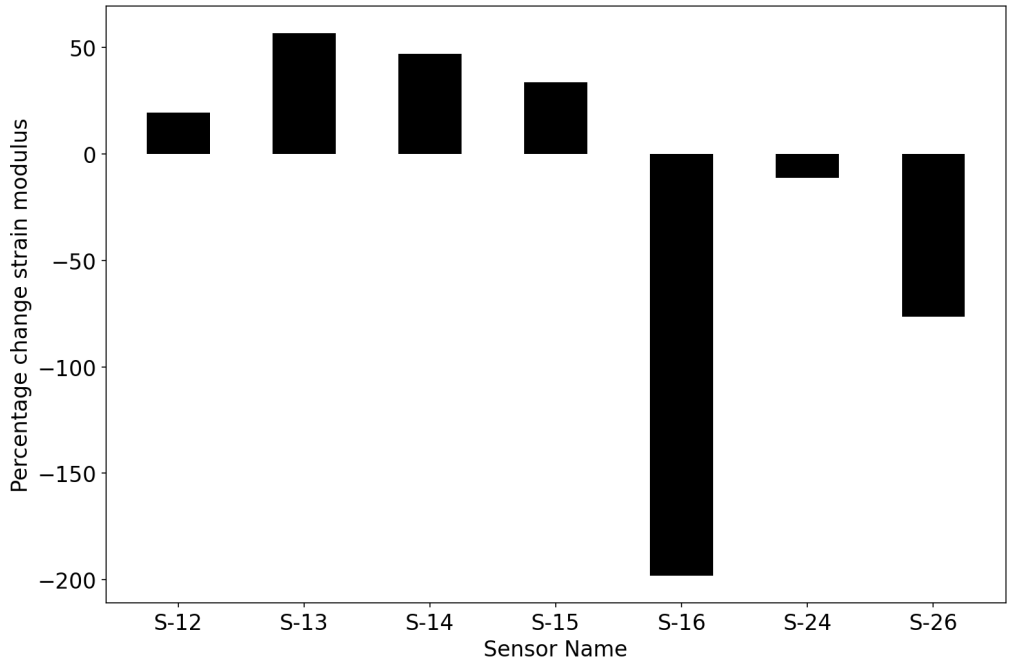

Figure 3-25 Percentage change between phase 3 and phase 2of remainder of south gusset gages, max load

Table 3-7 Strain modulus and r-squared values for south gusset gages, max load

Sensor	Phase 2		Phase 3	
	$(\frac{\mu\epsilon}{kip})$	R^2	$(\frac{\mu\epsilon}{kip})$	R^2
S-04	0.0406	1	0.0442	0.98
S-05	0.0478	1	0.0607	0.97
S-06	-0.0053	0.73	-0.009	0.79
S-07	0.1092	0.99	0.1514	0.97
S-08	0.1943	0.99	0.2192	0.99
S-09	0.2253	0.99	0.27	0.98
S-10	0.3133	0.98	0.405	0.99
S-11	0.4114	0.98	0.5529	0.99
S-12	0.5835	0.98	0.7034	0.99
S-13	0.3241	0.88	0.5112	0.89
S-14	0.2911	0.97	0.437	1
S-15	-0.0968	0.99	-0.1221	0.98
S-16	0.1113	0.81	-0.1021	0.99
S-24	0.0173	1	0.019	0.99
S-26	0.0078	0.96	0.0047	0.67

3.5 Tension Strut

The approximate locations for the strain gages on the tension strut are shown in Figure 3-26. All gages labeled with the prefix ‘T’ are on the web of the tension strut, while those labeled ‘N’

or ‘S’ are on the north or south flange, respectively. The average strain moduli for the gages on the tension strut are shown in Figure 3-27. The percentage change in strain moduli are shown Figure 3-28. All results are tabulated in Table 3-8. Note, for the tension strut, plotted results are not shown for N-01, N-02, N-03, T-02 and T-07. These gages were damaged either during installation or during the pouring of concrete, and so their readings are either null or suspect.

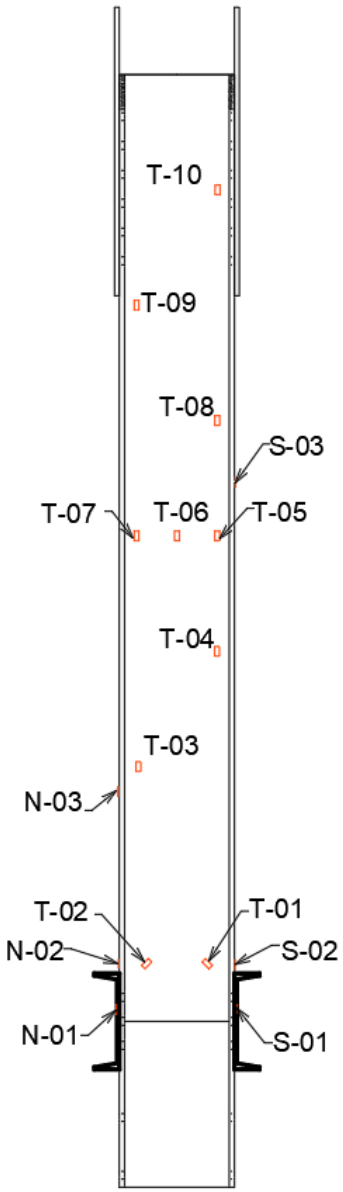

Figure 3-26 Labels for strain gages on the tension strut

3.5.1 140 kips tests

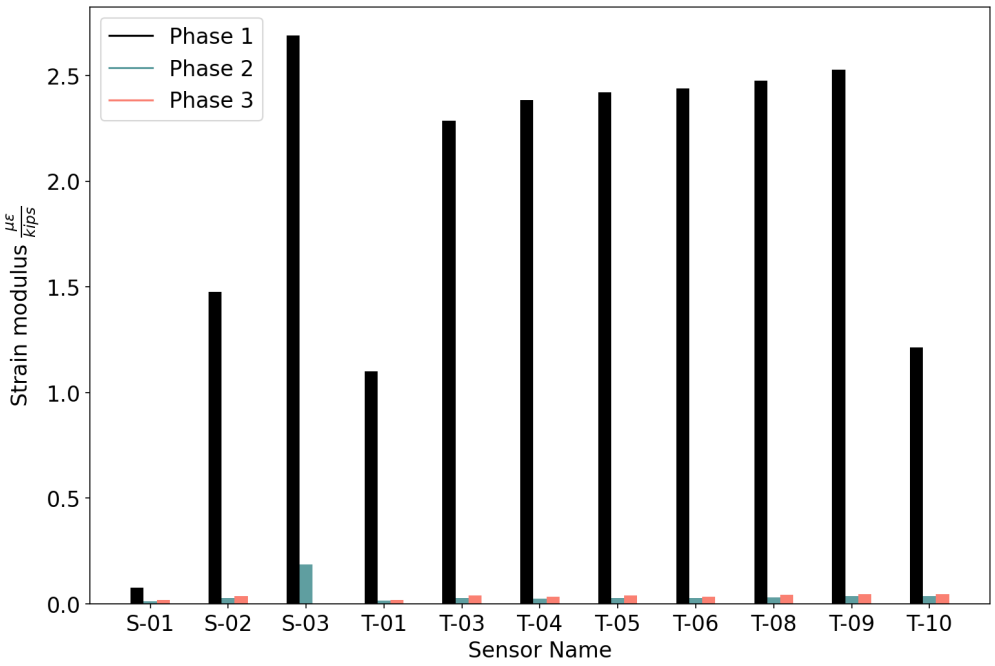

Figure 3-27 Strain modulus for tests with and without concrete for gages on the tension strut

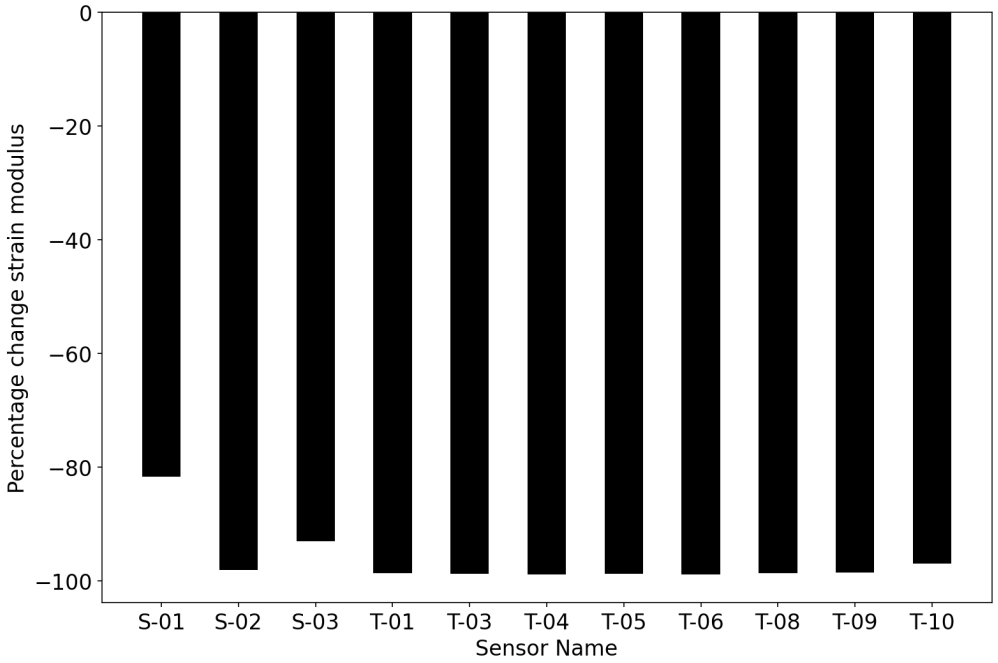

Figure 3-28 Percent change in strain modulus for gages on the tension strut, phase 2

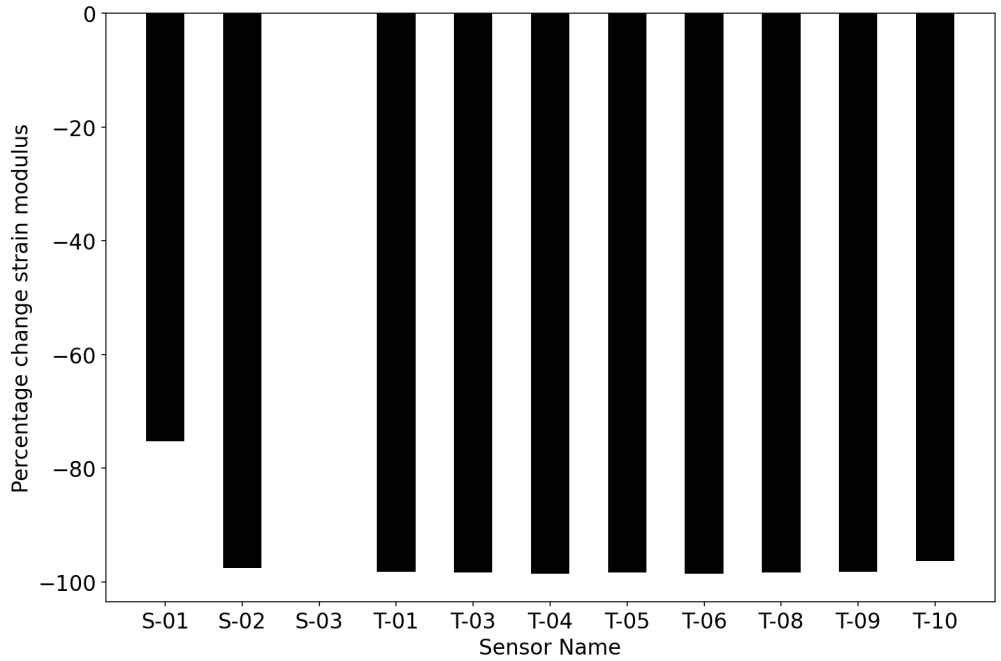

Figure 3-29. Percentage change in strain modulus for tension strut gages, phase 3

Table 3-8 Strain moduli and r-squared values for gages on the tension strut

Sensor	Phase 1		Phase 2		Phase 3	
	$(\frac{\mu\epsilon}{kip})$	R^2	$(\frac{\mu\epsilon}{kip})$	R^2	$(\frac{\mu\epsilon}{kip})$	R^2
N-01	0.3815	0.83	N/A	N/A	N/A	N/A
N-02	3.8224	0.99	N/A	N/A	N/A	N/A
N-03	-3.7502	0.12	0.5187	0.15	0.1106	0.09
S-01	0.0758	0.35	0.0138	0.99	0.0187	1
S-02	1.4759	0.94	0.0272	1	0.0365	0.98
S-03	2.689	1	0.1859	0.02	N/A	N/A
T-01	1.1017	0.98	0.0141	0.99	0.0193	0.97
T-02	0.938	0.99	N/A	N/A	N/A	N/A
T-03	2.2868	1	0.0288	1	0.0395	0.97
T-04	2.3823	1	0.0258	0.98	0.0348	0.99
T-05	2.4213	1	0.0279	1	0.0407	1
T-06	2.4382	1	0.0265	1	0.0353	1
T-07	2.4771	1	N/A	N/A	N/A	N/A
T-08	2.4741	1	0.0314	0.99	0.0427	1
T-09	2.5269	1	0.0371	1	0.0447	1
T-10	1.2125	1	0.0366	1	0.0453	0.96

3.5.2 Max load tests

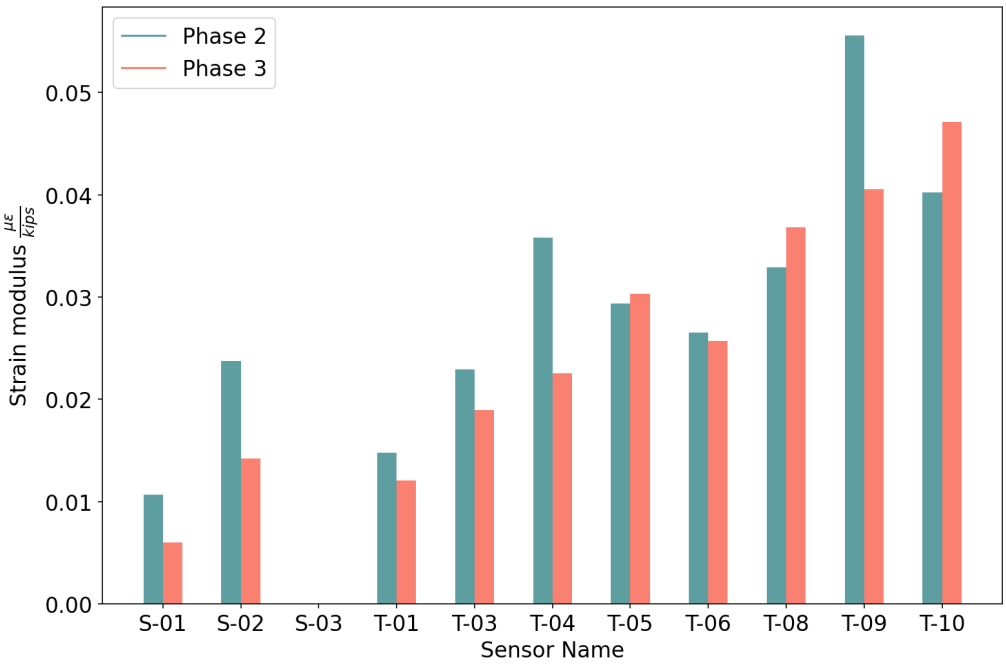

Figure 3-30 Strain modulus for tension strut gages, max load test

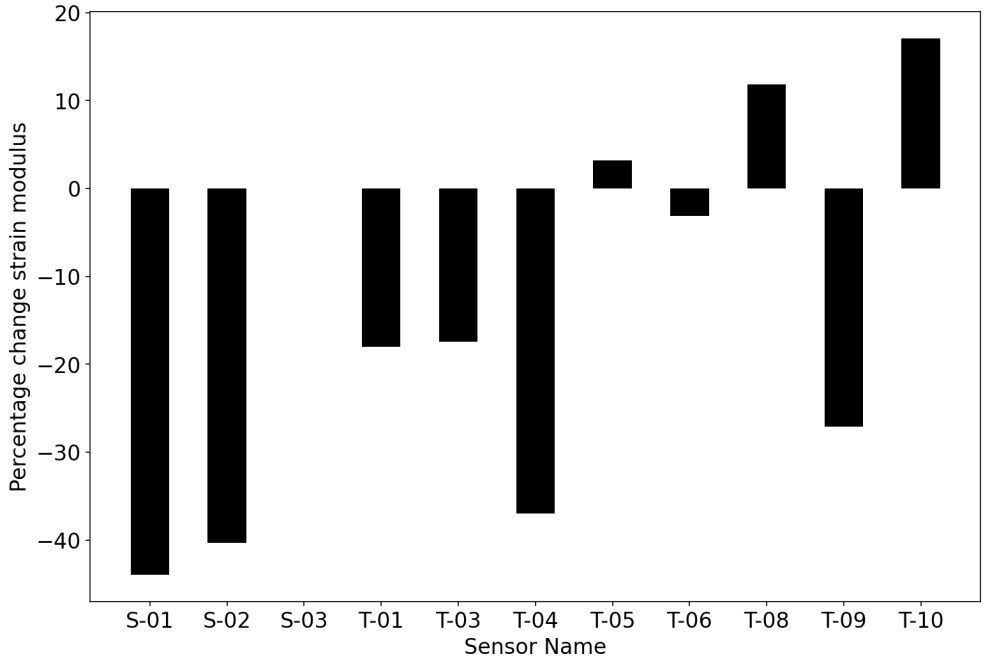

Figure 3-31 Percentage change strain modulus for tension strut gages, max load test

Table 3-9 Strain Modulus and R-squared values for tension strut gages, max load

Sensor	Phase 2		Phase 3	
	$(\frac{\mu\epsilon}{kip})$	R^2	$(\frac{\mu\epsilon}{kip})$	R^2
S-01	0.0107	0.98	0.0138	0.97
S-02	0.0238	0.99	0.0305	0.98
T-01	0.0148	1	0.0185	0.98
T-02	0.0478	0.04	N/A	N/A
T-03	0.023	1	0.0339	0.99
T-04	0.0358	0.76	0.0336	1
T-05	0.0293	1	0.0398	1
T-06	0.0265	1	0.0331	1
T-07	0.0231	0.34	N/A	N/A
T-08	0.0329	1	0.043	1
T-09	0.0556	0.91	0.0468	1
T-10	0.0402	1	0.049	0.99

3.6 Compression Strut

Approximate locations for the strain gages on the compression strut are shown in Figure 3-32 and Figure 3-33. Gages shown in red are on the outside face of the angle piece used for the compression foot of the strut. Gages shown in blue are on the inside face of the flanges of the compression strut itself. The average strain moduli for the gages on the compression strut are shown in Figure 3-34. The percentage change in strain moduli are shown in Figure 3-35. All results are tabulated in Table 3-10. Note, plotted results are not shown for S-17 and S-20 as these gages were damaged during the concrete pouring procedure. No data is available for gages N-20 and S-19, as these were damaged during initial installation.

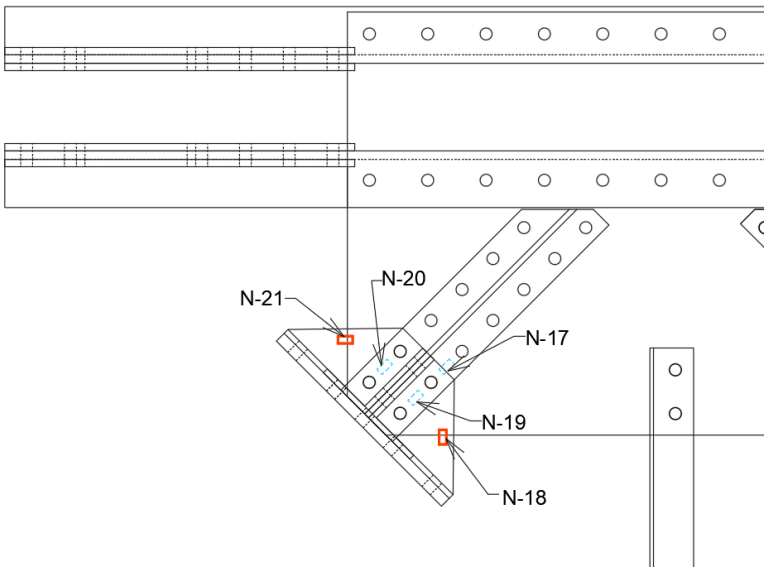

Figure 3-32 Labels for strain gages on north side of compression strut. Red gages are on the outside, blue gages are on the inside

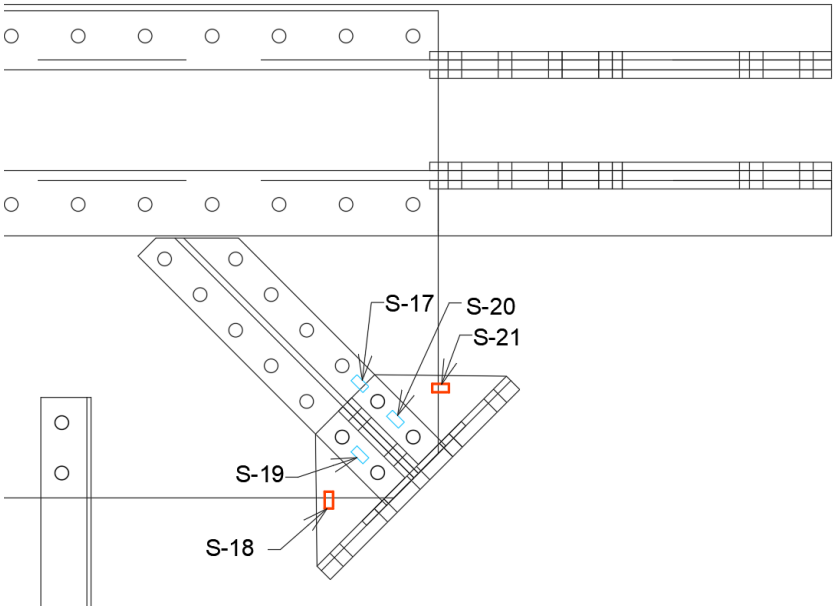

Figure 3-33 Labels for strain gages on the south side of the compression strut. Red gages are on the outside, blue gages on the inside.

3.6.1 140 kips tests

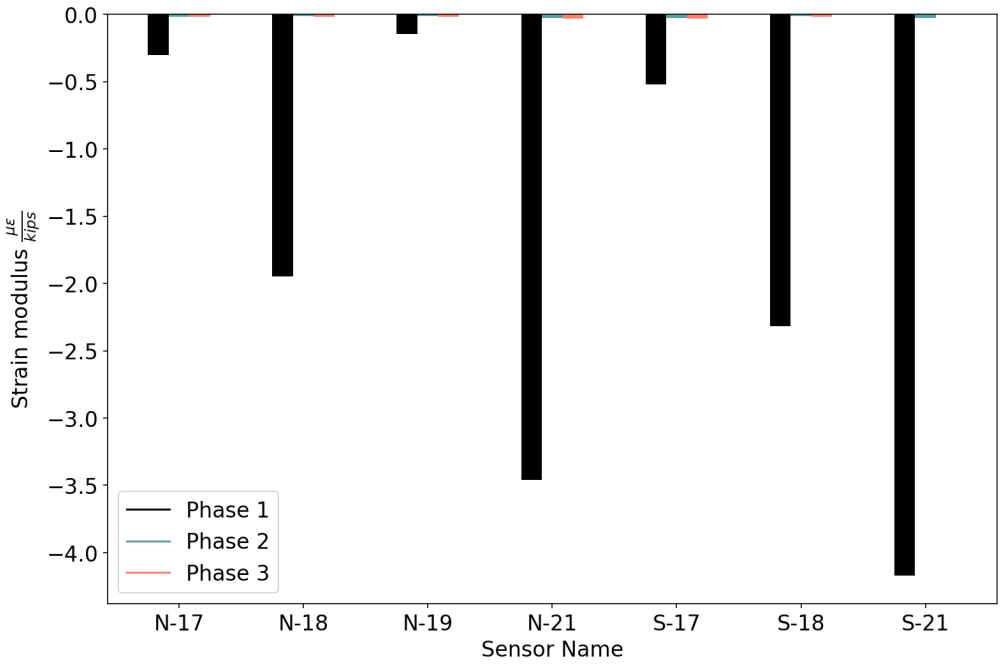

Figure 3-34 Strain modulus for tests with and without concrete for gages on the compression strut

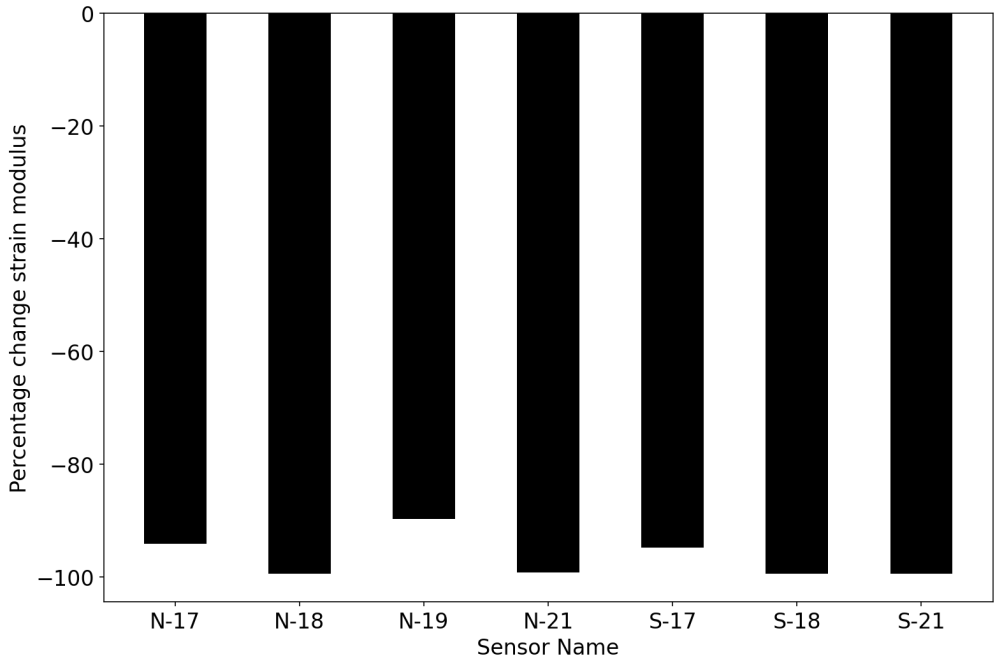

Figure 3-35 Percent change in strain modulus for gages on the compression strut, phase 2.

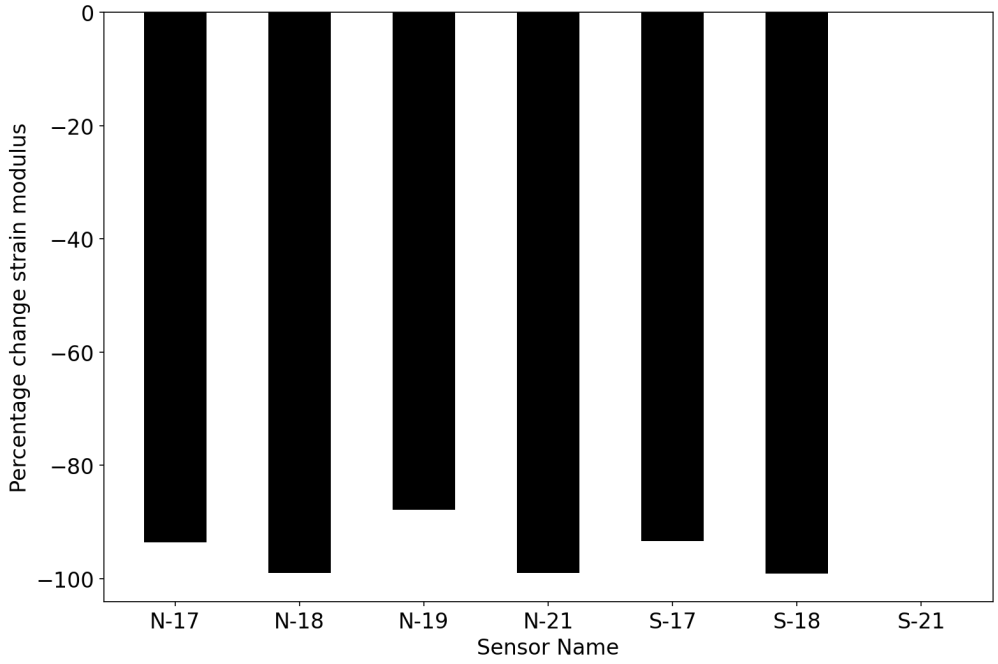

Figure 3-36 Percentage change in strain modulus for compression strut gages, phase 3

Table 3-10 Strain moduli and r-squared values for gages on the compression strut

Sensor	Phase 1		Phase 2		Phase 3	
	$(\frac{\mu\epsilon}{kip})$	R^2	$(\frac{\mu\epsilon}{kip})$	R^2	$(\frac{\mu\epsilon}{kip})$	R^2
S-17	-0.5232	0.97	-0.0273	0.54	-0.0348	0.94
S-18	-2.3193	0.94	-0.0137	0.96	-0.0197	0.93
S-20	-0.1948	0.58	N/A	N/A	N/A	N/A
S-21	-4.1712	0.98	-0.0266	0.99	N/A	N/A
N-17	-0.3051	0.92	-0.0181	0.99	-0.0195	0.91
N-18	-1.949	0.91	-0.0123	0.95	-0.0199	0.95
N-19	-0.1477	0.54	-0.0153	0.99	-0.0178	0.98
N-21	-3.4588	0.99	-0.0294	1	-0.0336	0.93

3.6.2 Max load tests

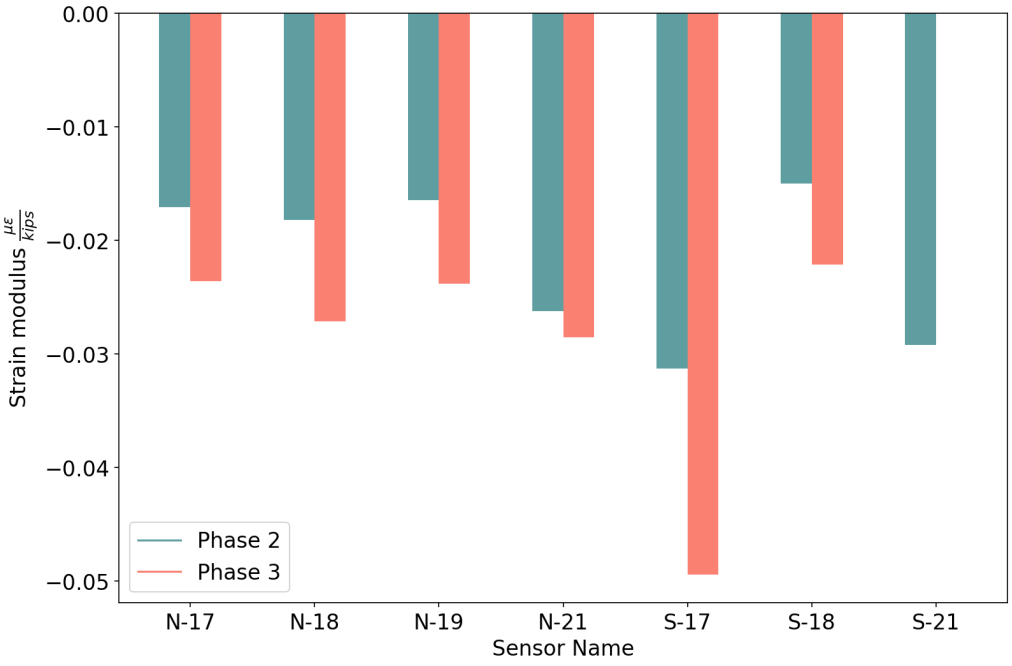

Figure 3-37 Strain modulus for compression strut gages, max load

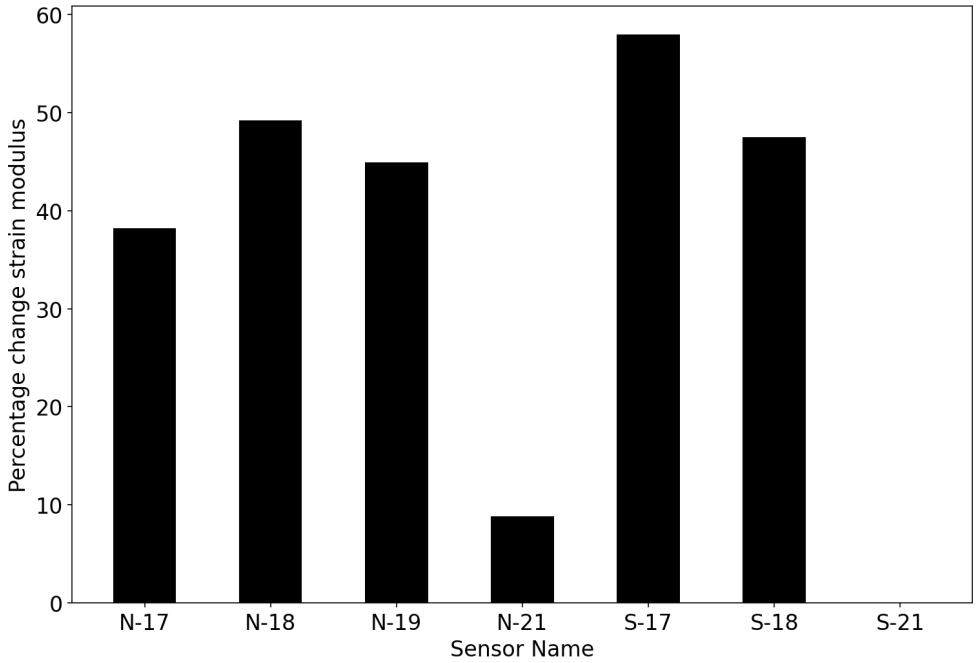

Figure 3-38 Percentage change between phase 3 and phase 2 for compression strut gages, max load

Table 3-11 Strain modulus and R-squared values for compression strut gages, max load

Sensor	Phase 2		Phase 3	
	$(\frac{\mu\epsilon}{kip})$	R^2	$(\frac{\mu\epsilon}{kip})$	R^2
N-17	-0.0171	1	-0.0196	0.97
N-18	-0.0182	0.99	-0.0233	0.96
N-19	-0.0164	1	-0.0199	0.99
N-21	-0.0262	0.98	-0.0276	0.99
S-17	-0.0313	0.95	-0.0413	0.96
S-18	-0.015	1	-0.0183	0.97
S-21	-0.0292	0.99	N/A	N/A

DISCUSSION

In the results shown in the previous section, some issues stand out from the data. First, the complicated nature of the contact phenomenon that occurs near the supports for the phase 1 test makes a one-to-one comparison of nearby gages between phase 1 and the other two phases difficult. This is particularly the case at N-18, N-19, S-01 and S-02. These gages show either a curvilinear, or bilinear, response during the phase 1 test. This is highlighted in the small R2 values of the OLS fit seen in the tables, and can be corroborated from the data plots provided in the Appendix. It is suspected that this behavior is due to a change in the state of contact of the specimen at the support locations that is not seen in the phase 2 test (because those supports are no longer used). Thus, discretion must be used when comparing the results of these gages.

Next, multiple strain gages were damaged or destroyed during the concrete pouring procedure. Those gages are N-01, N-02, N-03, N-08, N15, N-16, N-22, S-17, S-20, S-25, T-02, and T-07. The loss of gages was an expected outcome from the concrete pouring procedure, which was a primary motivation for the inclusion of what may have been seen as an otherwise excessive amount of strain gages. In spite of the loss of the gages listed above, there is adequate information to describe the behavior of the anchorage.

On the unembedded portion of the anchorage specimen, the two strain gages located near the center-line of the channels, B-01 and T-11, display consistent behavior. This consistency is expected as the unembedded portion should not be significantly impacted by the presence of concrete. Moreover, the location of these two gages along the center line of the channels is such that they will not be sensitive to any bending in the channels. The remainder of the unemebedded strain gages show somewhat significantly varying behavior. These strain gages are all located on the flanges of the channels and are thus sensitive to bending that may be caused by inconsistencies with load direction between tests. These inconsistencies in direction of load are likely to be caused by the addition of the concrete block, and the shifting of the specimen between phases 1 and then 2 and 3. Moreover, for the sake of the tests performed herein, the unembedded portions of the anchorages are not of particular interest given that, in the field, they are easily inspected. Thus, fatigue damage such as cracking can be found via visual inspection and quickly mitigated.

For the remaining gages on the embedded portions of the specimen, the behavior is mostly consistent with the numerical modeling results, wherein the presence of the embedding concrete significantly reduces the stress in the steel. On exception to this typical behavior is gage N-14, near the interface of the concrete. The strain modulus of 0.70 $\frac{\mu\epsilon}{kip}$ in phase 2 and 0.77 $\frac{\mu\epsilon}{kip}$ in phase 3 are both larger than the strain modulus of 0.54 $\frac{\mu\epsilon}{kip}$ in phase 1. It is expected that this increase is due to the fact that this gage is near the concrete interface, and likely caused be the bending that saw similar increases on the unembedded gages.

4.1 Updating fatigue analysis

For reinvestigating the AASHTO-based fatigue analysis, it is of particular interest to investigate the critical strain modulus on each of the components. The critical strain modulus here is taken as the modulus with the highest absolute value in either phase 2 or 3. For the tension strut,

the critical strain modulus is from gage T-09, with a value of 0.04 $\frac{\mu\epsilon}{kip}$ in phase 3. For the compression strut the critical strain modulus is from gage S-17, with a value of -0.04 $\frac{\mu\epsilon}{kip}$ in phase 3 (note, the negative value means this would be in compression). Across the gages on both gusset plates, the critical strain modulus is from gage S-12, with a value of 0.79 $\frac{\mu\epsilon}{kip}$ in phase 3.

For the component likely to be of most interest to the practicing engineer, the tension strut, the maximum strain modulus of 0.04 με/kips for gage T-09 is used to update the AASHTO analysis. An estimate of the stress range, $(\Delta f)_{eff}$ is found by multiplying the strain modulus by the Young's modulus of steel of 29,000 ksi, then multiplying by the overturning reaction caused by the hanging gate (which is analogous to the applied load during the test). The largest force in the tension strut in Table 1-1 is 125 kips, which corresponds to an overturning moment of the miter gate of 177 kips. Using the strain modulus, a stress of 205 psi could be expected in the tension strut of the anchorage. This stress is well below the endurance limit for steel, which is typically taken as 35% to 50% of the yield strength of steel (Suresh, 2012). Using the AASHTO definition for minimum constant amplitude fatigue threshold (analogous to the endurance limit), the lowest value across all fatigue detail categories is 2.6 ksi for fatigue detail category E', based on Table 6.6.1.2.5-3 in the AASHTO (2017) LRFD Bridge Design Manual. The typically assumed fatigue detail for miter gate anchorages is category D. For category D, the constant amplitude fatigue threshold is given as 7.0 ksi. Based on the results of this study, a design engineer following code-based guidance would find no need to consider a fatigue limit state for calculating structural capacity of either the tension strut or compression strut of miter gate anchorages.

For the gusset plates, the max strain modulus is 0.74 με/kips. As described above, the maximum force due to the overturning moment of the miter gate experienced by the miter gate anchorages considered in this study is 787 kN (177 kips). Thus, multiplying this value by the max gusset plate strain modulus and the modulus of elasticity of steel, and max stress of 3.8 ksi is expected is expected in the gusset plates. As described above, for the fatigue category D with constant amplitude fatigue threshold of 7.0 ksi, the design engineer would again need not consider fatigue limit states when designing the gusset plates. The discussion above of course assumes the condition of the concrete, steel, and steel-concrete bonding in the field are similar to those in the tests performed as part of this study for the life of the miter gate anchorage. For miter gate anchorages in the field, the practicing engineer should carefully assess on-site conditions when applying the results of this study. If the design engineer were being conservative and assumed a fatigue detail category E', equation (1) would be revisited with a $(\Delta f)_{eff}$ now equal to 3.8 ksi. For the critical case of Lock 14, found to be 12 years over its fatigue life in Table 1-1, the updated analysis shows that there would be an expected addition 7500 years of operation before a fatigue failure is expected.

CONCLUSIONS

In this study, a full-scale test of an embedded miter gate anchorage was performed to assess the contribution of concrete stiffness to structural behavior and make realistic fatigue life estimates. A full-scale test specimen was fabricated to the specifications of a typical in-service and representative miter gate anchorage. The test was performed in three phases. In phase 1, the test specimen was supported to mimic the boundary conditions assumed in the traditional analysis approach where the miter gate anchorage is assumed to behave as a freestanding, unembedded truss. In phase 2, the specimen was cast in a block of concrete to simulate the in-situ conditions of a primary miter gate anchorage. In phase 3, a portion of the concrete was cut away to simulate the conditions of a typical secondary miter gate anchorage. In all phases, the specimen was instrumented with 58 strain gages and the strain response was recorded while the specimen was placed under load applied by two synchronized actuators.

Results show that, on the tension strut, which is the component of primary concern to field engineers, the tensile strain reduces by nearly 100 percent when the specimen is embedded in concrete. Using the typical loads for a selection of representative miter gate anchorages on the Mississippi river in conjunction with the calculated strain moduli, it was seen that the stress in the tension strut is likely below typical endurance limits for steel and below the AASHTO code-based fatigue threshold used in practice. The results of this study support the notion that, for miter gate anchorages of similar construction and embedment, the cyclic stress amplitude is likely insignificant for much of the embedded steel. Replacement of the entire miter gate anchorage thus may not be necessary. However, for in-service miter gate anchorages, the condition of the embedding concrete and the extent at which the embedding steel is bonded to concrete is difficult to evaluate. Similarly, deterioration of materials over age may influence material strength and global stiffness of the embedded anchorage assembly. Engineers should carefully consider on-site conditions prior to leveraging the results of this study for rehab or repair decisions. Additionally, the exposed portions of miter gate anchorages have been subjected to decades of environmental degradation, which could accelerate fatigue failure. Therefore, engineers could consider at a minimum excavating and replacing the channels and reinforcing the gusset plates in the regions near the face of concrete. This limited upgrade scheme would eliminate the need to fabricate and replace the entire anchorage and would still result in substantial savings in construction cost. Future work will utilize the results from this study to rigorously quantify the interaction between steel and concrete in miter gate anchorages and update numerical models with accurate interaction properties, allowing for more robust designs and accurate lifecycle analysis for these critical components.

REFERENCES

[1] U.S. Army Corps of Engineers, *Engineering and Design: Lock Gates and Operating Equipment; EM 1110-2-2703,* Washington DC: USACE, 1994.

[2] PIANC, "Miter Gate Design and Operation. WG Report No. 154-2017," PIANC, Brussels, 2017.

[3] B. A. Eick, Structural Health Monitoring of Inland Navigation Infrastructure, Urbana, IL: University of Illinois, 2020.

[4] T. J. Kelley, "Choke Point of a Nation: The High Cost of an Aging River Lock," *The New York Times,* 23 11 2016.

[5] M. Gillerman, "Barge Traffic Moving Again on Mississippi River," *St. Louis Post Dispatch,* 23 01 2013.

[6] American Association of State Highway and Transportation Officials, AASHTO Manual for Bridge Evaluation, Washington DC: AASHTO, 2011.

[7] A. Wöhler, "Versuche zur Ermittelung der auf die Eisenbahnwagen-Achsen einwirkenden Kräfte und der Wiederstandsfähigkeit der Wagen-Achsen. (Tests on railway wagon axles. Forces and capacity. In German)," *Zeitschrift für das Bauwesen,* vol. 10, pp. 583-616, 1860.

[8] O. H. Basquin, "The Exponential Law of Endurance Tests," *Proceedings of the American Societry for Testing and Materials,* pp. 625-630, 1910.

[9] M. A. Miner, "Cumulative Damage in Fatigue," *Journal of Applied Mechanics,* pp. 149-164, 1945.

[10] R. Lackner and H. A. Mang, "Scale transition in steel-concrete interaction. I: Model," *Journal of Engineering Mechanics,* vol. 129, no. 4, pp. 393-402, 2003-a.

[11] R. Lackner and H. Mang, "Scale Transistion in Steel-Concrete Interaction. II: Applications," *Journal of Engineering Mechanics,* vol. 129, no. 4, pp. 403-413, 2003-b.

[12] International Federation for Structural Concrete (fib), "Bond of reinforcement in concrete (Bulletin No. 10)," International Federation for Structural Concrete, Lausanne, 2000.

[13] M. Ghandehari, S. Krishnaswamy and S. Shah, "Technique for evaluating kinematics between rebar and concrete," *Journal of Engineering Mechanics,* vol. 125, no. 2, pp. 234-241, 1999.

[14] M. H. Harajli, M. Hout and W. Jalkh, "Local bond stress-slip behavior of reinforcing bars embedded in plain and fiber concrete," *ACI Materials Journal,* vol. 92, no. 4, pp. 343-354, 1995.

[15] M. H. Lai and J. C. M. Ho, "A theoretical axial stress-strain model for circular concrete-filled-steel-tube columns," *Engineering Structures,* vol. 125, no. 2016, pp. 124-143, 2016.

[16] A. Elremaily and A. Azizinamini, "Behavior and strength of circular concrete-filled tube columns," *Journal of Constructional steel research,* vol. 58, no. 2002, pp. 1567-1591, 2002.

[17] J. F. Natalli, E. M. Xavier, L. C. Barbosa Costa, B. H. Rodrigues, A. M. Cunha Sarmanho and R. A. Fiorotti Peixoto, "New methodology to analyze the steel-concrete bond in CFST filled with lightweight and conventional concrete," *Material and Structures,* vol. 54, no. 13 (2021), 2021.

[18] R. Gutierrez, L. Stempniewski and F. Wagner, "Modelling steel-concrete interaction using the extended finite element method," *Obras y Proyectos,* no. 24, pp. 6-12, 2018.

[19] J. Moon, D. E. Lehman, C. W. Roeder, H.-E. Lee and T.-H. Lee, "Analytical evaluation of reinforced concrete pier and cast-in-steel-shell pile connection behavior considering steel-concrete interface," *Advances in Materials Science and Engineering,* vol. 2016, 2016.

[20] J. Santos and A. A. Henriques, "New finite element to model bond-slip with steel strain effect for the analysis of reinforced concrete structures," *Engineering structures,* vol. 86, no. 2015, pp. 72-83, 2015.

[21] B. A. Eick, M. D. Smith and T. B. Fillmore, "Feasibility of retrofitting existing miter-type lock gates with discontinuous contact blocks," *Journal of Structural Integrity and Maintenance,* vol. 4, no. 4, pp. 179-194, 2019.

[22] J. P. Hartman, J. D. Gibson and M. D. Nelson, "Finite Element Studies of a Horizontally Framed Miter Gate; Technical Report ITL-87-4," US Army Engineer Waterways Experiment Station, Vicksburg, 1987.

[23] G. A. Riveros, J. L. Ayala-Burgos and D. Dixon, "Numerical Investigation of Diagonals in Miter Gates: Looking for the Optimum Prestressing," *Journal of Performance of Constructed Facilities,* vol. 31, no. 1, 2017.

[24] N. M. Levine, B. A. Eick, E. O. Johnson, B. F. Spencer and M. D. Smith, "Predicting fatigue life of miter gate anchorages with stochastic modeling and limited sensor data," in *12th International Workshop on Structural Health Monitoring*, Stanford, 2019.

[25] P. Soroushian, K. Obaseki and M. C. Rojas, "Bearing Strength and Stiffness of Concrete Under Reinforcing Bars (Title No. 84-M19)," *ACI Materials Journal,* no. May-June, pp. 179-184, 1987.

[26] B. A. Eick, M. D. Smith and S. Foltz, "Field testing to quantify the interaction of steel and concrete for miter gate anchorages," ERDC-CERL, Champaign, 2020.

[27] B. A. Eick, N. M. Levine, M. D. Smith and B. F. Spencer, Jr., "Fatigue life updating of embedded miter gate anchorages of navigation locks using full-scale laboratory testing," *Structure and Infrastructure Engineering,* ACCEPTED 2021.

[28] ASTM C39 / C39M-20, Standard Test Method for Compressive Strength of Cylindrical Concrete Specimens, West Conshohocken, PA: ASTM International.

[29] Micro-measurements, "General Purpose Strain gages," [Online]. Available: https://docs.micro-measurements.com/?id=2590. [Accessed 12 01 2021].

[30] Micro-measurements, "Strain gage adhesive," [Online]. Available: http://www.vishaypg.com/docs/11010/bond200.pdf. [Accessed 12 01 2021].

[31] National Instruments, SCXI CHassis User Manual, Austin, TX, 2006.

[32] National Instruments, SCXI-1520 user manual, Austin, TX, 2009.

[33] National Instruments, SCXI-1314 Universal Strain Terminal Block, Austin, TX, 2000.

[34] National Instruments, SignalExpress: Getting Started with SignalExpress, Auistin, TX, 2013.

[35] SciPy Community, "SciPy Least Square Documentation," 05 May 2018. [Online]. Available: https://docs.scipy.org/doc/scipy/reference/generated/scipy.optimize.least_squares.html. [Accessed 07 December 2017].

[36] C. W. de Silva, Vibration: Fundamentals and Practice, Second Edition, Boca Raton, FL: Taylor and Francis Group, 2006.

[37] Hogg, McKean and Craig, Introduction to Mathematical Statistics, Pearsons, 2018.

[38] S. J. Sheather, A Modern Approach to Regression with R, New York: Springer, 2009.

APPENDIX A : ALL DATA

In this appendix, plots for all gages showing the strain vs. load response are provided. In each plot, the black series represent the phase 1 tests, the purple series represent the phase 2 test up to 140 kips, and the blue series represent the phase 2 test up to 390 kips. Similar to the results shown previously in this report, the gages are divided into sections based on their location on the anchorage. Images are provided to inform locations of each gages. Data is provide for those gages that were damaged during the concrete pour, and plots are listed as such. Data for phase 2 from these gages should be ignored (it is either unreasonable or zero).

A.1 Channel Sections

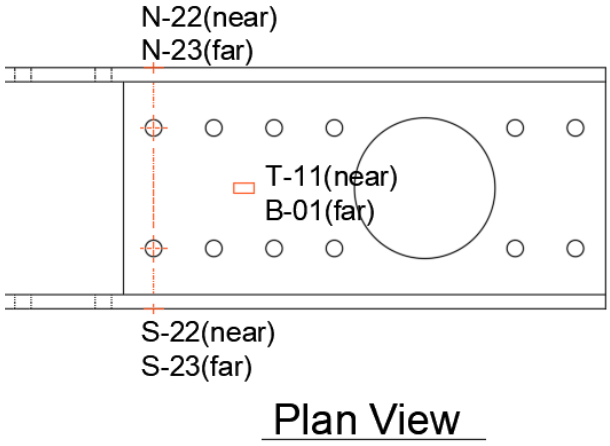

Figure A-1 Plan view of exposed portion of channels showing installed strain gage labels

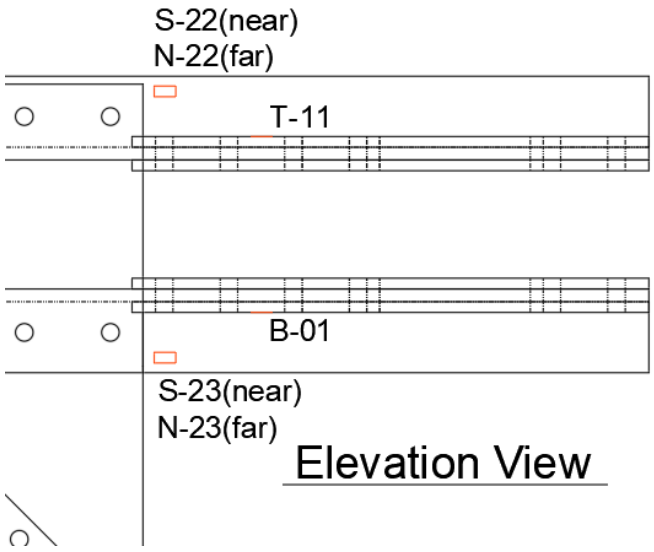

Figure A-2 Elevation view of exposed portion of channels showing strain gage labels

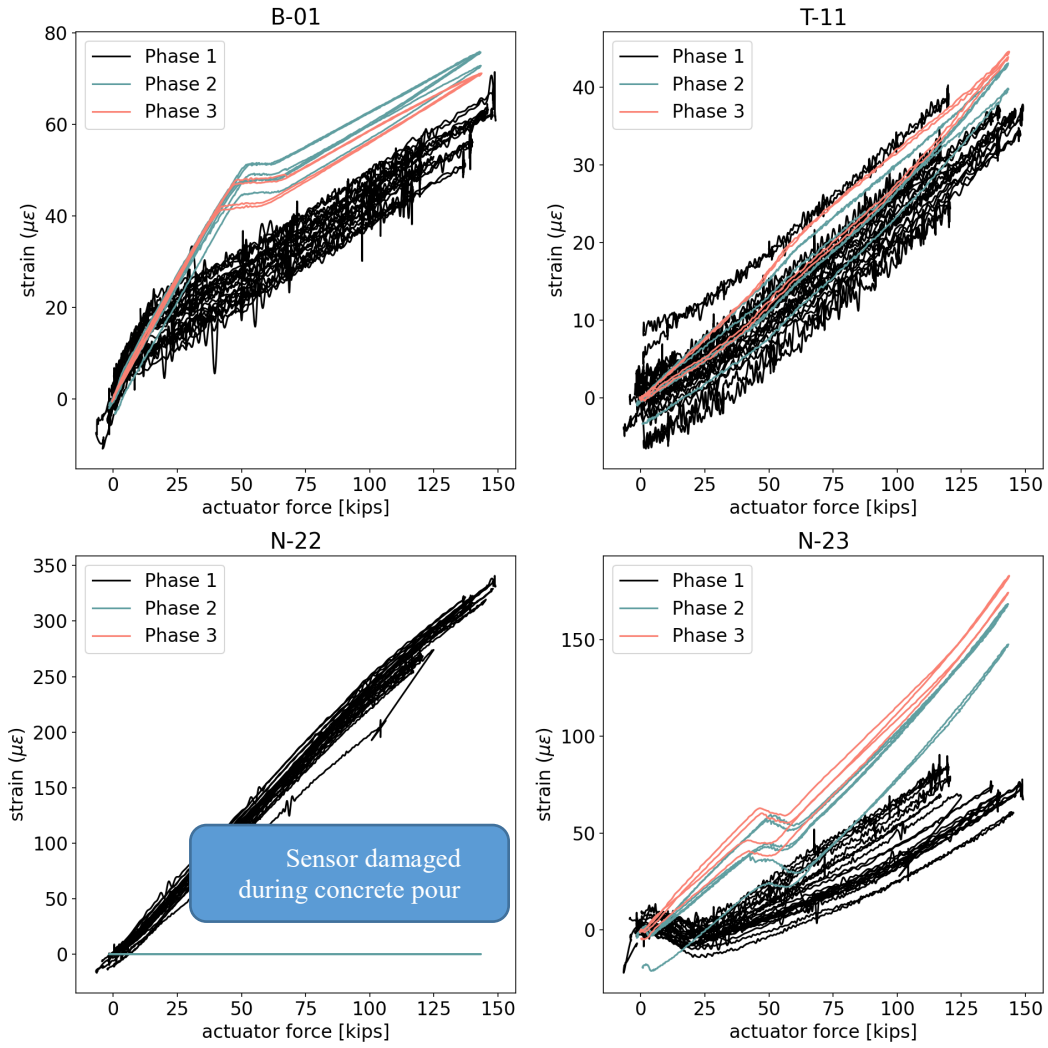

Figure A-3 Response of strain gages on unembedded channel sections

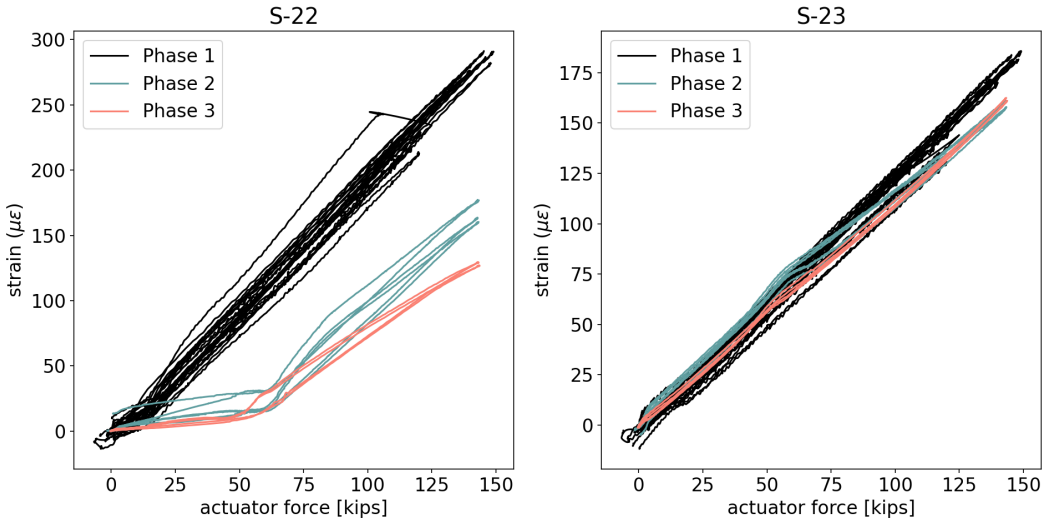

Figure A-4 Response of remainder of strain gages on unembedded channel sections

A.1.1 Max load test

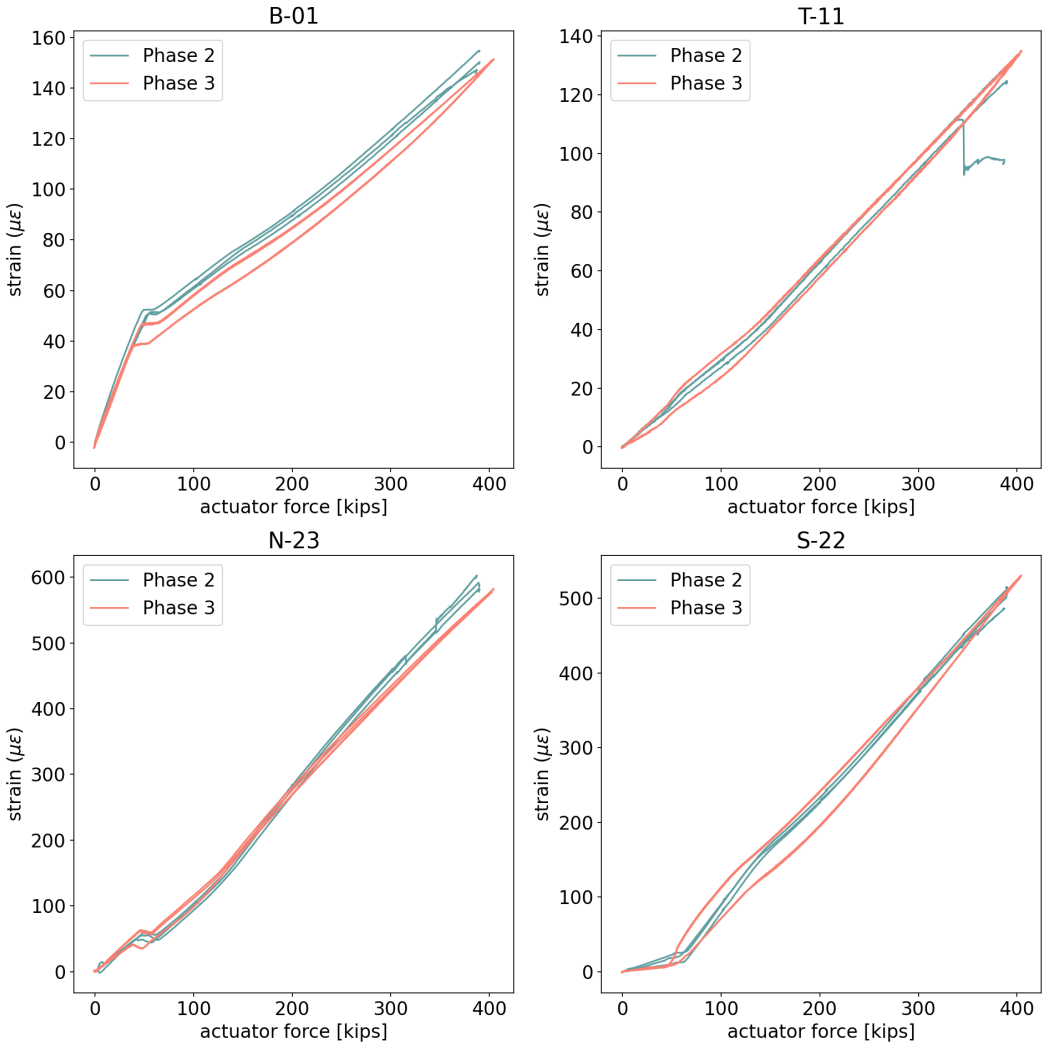

Figure A-5 Response of strain gages on unembedded channel sections at max load

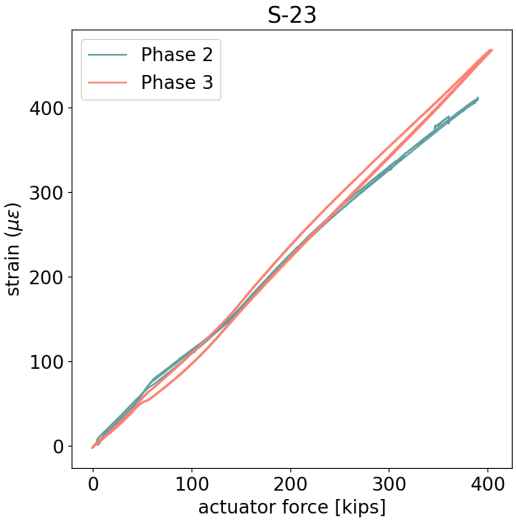

Figure A-6 Response of S-23 at Max load

A.2 North Gusset

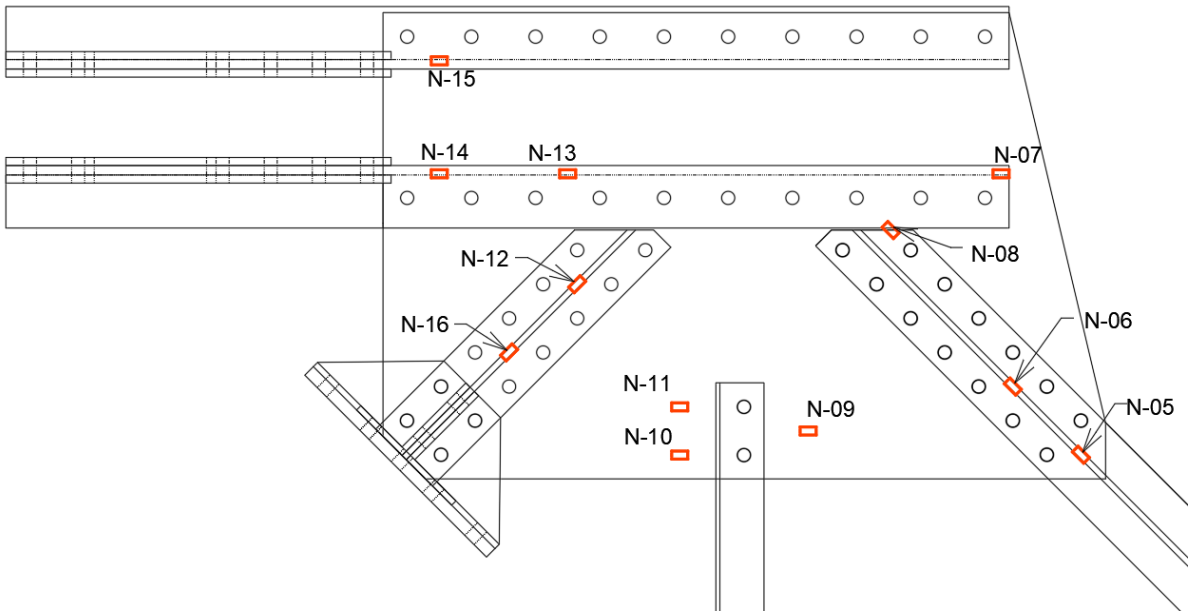

Figure A-7 Strain gage labels for the north gusset

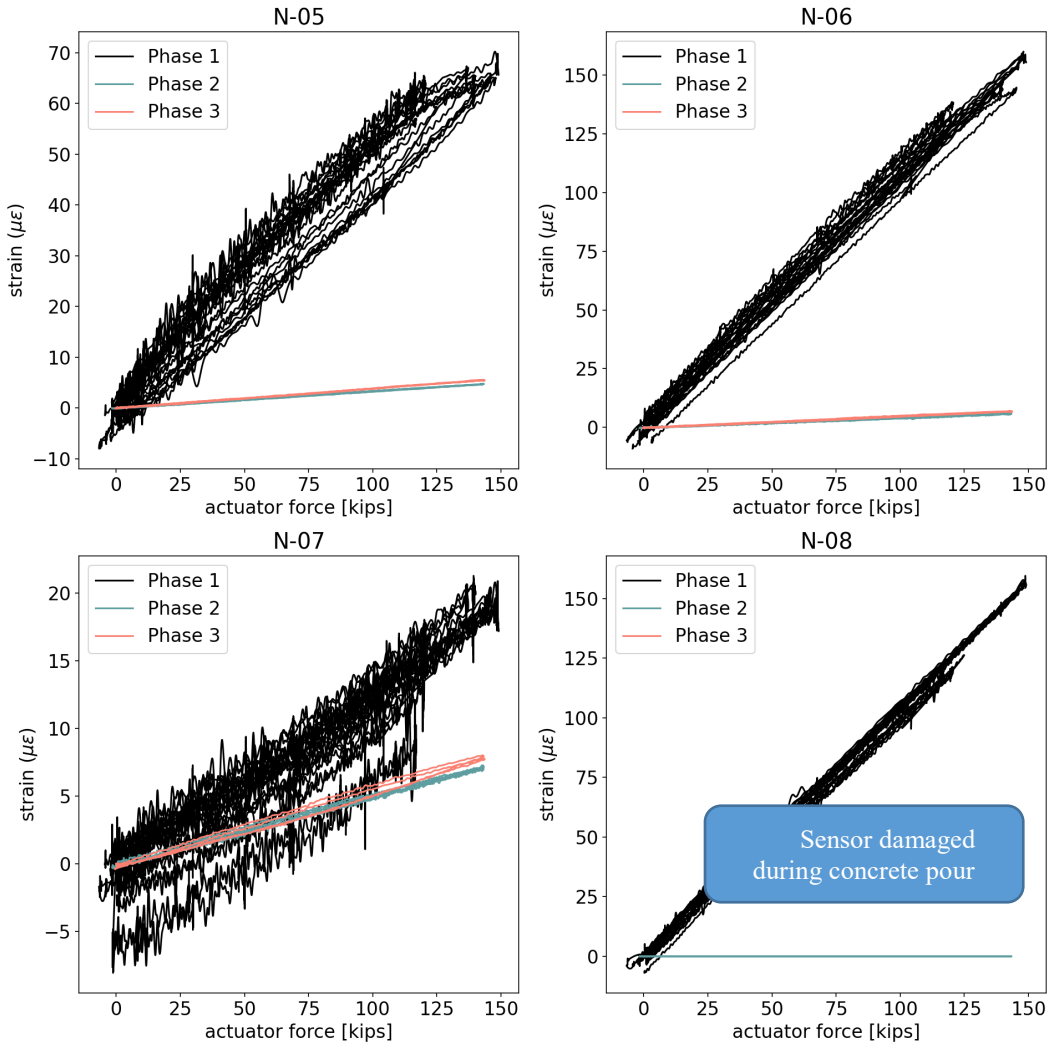

Figure A-8 Response of selection of strain gages on north gusset plate

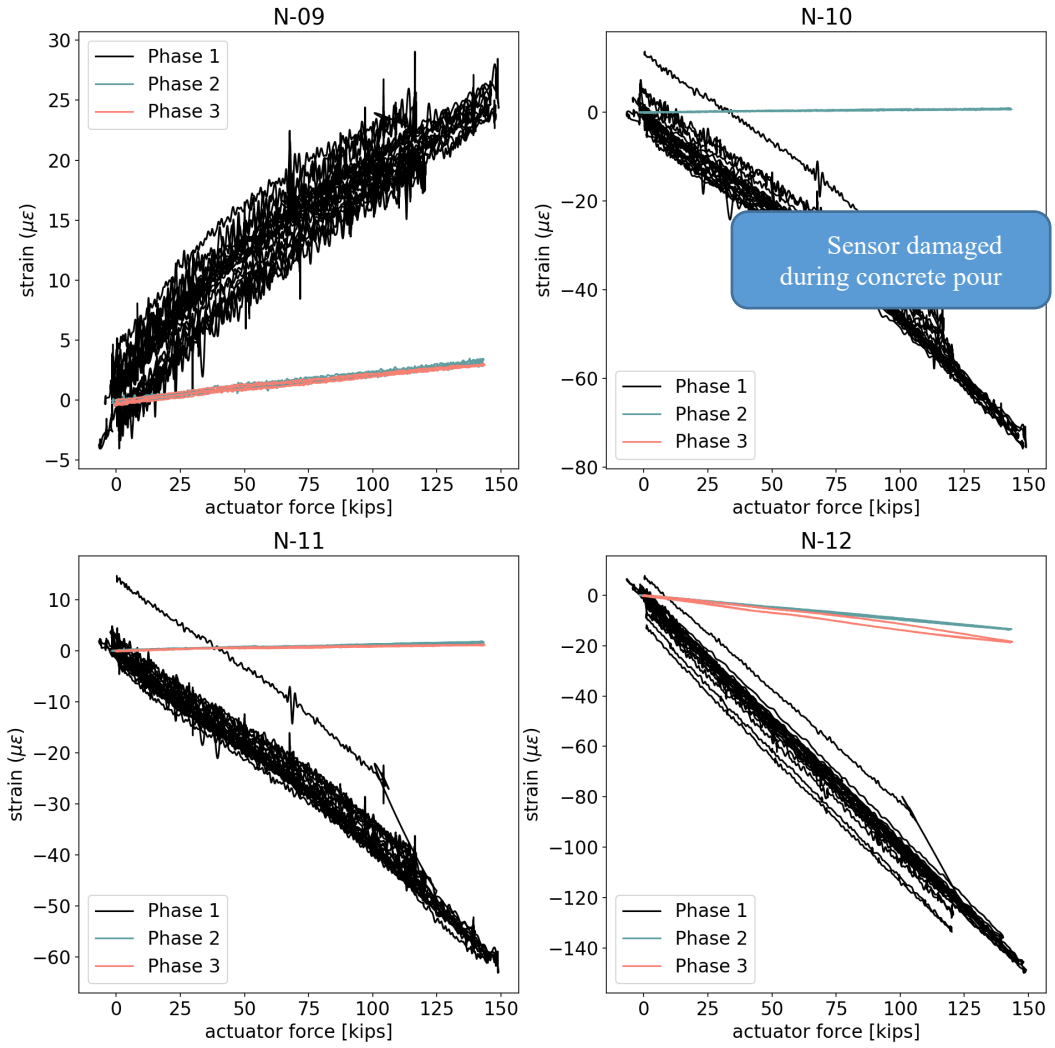

Figure A-9 Response of additional strain gages on north gusset plate

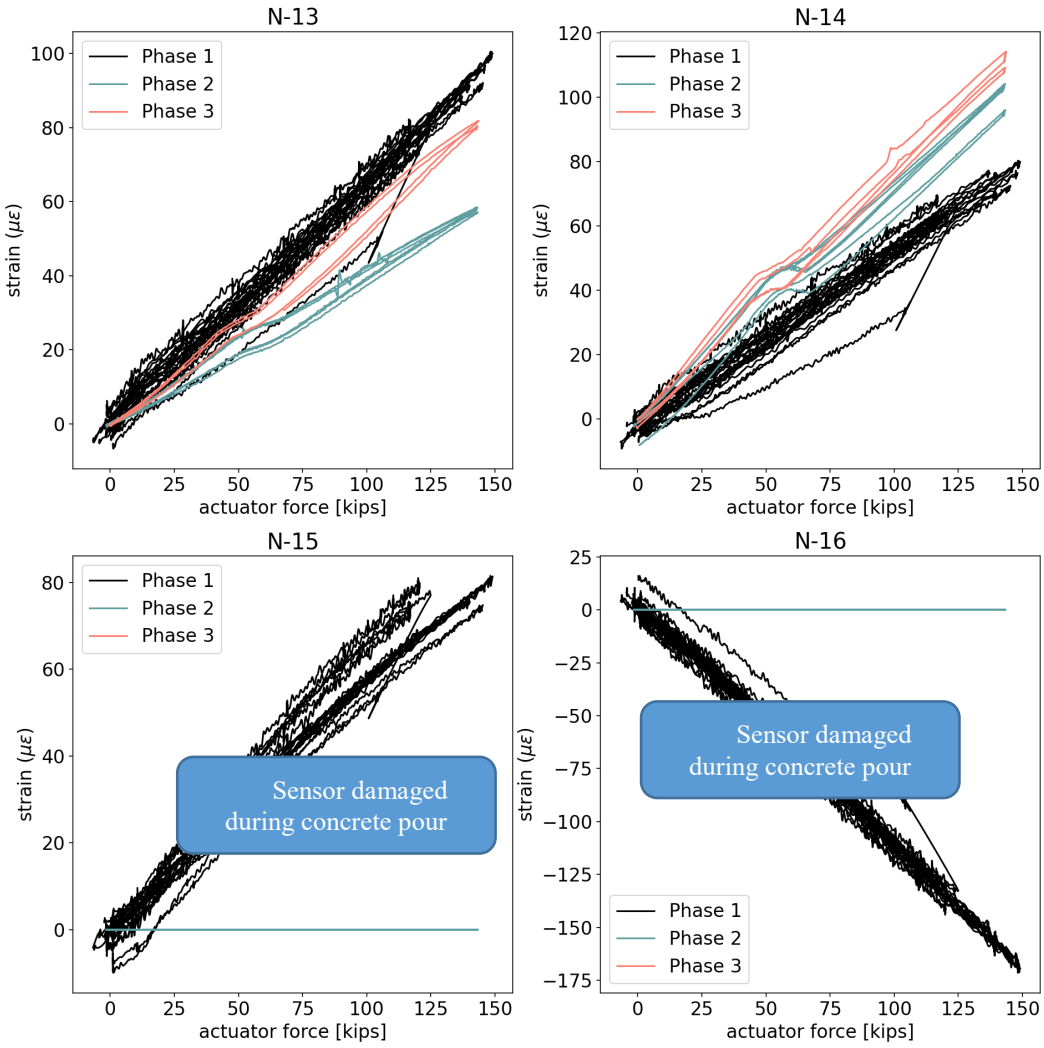

Figure A-10 Response of remainder of strain gages on north gusset plate

A.2.1 Max Load Test

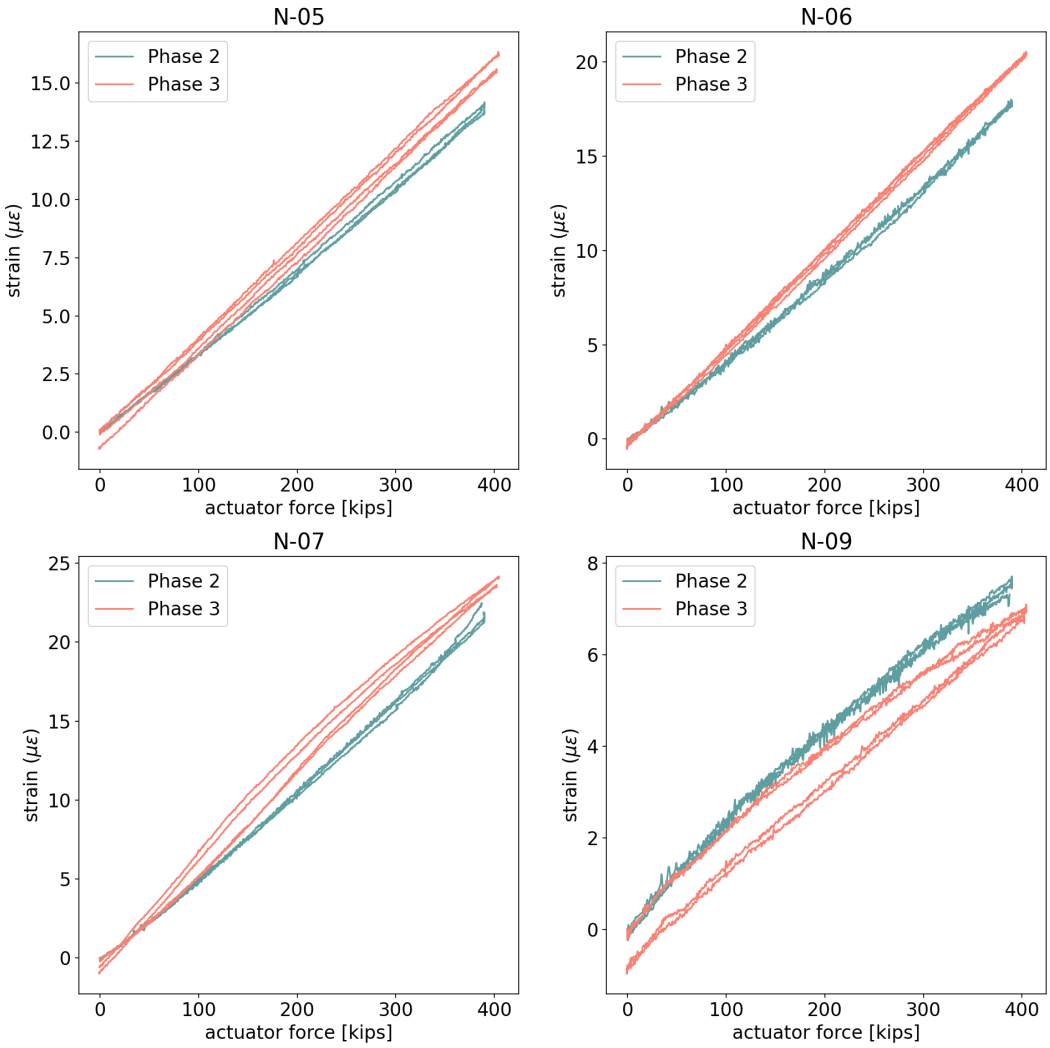

Figure A-11 Response of selection of strain gages on north gusset plate under max load

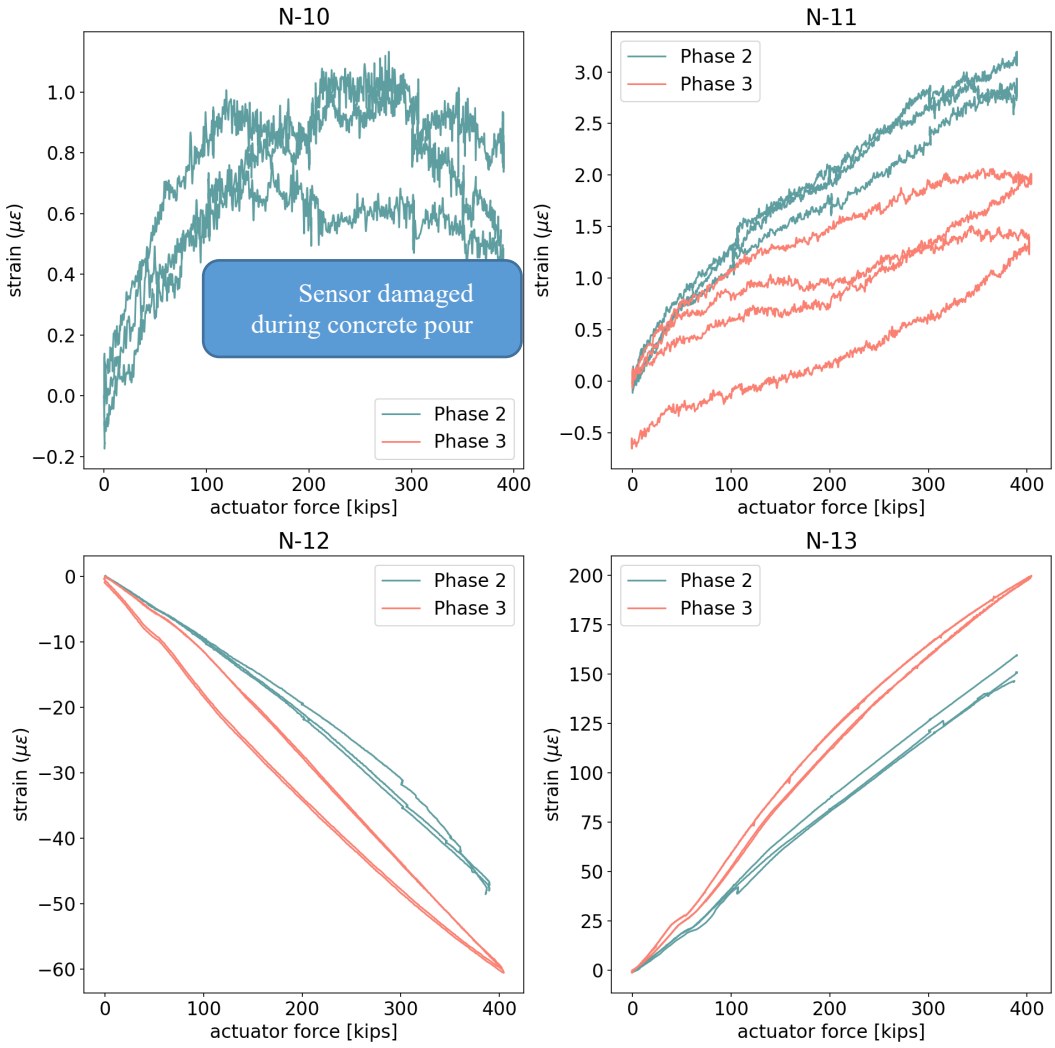

Figure A-12 Response of additional strain gages on north gusset plate under max load

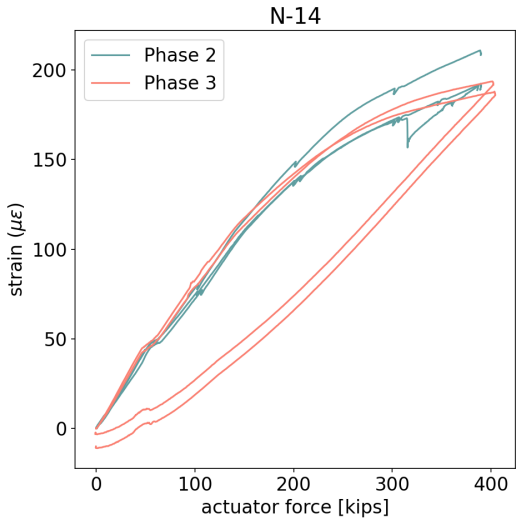

Figure A-13 Response of N-14 on north gusset plate under max load

A.3 South Gusset

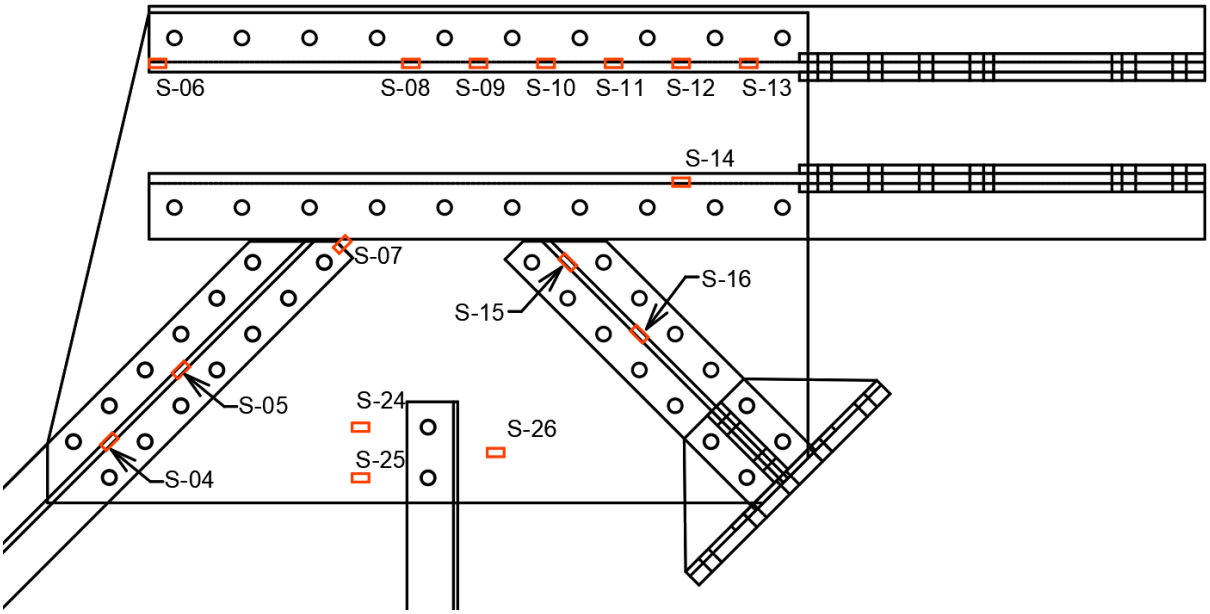

Figure A-14 Labels for strain gages on the south gusset

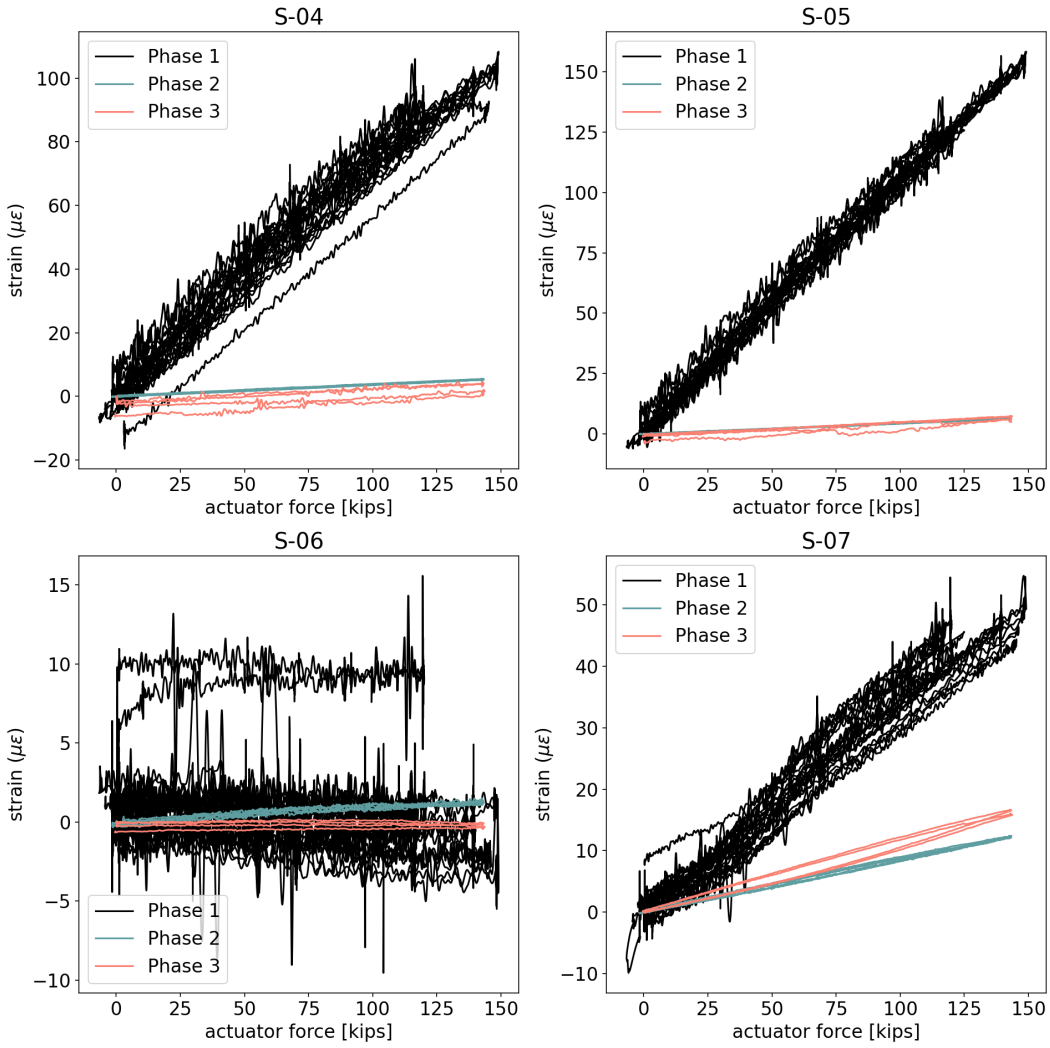

Figure A-15 Response of selection of strain gages on south gusset plate

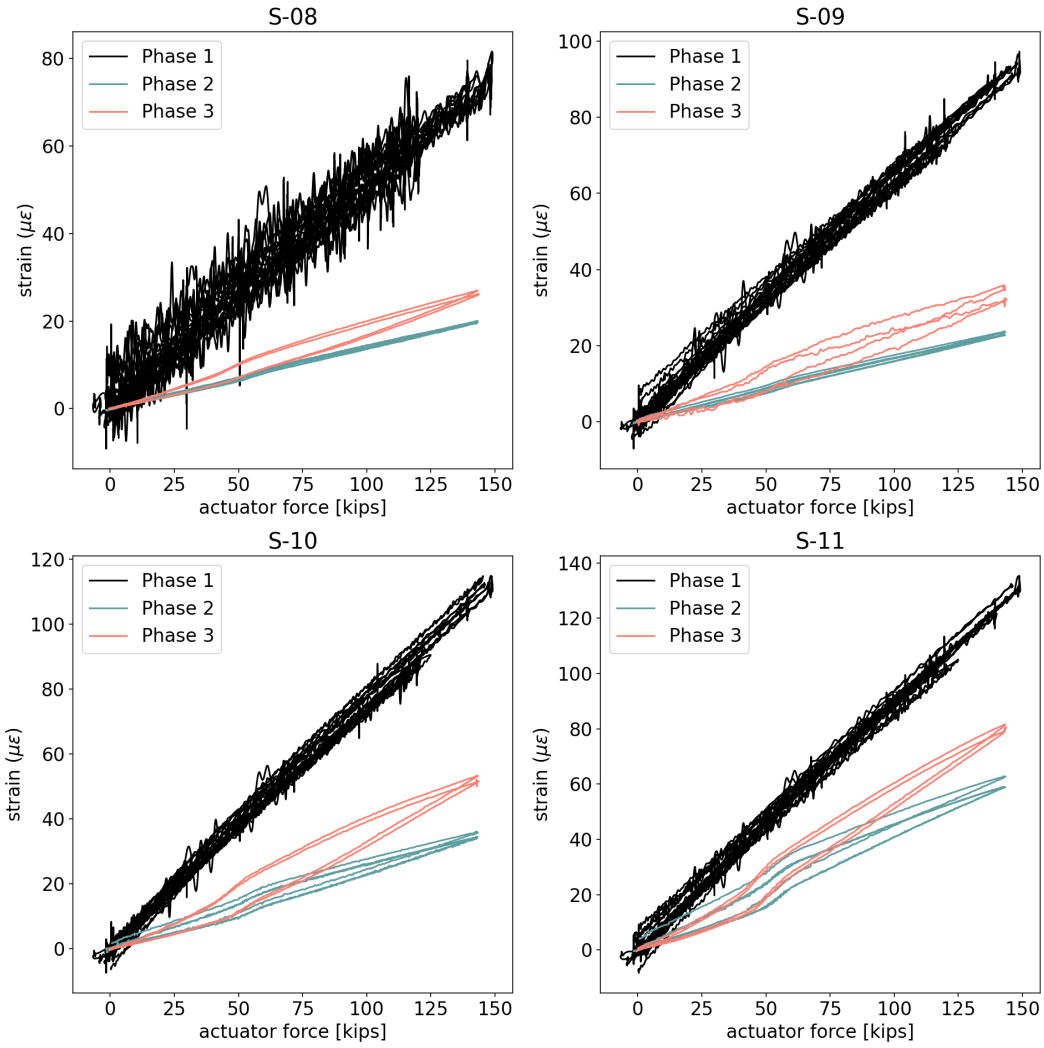

Figure A-16 Response of additional strain gages on south gusset plate

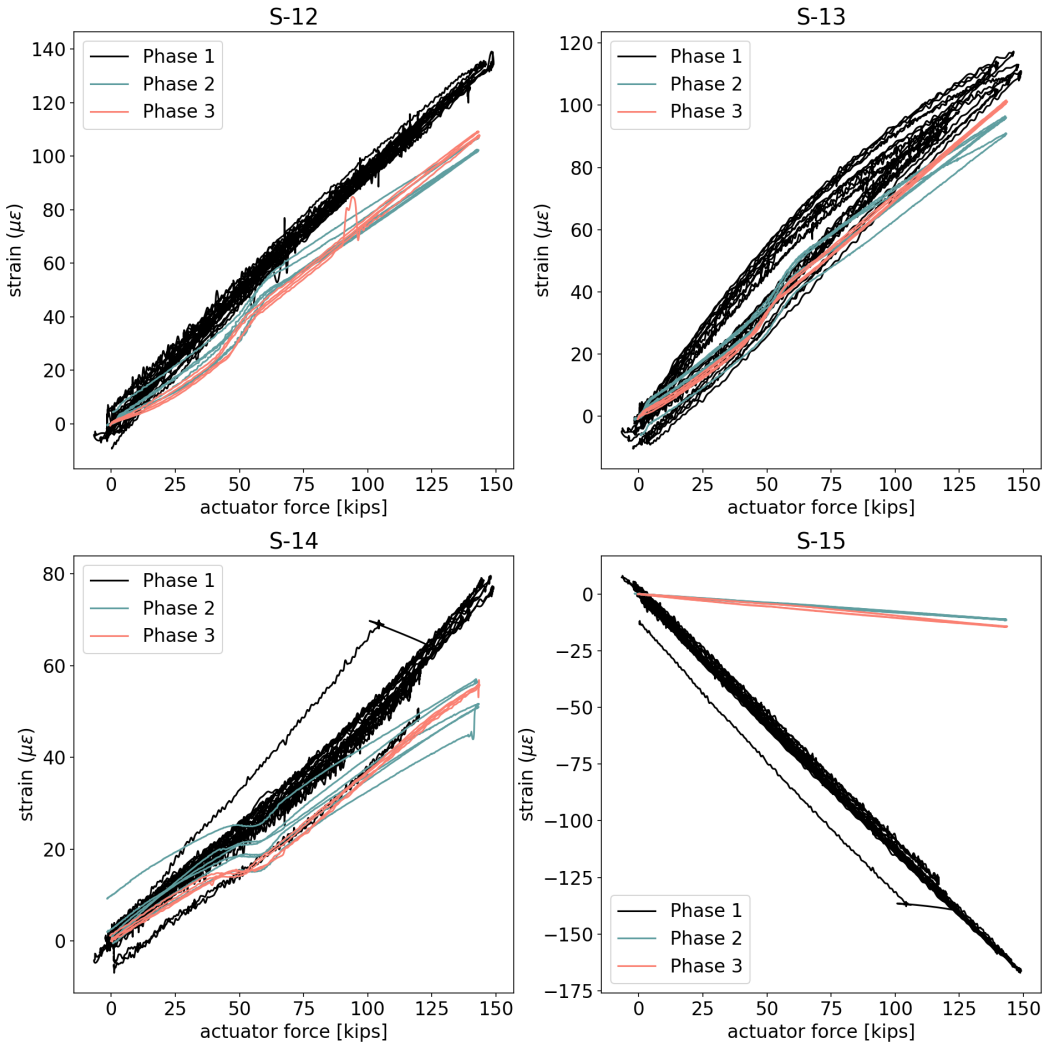

Figure A-17 Response of third set of strain gages on south gusset plate

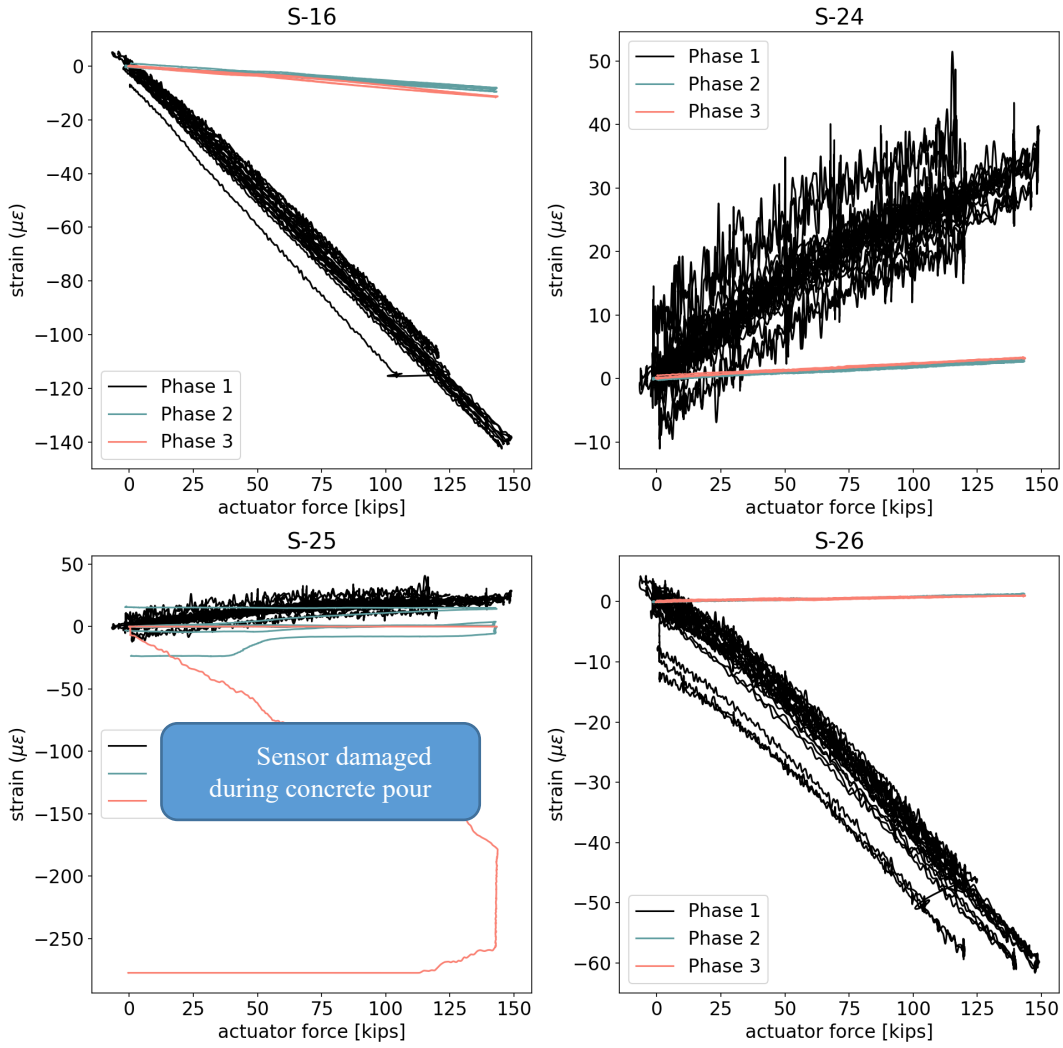

Figure A-18 Response of remaining strain gages on south gusset plate

A.3.1 Max Load Test

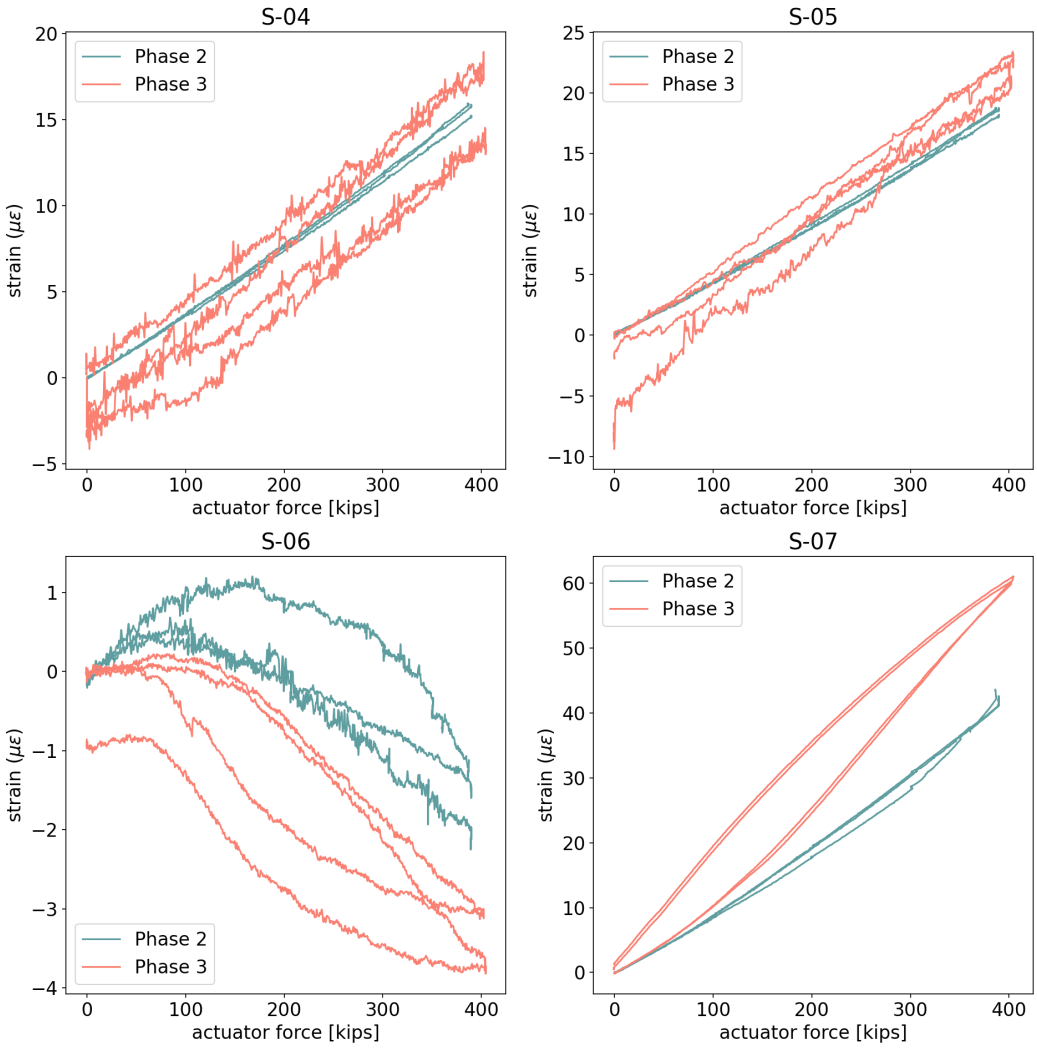

Figure A-19 Response of selection of strain gages on south gusset plate under max load

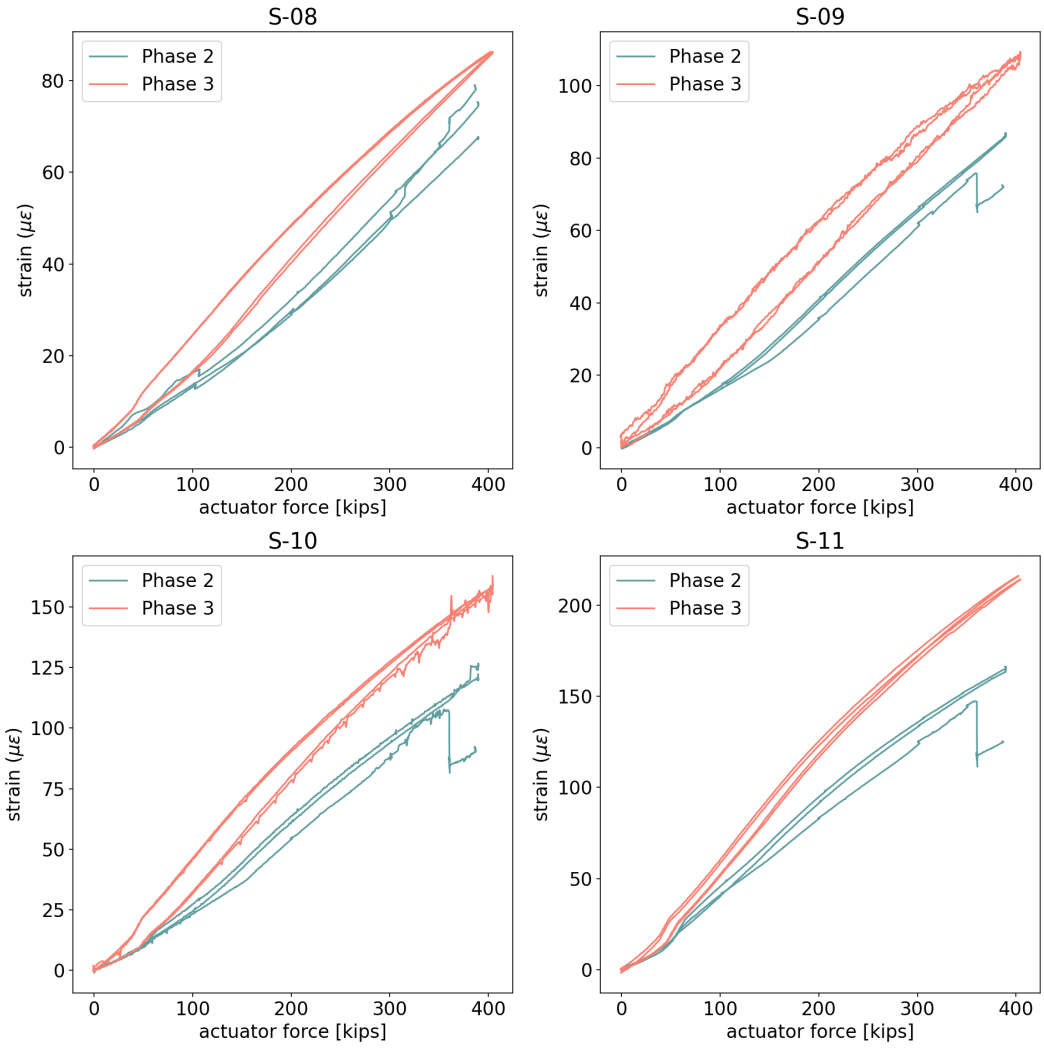

Figure A-20 Response of additional strain gages on south gusset plate under max load

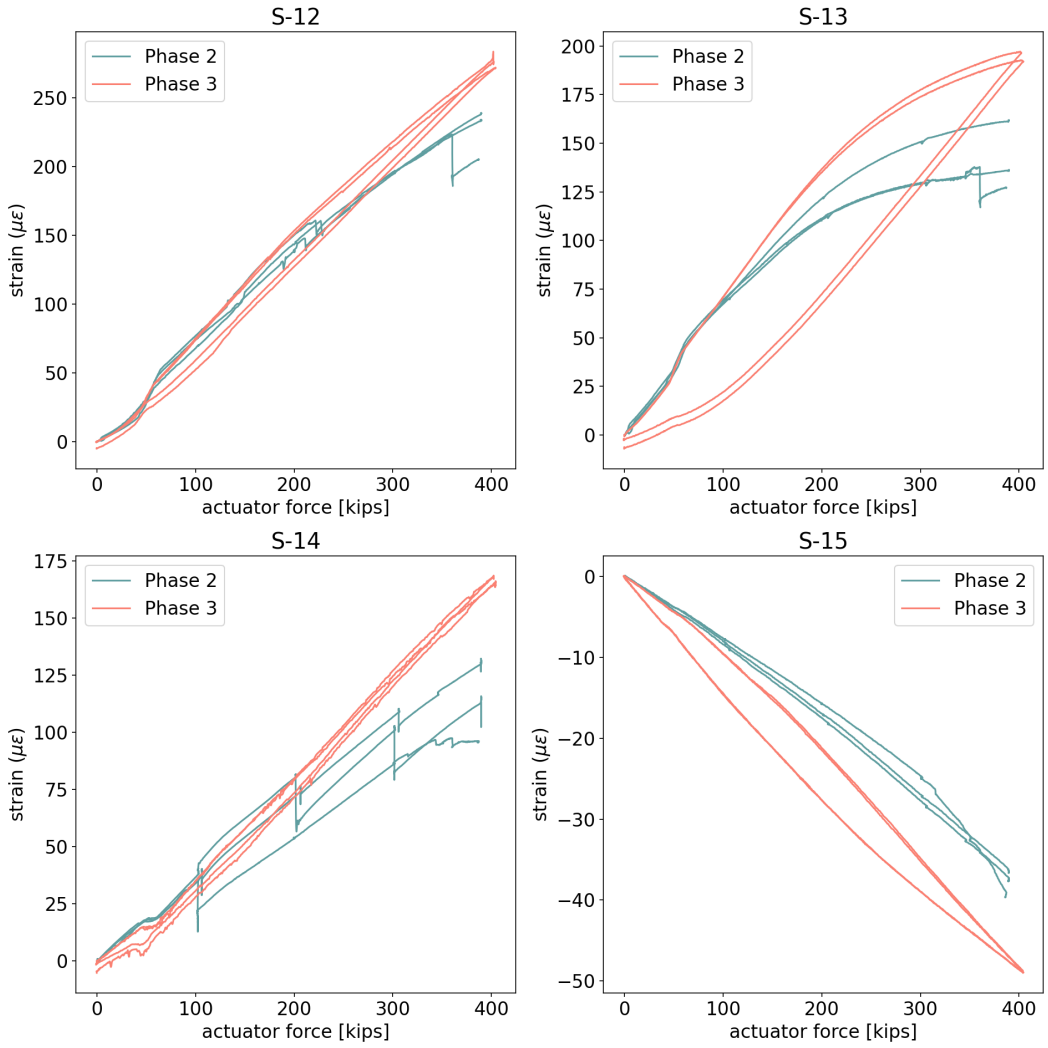

Figure A-21 Response of third set of strain gages on south gusset plate under max load

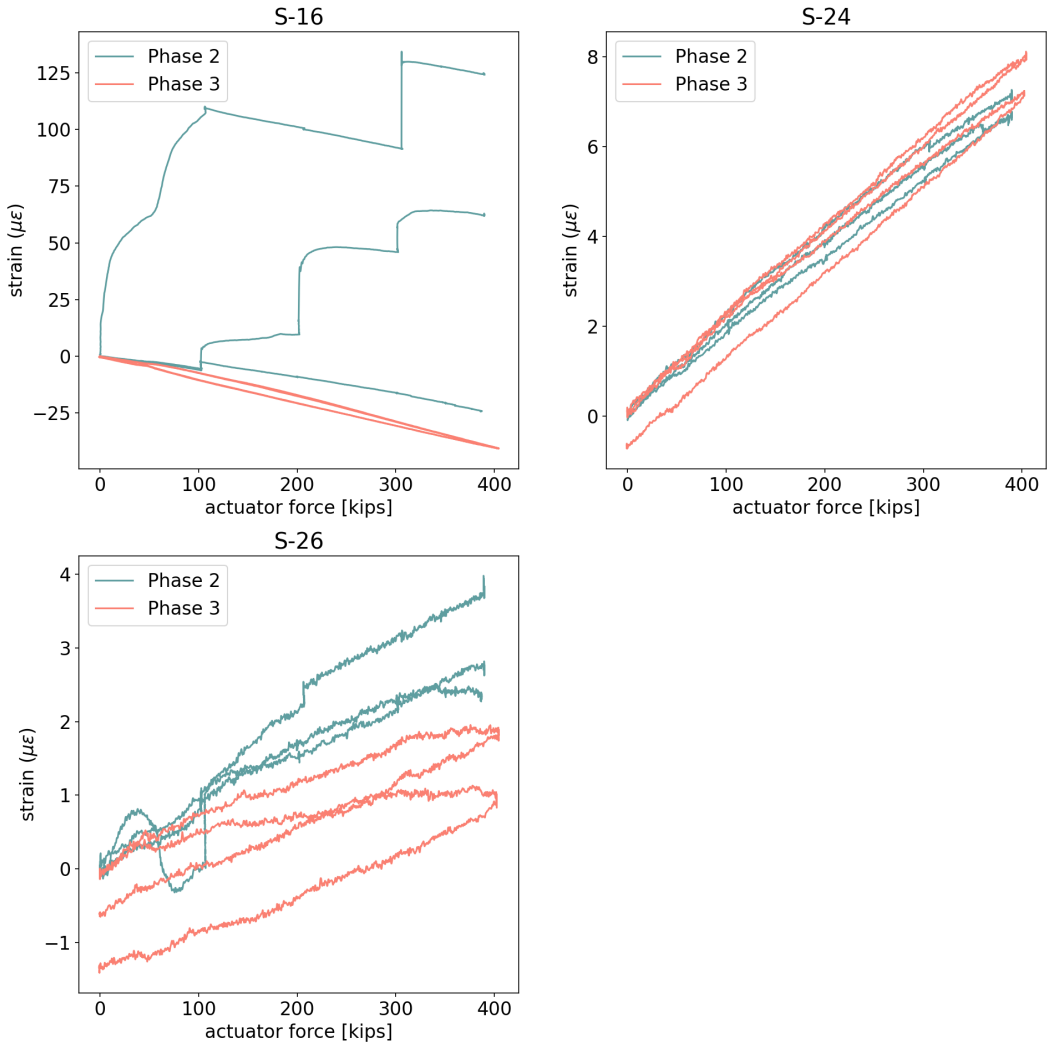

Figure A-22 Response of remaining strain gages on south gusset plate under max load

A.4 Tension Strut

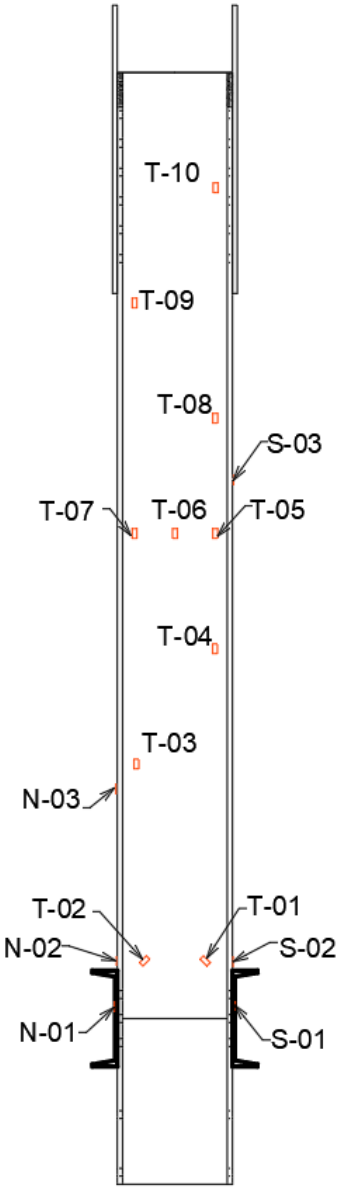

Figure A-23 Labels for strain gages on the tension strut

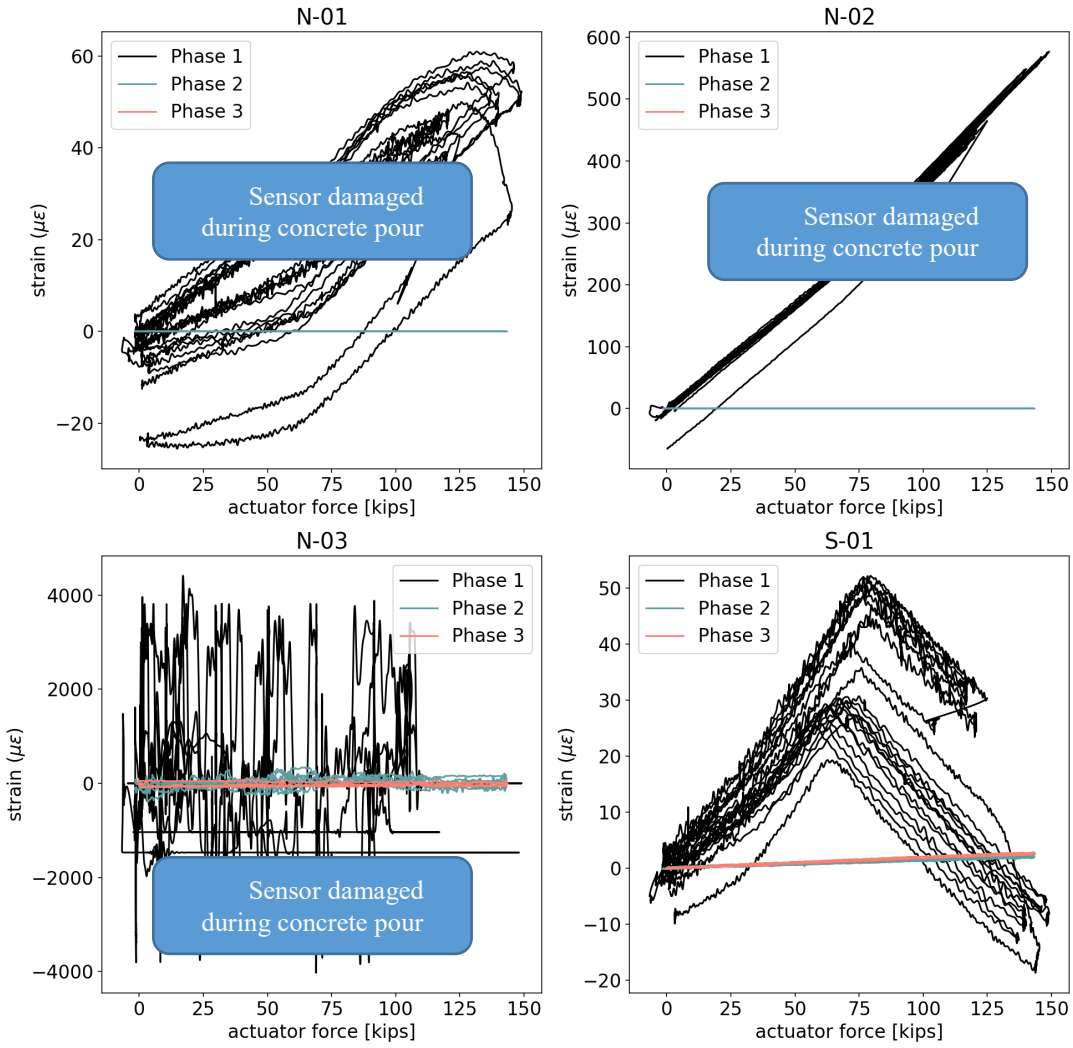

Figure A-24 Response of selection of strain gages on tension strut

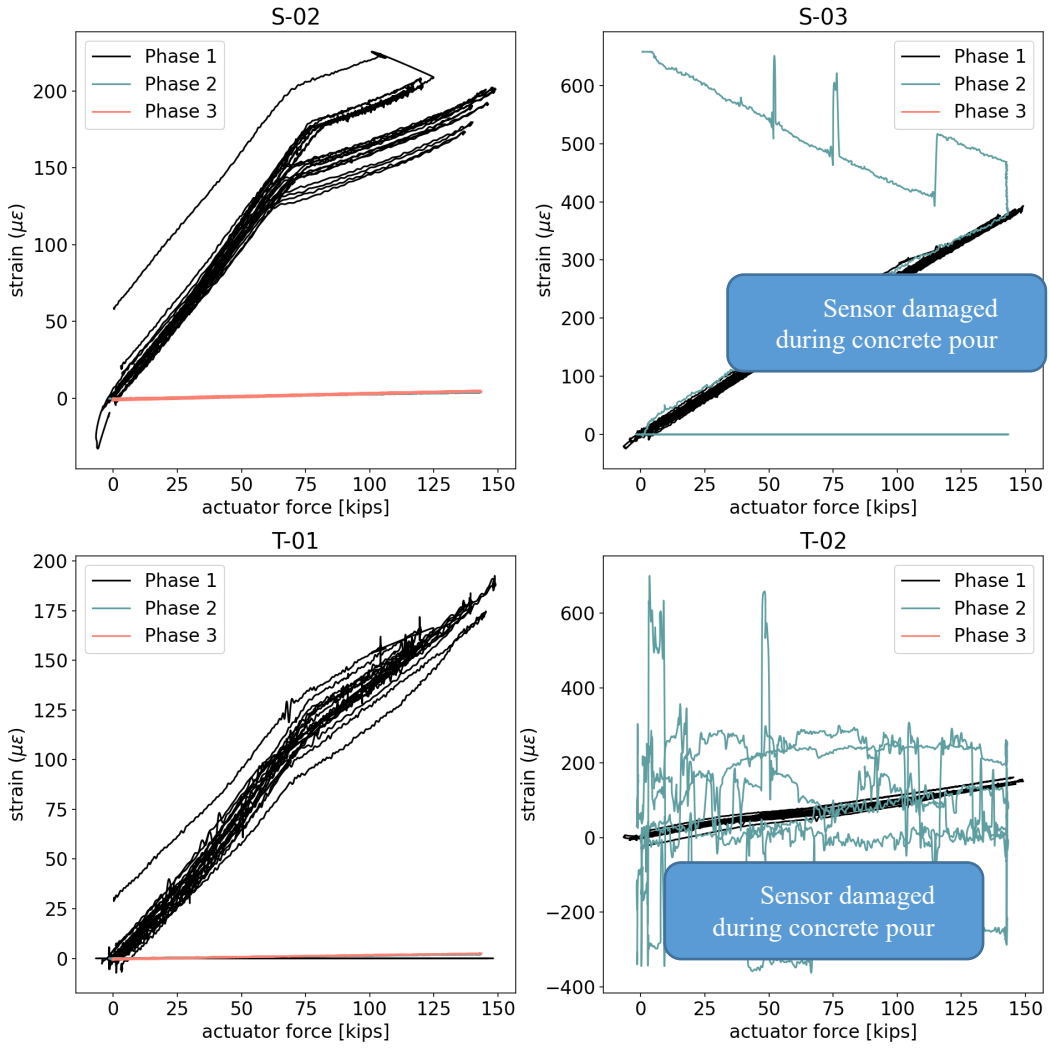

Figure A-25 Response of additional strain gages on tension strut

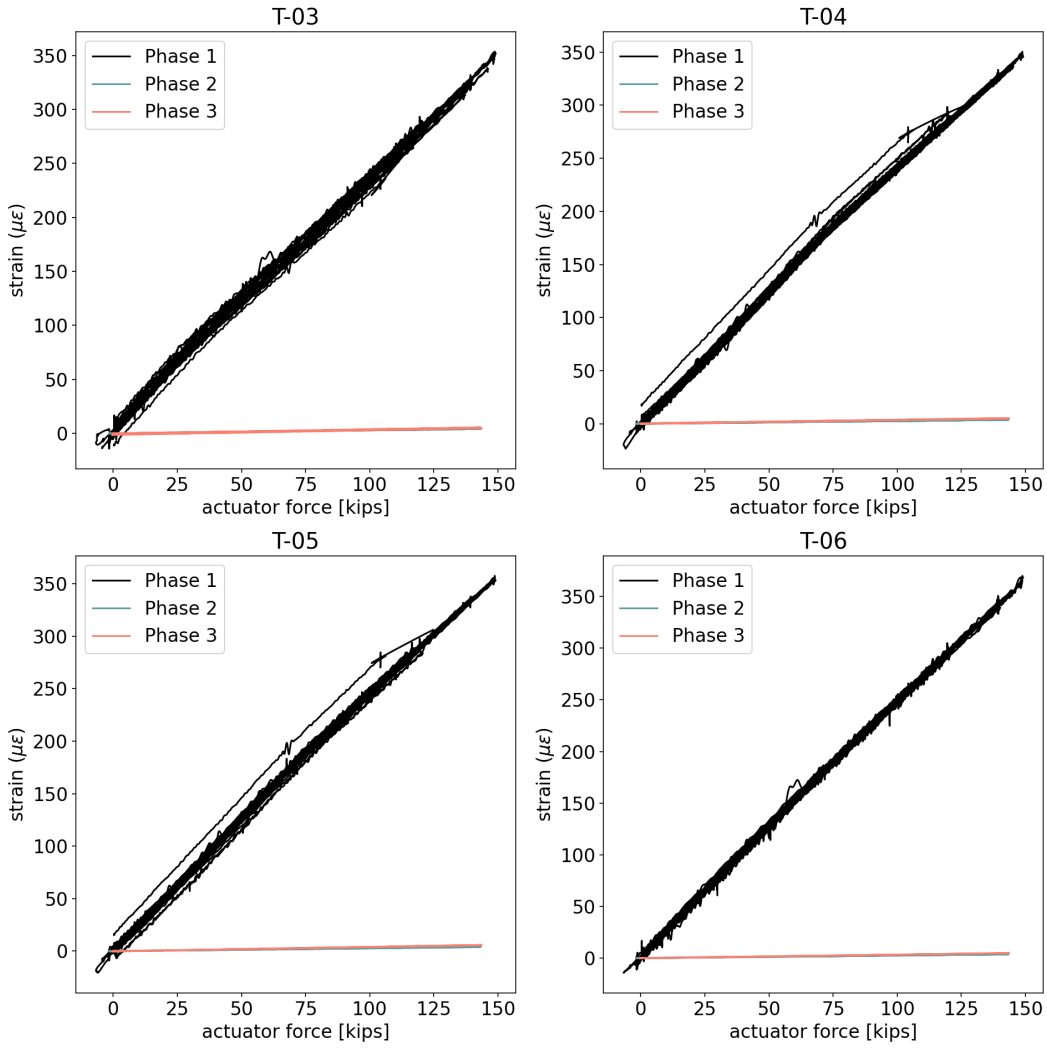

Figure A-26 Response of third set of strain gages on tension strut

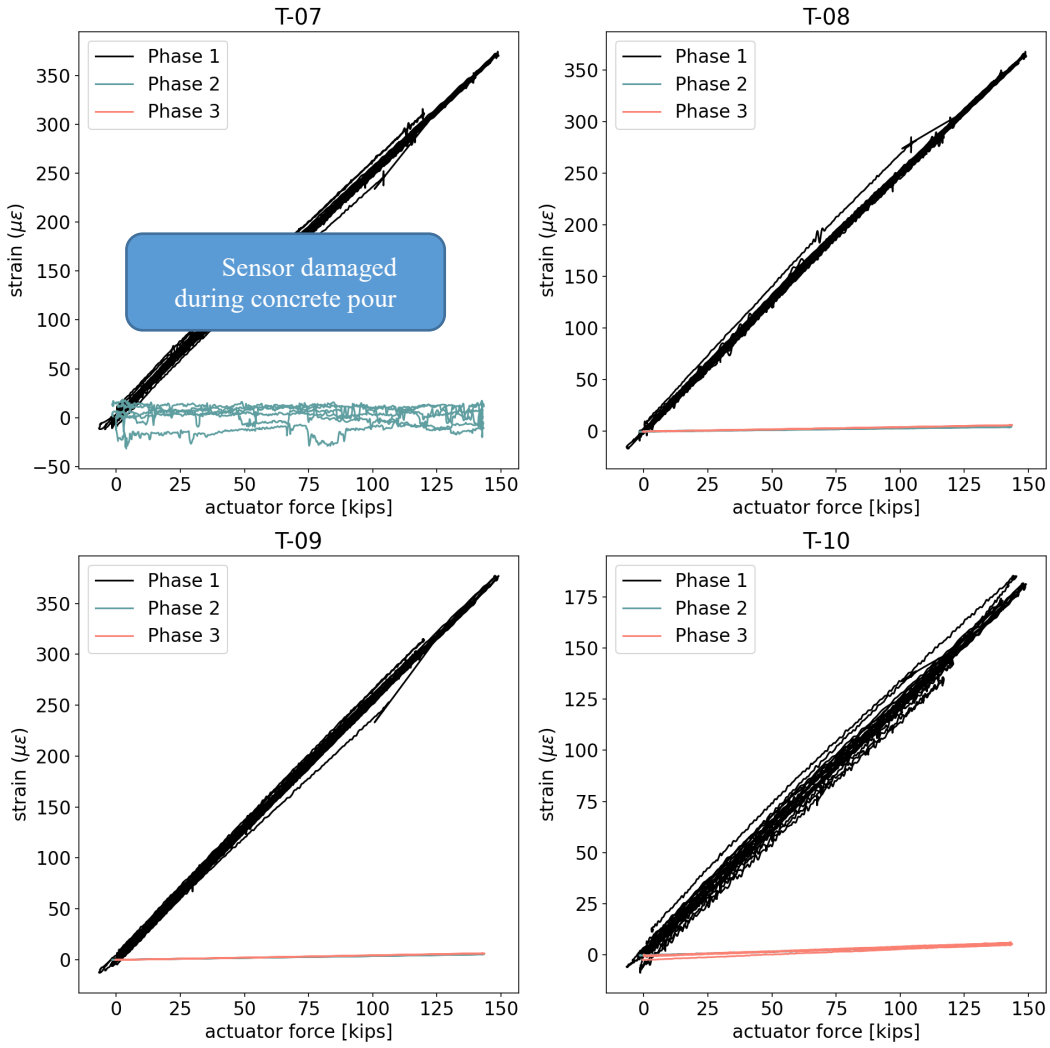

Figure A-27 Response of remaining strain gages on tension strut

A.4.1 Max load test

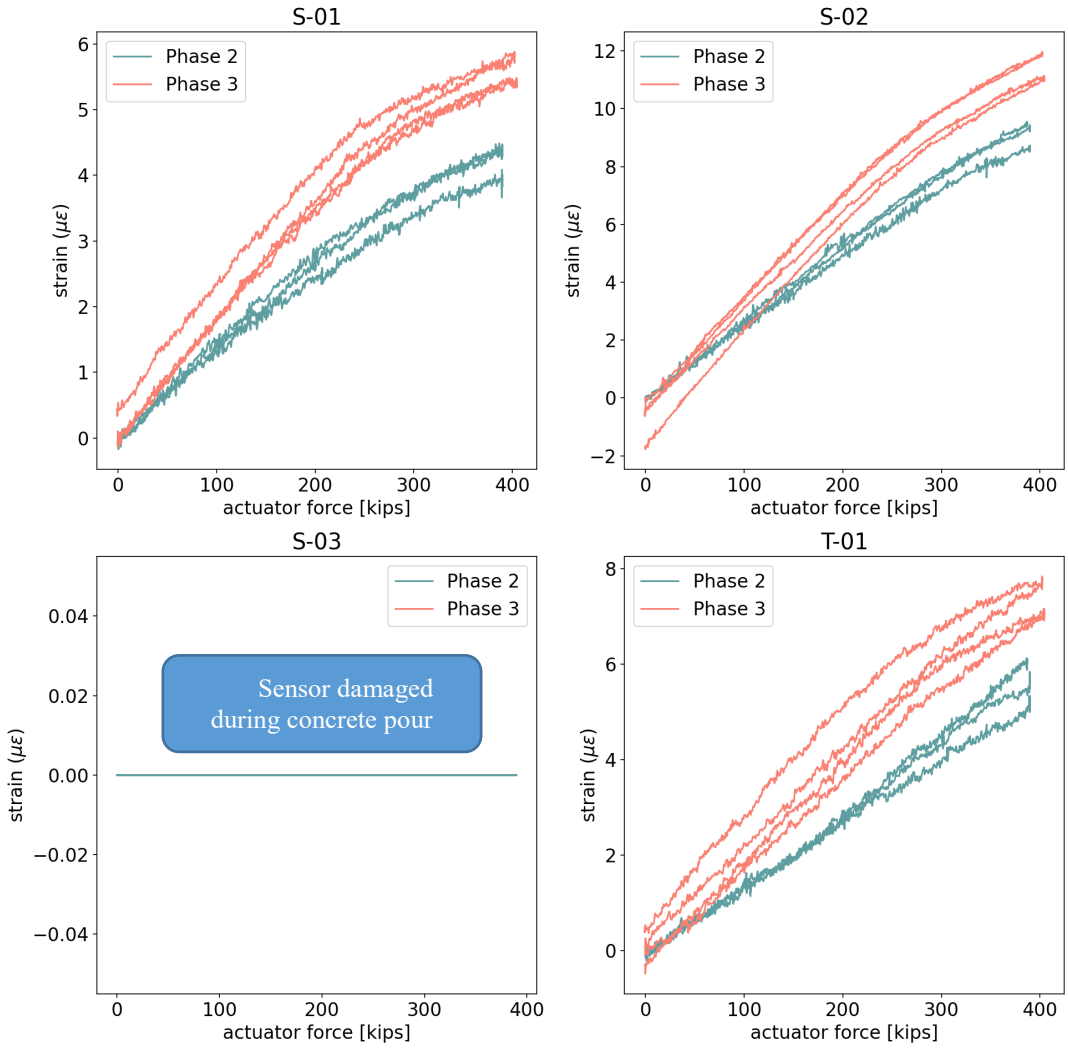

Figure A-28 Response of selection of strain gages on tension strut under max load

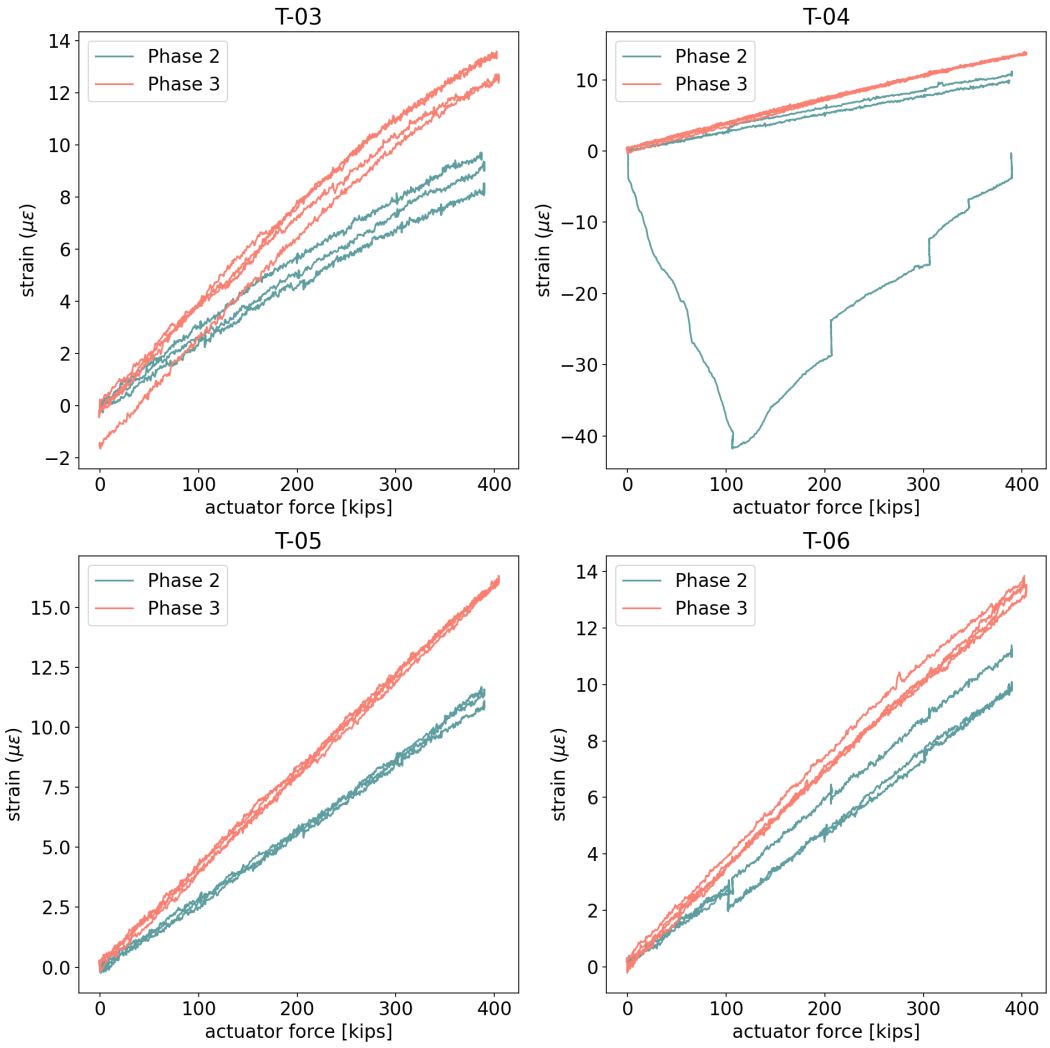

Figure A-29 Response of additional strain gages on tension strut under max load

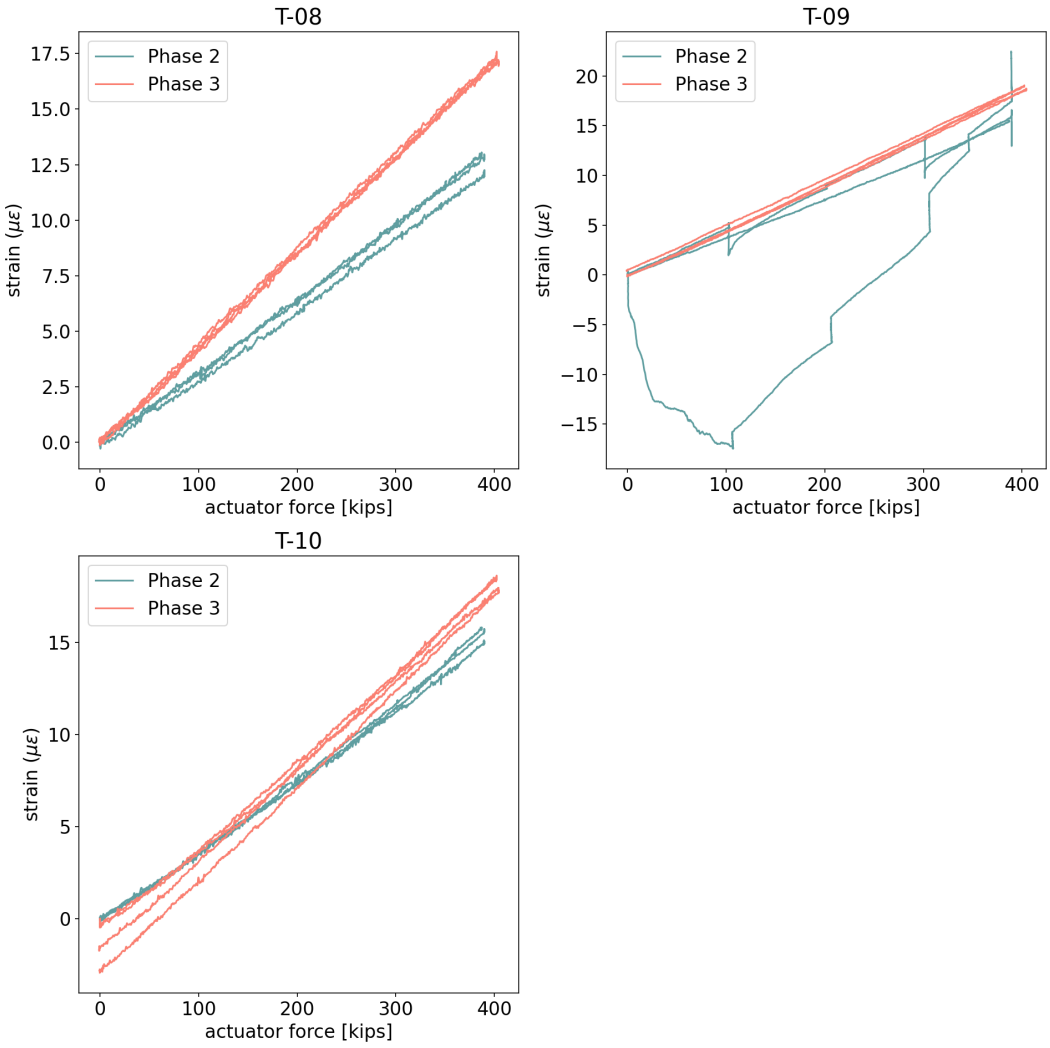

Figure A-30 Response of remaining strain gages on tension strut under max load

A.5 Compression Strut

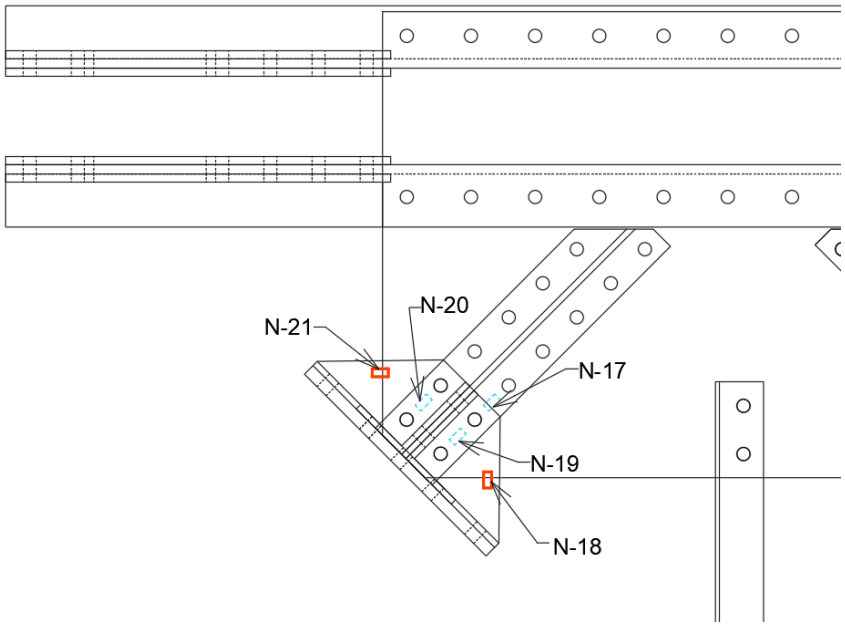

Figure A-31 Labels for strain gages on north side of compression strut. Red gages are on the outside, blue gages are on the inside

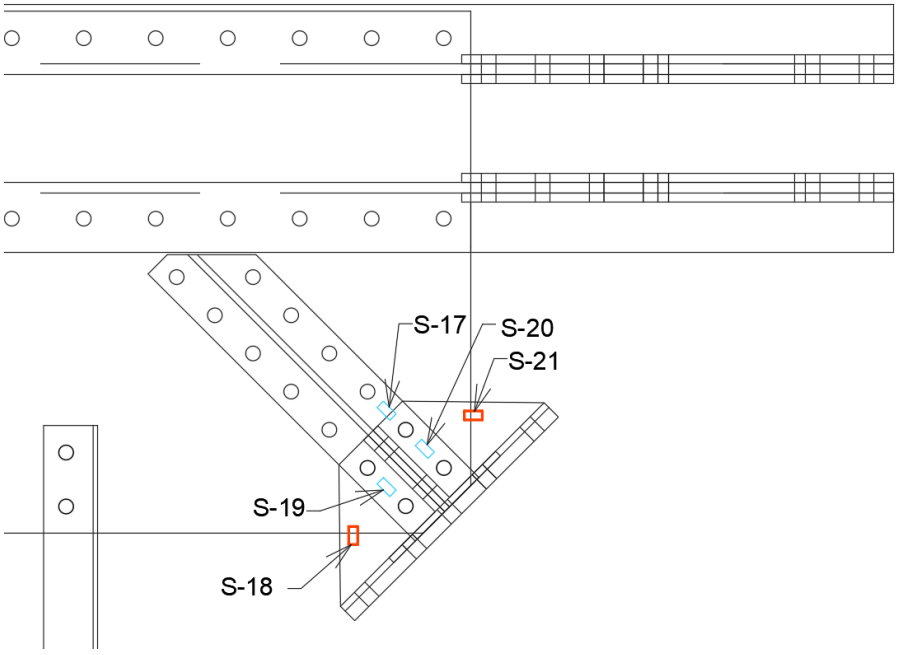

Figure A-32 Labels for strain gages on the south side of the compression strut. Red gages are on the outside, blue gages on the inside.

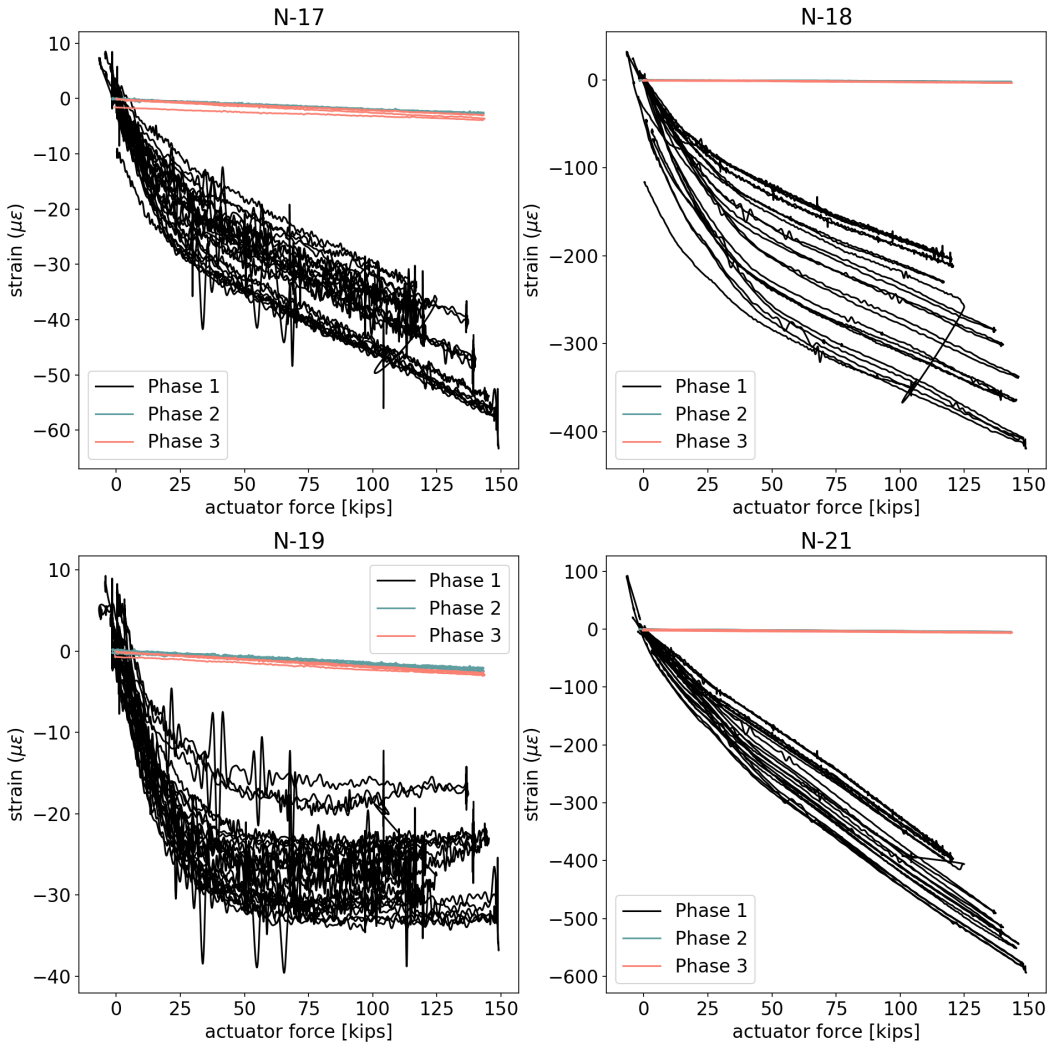

Figure A-33 Response of selection of strain gages on compression strut

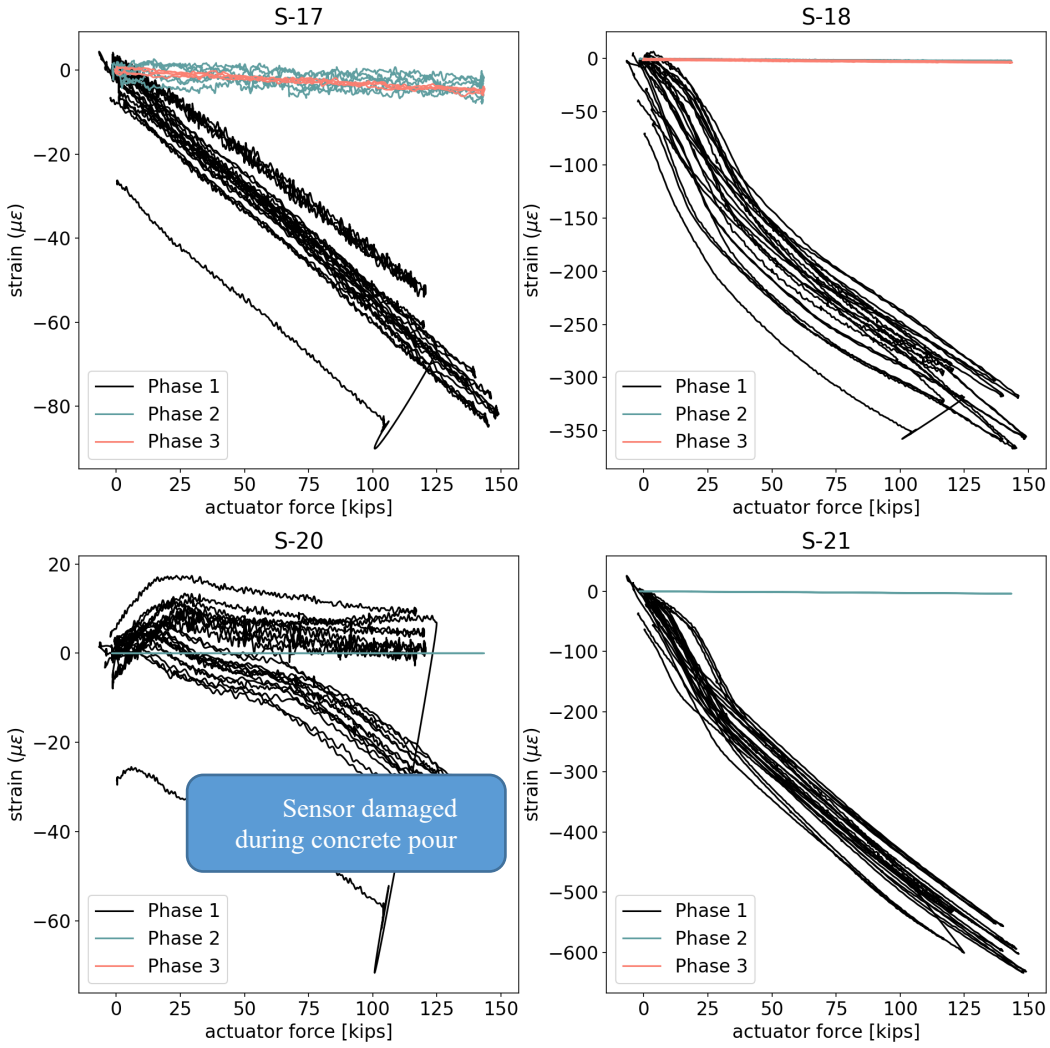

Figure A-34 Response of additional strain gages on compression strut

A.5.1 Max Load test

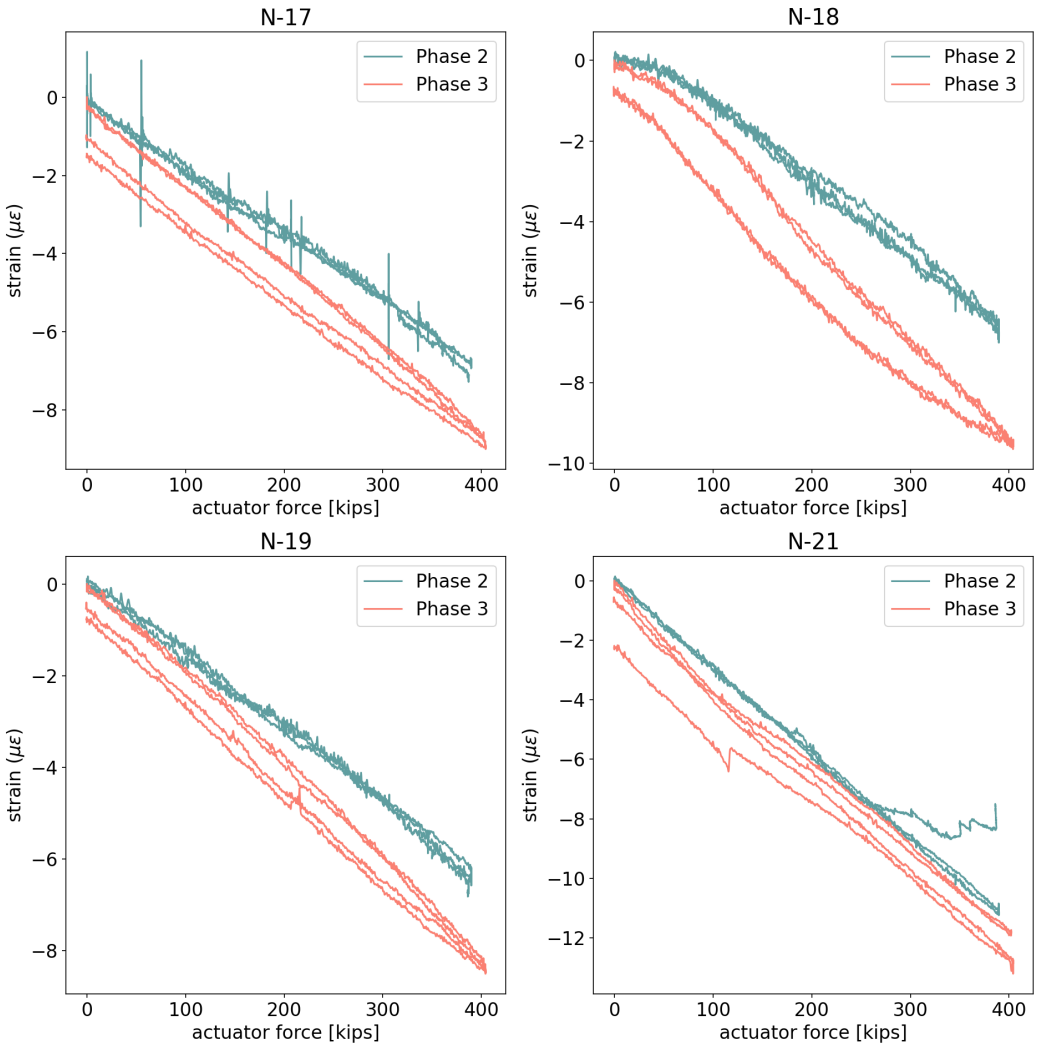

Figure A-35 Response of selection of strain gages on compression strut under max load

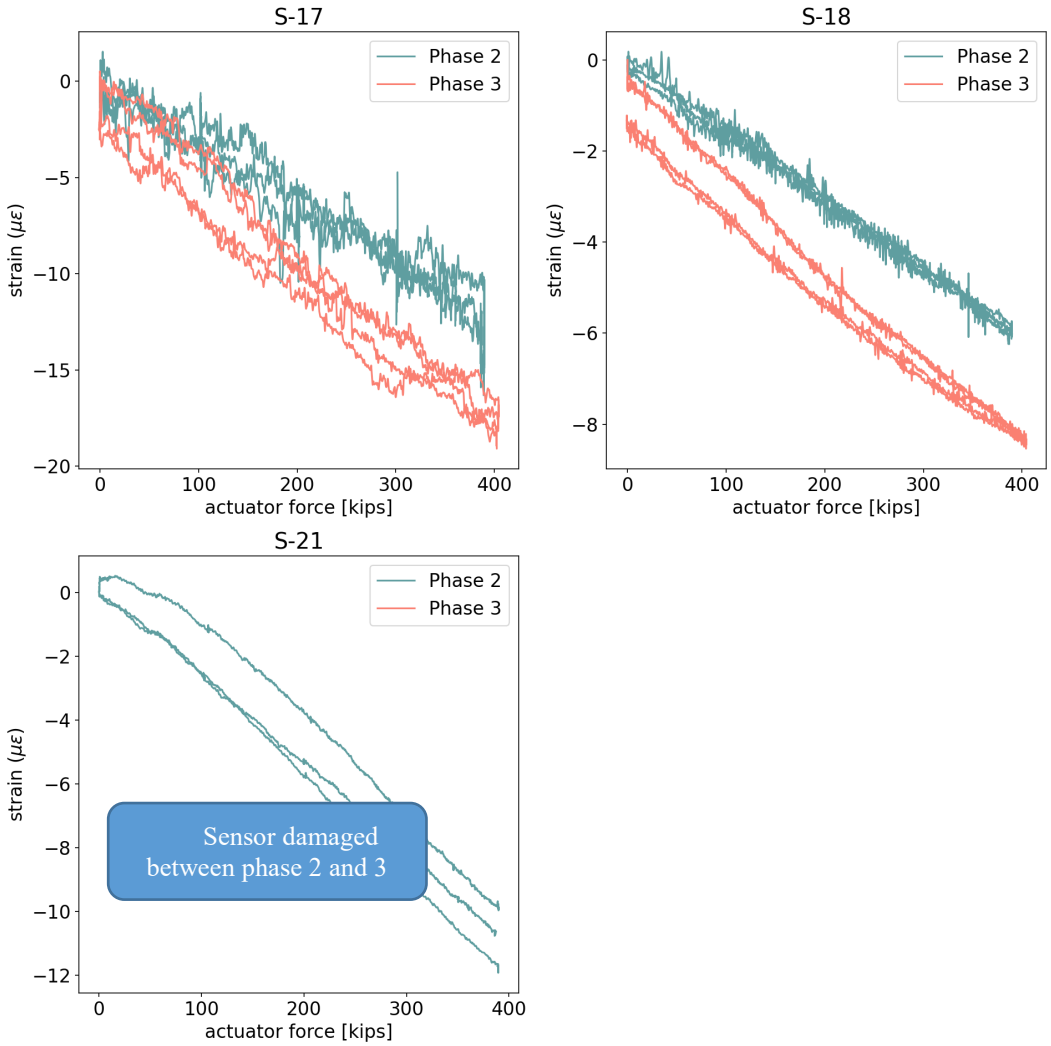

Figure A-36 Response of additional strain gages on compression strut under max load

List of Recent NSEL Reports

No.	*Authors*	*Title*	*Date*
037	Li, J. and Spencer, B.F.	Monitoring, Modeling, and Hybrid Simulation: An Integrated Bayesian-based Approach to High-fidelity Fragility Analysis	May 2015
038	Sim, S-H. and Spencer, B.F.	Decentralized Identification and Multimetric Monitoring of Civil Infrastructure using Smart Sensors	June 2015
039	Giles, R.K. and Spencer, B.F.	Development of a Long-term, Multimetric Structural Health Monitoring System for a Historic Steel Truss Swing Bridge	June 2015
040	Spencer, B.F., Moreu, F., and Kim, R.E.	Campaign Monitoring of Railroad Bridges in High-Speed Rail Shared Corridors using Wireless Smart Sensors	June 2015
041	Moreu, F. and Spencer, B.F.	Framework for Consequence-based Management and Safety of Railroad Bridge Infrastructure Using Wireless Smart Sensors (WSS)	June 2015
042	Spencer, B.F. and Gardoni, P. (Eds.)	Innovations and Advances in Structural Engineering: Honoring the Career of Yozo Fujino	August 2015
043	Asai, T. and Spencer, B.F.	Structural Control Strategies for Earthquake Response Reduction of Buildings	August 2015
044	Kim, R. and Spencer, B.F.	Modeling and Monitoring of the Dynamic Response of Railroad Bridges using Wireless Smart Sensors	September 2015
045	Wierschem, N. and Spencer, B.F.	Targeted Energy Transfer using Nonlinear Energy Sinks for the Attenuation of Transient Loads on Building Structures	September 2015
046	Fahnestock, L.A. and Hashash, Y.M.A.	Structural and Geotechnical Observations after the April 25, 2015 M7.8 Gorkha, Nepal Earthquake and its Aftershocks	December 2016
047	Yoon, H. and Spencer, B.F.	Enabling Smart City Resilience: Post-disaster Response and Structural Health Monitoring	December 2016
048	Kozak, D.L., Luo, J., Olson, S.M., LaFave, J.M., and Fahnestock, L.A.	Modification of Ground Motions for use in Central North America: Southern Illinois Surface Ground Motions for Structural Analysis	September 2017
049	Fermandois, G.A. and Spencer, B.F.	Development and Implementation of a Multi-axial Real-time Hybrid Simulation Framework	September 2018
050	Eick, B.A. and Spencer, B.F.	Structural health monitoring of inland navigation infrastructure	August 2021
051	Najafi, A. and Spencer, B.F.	Multi-axial Real-time Hybrid Simulation Framework for Testing Nonlinear Structural Systems with Multiple Boundary Interfaces	August 2021
052	Eick, B.A., Levine, L.M., Smith, M.A., and Spencer, B.F.	Full-scale Laboratory Testing of Embedded Miter Gate Anchorages	October 2021